ABSTRACT

DONG, QI. Applications of Metal-Halide Perovskites in Optoelectronic Devices. (Under the direction of Dr. Franky So).

Metal-halide perovskites are a type of emerging low-cost semiconductors, showing a great potential in various optoelectronic applications due to their superior properties. Typically, they have been applied in photovoltaics (PVs), light-emitting diodes (LEDs), and lasers. In this dissertation, three projects have been conducted to explore each of these three applications. The studies on perovskite PVs and LEDs are mainly from the perspective of device physics, while the perovskite lasers are investigated through photo physics and thin-film optics.

The first successful application of perovskites is in PVs. To date, high-quality perovskite thin films with long carrier diffusion length (several μm) can be easily achieved due to the improved synthesis method. To further enhance the efficiency, other functional layers and interfaces become critical. Among them, electron transporting layer (ETL) and its interface with perovskite play a crucial role in electron collection. In the first project of this dissertation, perovskite PVs with aluminum-doped zinc oxide (AZO) as ETL are demonstrated. By inserting a passivation interlayer at the AZO/perovskite interface, the device efficiency has been improved from 13% to 17%. To understand the mechanism, the interfacial properties are studied, showing that the enhanced efficiency is attributed to a reduced interfacial defect density and an enhanced electron collection efficiency.

Following the success of perovskite PVs, perovskite LEDs are also gaining an increasing attention. Different from perovskite PVs that operate at low voltages, the electric field in perovskite LEDs is much stronger, leading to a prominent ion migration. However, most current studies are focused on the device efficiency, while the understanding of ion migration in perovskite

LEDs is still lacking. Therefore, the second project of this dissertation is focused on studying ion migration in perovskite LEDs by transient electroluminescence and current measurements. Based on this these measurements, a combined analysis of charge injection and recombination dynamics is conducted, enabling us to draw a comprehensive picture of the role of ion migration in device operation.

In addition to PVs and LEDs, perovskites are also promising candidates for gain media in laser applications. Among different laser cavities, distributed feedback (DFB) cavities are interesting because of their single mode operation and low threshold. Although low threshold perovskite DFB lasers driven by pulsed optical pumping have been reported, fine-tuning the cavity is still a challenge due to the lack of a systematic guidance and the time-consuming cavity-fabrication process. In the third project, a facile and systematic methodology for fine-tuning the cavity of perovskite surface-emitting DFB lasers is demonstrated. The cavity-fabrication is simplified by an innovative nanoimprint on the perovskite film, while the cavity fine-tuning is guided by a systematic analysis of the optical modes in the DFB structures. Using this methodology, the process of fine-tuning the perovskite laser cavity is largely simplified.

Applications of Metal-Halide Perovskites in Optoelectronic Devices

by
Qi Dong

A dissertation submitted to the Graduate Faculty of
North Carolina State University
in partial fulfillment of the
requirements for the degree of
Doctor of Philosophy

Material Science and Engineering

Raleigh, North Carolina
2021

APPROVED BY:

Dr. Franky So
Committee Chair

Dr. Elizabeth Dickey

Dr. Ramon Collazo

Dr. Kenan Gundogdu

DEDICATION

To the great minds that not only enlightened this world, but also accompany me on a lonely and perplexing journey striving to seek for the ultimate truth.

BIOGRAPHY

Qi Dong was born in 1992 in Hunan, China. At his age of 7, he dreamed of becoming a scientist. Although he did not quite understand its meaning at that time, all he knew was that he wanted to understand everything, from human mind to the universe. As he grew older, he started to think that science is the only path that would give the ultimate answers to all the questions. Therefore, he found his passion in science and became the top student in science courses all the way to high school. Later, when he went to Hong Kong Baptist University (HKBU) for his bachelor's degree in 2010, he chose physics as his major, and expected to find the ultimate truth through physics.

However, life is beautiful because of surprise. At his age of around 20 in HKBU, the more he tried to explain everything by science, the more he realized that this world is broader than he previously thought. It was both a tragedy and an enlightenment to him. Because of this, he started to liberate his thought from the cage of science and think freely, which transferred his interest from science to philosophy. As a result, he minored philosophy in undergraduate. Descartes, Kant, and Wittgenstein became his idols, and he became infatuated with meditation and reading. Despite all these efforts, he still could not answer the most important question, the meaning of his life.

A turn of fate occurred. Before his graduation from HKBU, he suddenly realized that instead of getting trapped in the endless thinking, why not make a difference in the real world. Meaning is not something that can be isolated from experience. This pragmatic way of thinking leads him to go for the practical applications of science. Since then, his new dream is to become an inventor that make this world better.

The rest of the story is mainly about his journey of pursuing the new dream. He received a master's degree in physics in the University of Hong Kong in 2014, where he learned how to fabricate and characterize perovskite solar cells for future renewable energy resources. After that, he went to North Carolina State University to pursue PhD under the supervision of Prof. Franky So. During this period, he gained broad knowledges and skills, including device physics, device optics, spectroscopy, thin-film characterizations, PVs, LEDs, lasers and so on. More importantly, he has been trained in such a way that he can quickly catch up in a new project that is out of his previous expertise and come up with innovative ideas. Currently, he is trying to push the frontier of organic and hybrid light emitting devices to practical applications by photophysical studies in the ultrafast regime and sophisticated engineering in device optics. This is not the end of the story, and Qi Dong' journey continues.

ACKNOWLEDGMENTS

First, I would like to express the greatest gratitude to my PhD advisor, Prof. Franky So. Thank you for giving me the chance to study in this wonderful research group. The chemistry in this group allows me to learn lots of new knowledges and skills from others and become a team-worker. Most importantly, thank you for teaching me the way of thinking. I would also like to thank Prof. Kenan Gundogdu, Prof. Elizabeth Dickey, and Prof. Ramon Collazo for being my committee members. Your suggestions and comments are very valuable.

Second, I would like to thank my group members for their support and help. Thank Dr. Xiangyu Fu for guiding me into device optics. Thank Dr. Carr Hoi Yi Ho, Dr. Liping Zhu, Dr. Hyeonggeun Yu, Lei Lei, Juliana Mendes, Shichen Yin, Yash Mehta, Siliang He, and Dr. Amin Salehi for the productive collaborations. Thank Dr. Dong-Hun Shin, Dr. Cheng Peng, Dr. Shuyi Liu, Stephen Amoah, Dr. Xueping Yi, Dr. Chen Dong, Shuo Ding and Dr. Szuheng Ho for hanging out and the good times we spent together in the office.

Third, I would like to thank my collaborators from other groups. Thank Prof. Gundogdu and Dovletgeldi Seyitliyev for teaching me photo physics and spectroscopy. Thank Prof. Aram Amassian, Kasra Darabi, Prof. Chih-Hao Chang and Yi-An Chen for the collaborations.

Last but not the least, I would like to thank my parents for their support all the way along. Thank you for giving me the freedom to chase dreams.

TABLE OF CONTENTS

LIST OF TABLES

LIST OF FIGURES

CHAPTER 1: INTRODUCTION

Perovskites are a class of ceramic compounds with a chemical formula of ABX_3, whose very initial prototypical composition is titanium calcium oxide ($TiCaO_3$), firstly discovered as a mineral in 1839. In recent years, a new type of perovskite materials commonly denoted by metal-halide perovskites are attracting increasing attentions in various research communities by showing the potential of overthrowing the paradigm of conventional semiconductor industries established on silicon. For example, metal-halide perovskites have been found as a competitive candidate in the applications of the next-generation electronic and photonic devices, such as photovoltaics (PVs),[1,2] field effect transistors (FETs),[3] light-emitting diodes (LEDs),[4] and lasers,[5] due to their superior properties of tunable direct-bandgap,[6] defect tolerance,[7] long carrier diffusion length,[8] long carrier lifetime,[9] high photoluminescence quantum yield (PLQY),[10] narrow emission spectrum,[10] and solution-processibility.[11] To have a comprehensive understanding on the prospect of these emerging materials in the future semiconductor technologies, an introduction is given in this chapter, starting from the basic compositions and crystal structures followed by their superior properties and the implications in specific applications. After that, optoelectronic devices based on metal-halide perovskites, including photovoltaics, LEDs, and DFB lasers, are introduced by addressing the state-of-the-art performance, device structures and basic working mechanisms.

1.1 Metal-halide perovskite materials

1.1.1 Compositions and crystal structures

Like conventional perovskite materials, metal-halide perovskites also share the chemical formula of ABX_3. Here, the A-site cation is either a monovalent organic cation such as methylammonium (MA^+) and formamidinium (FA^+), or an alkali metal cation such as Cs^+ and Rb^+;

the B-site cation is a divalent transition metal cation, including but not limited to Pb^{2+}, Sn^{2+}, and Ge^{2+}; the X-site anion is a halide ion including Cl^-, Br^- and I^-.[12] Among these variations, the most prototypical composition is $MAPbI_3$ that has been intensively studied in the applications of photovoltaics, leading to a high efficiency comparable to polycrystalline silicon solar cells.[13] In addition, some other compositions are also gaining increasing popularity, such as Sn-based perovskites (e.g., $MASnI_3$) developed to reduce the environmental contamination caused by Pb,[14] and Cs-based all-inorganic perovskites (e.g., $CsPbI_3$) for a better stability in the operation of optoelectronic devices.[15] It should also be noted that each ionic site can be alloyed, further enlarging the tunability of the optoelectronic properties. For example, by fine-tuning the composition of the X-site through mixing different halide ions (e.g., $MAPbCl_xBr_yCl_{3-x-y}$), different bandgaps covering the full visible spectrum can be achieved,[16] which is a distinct advantage in the applications of full color displays.

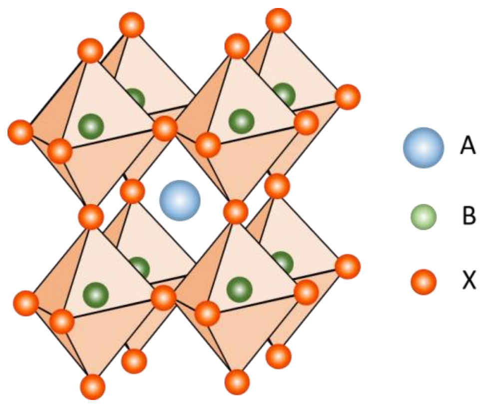

Fig.1.1 Schematic diagram showing the crystal structure of perovskites (ABX_3).

The crystal structure of metal-halide perovskites can be visualized as a 3-dimentional network formed by corner-sharing octahedra ($[BX_6]^{4-}$), where the A-site cations fit into the interstitial sites, as is shown in **Fig.1.1**. The crystal symmetry of a specific composition can be estimated by the Goldschmidt tolerance factor: $t=(R_A+R_X)/\sqrt{2}(R_B+R_X)$, where R_A, R_B and R_X are the ionic radii of A, B and X ions, respectively.[17,18] For example, the crystal symmetry is cubic when t is between 0.9~1, hexagonal when t is larger than 1, and orthorhombic when t is less than 0.9. Compositions with t less than 0.813 or larger than 1.107 normally cannot form a stable perovskite crystal.[19] In addition to the composition, the temperature also has an impact on the crystal symmetry of metal-halide perovskites, which is often observed in temperature-dependent measurements, denoted by phase transition. For example, $MAPbI_3$ undergoes a tetragonal-to-cubic phase transition when the temperature is elevated above 327 K, and a tetragonal-to-orthorhombic phase transition when the temperature drops below 162 K.[20] For more detailed information about the crystal structures of metal-halide perovskites, including the experimental techniques and lattice parameters, a comprehensive review article wrote by Takeo Oku serves as a good reference.[12]

1.1.2 Electronic structures

The electronic structures of metal-halide perovskites provide fundamental insights for understanding their superior properties in specific applications. In general, to investigate their electronic structures, computational methods based on first principle calculations including many-body perturbation theory and density functional theory (DFT) are adopted to obtain the band structures theoretically.[21–23] Due to the existence of heavy elements like Pb and halogen, spin-orbital coupling plays an important role in the formation of molecular orbitals, and therefore is also taken into consideration to enhance the accuracy of the computational results.[24] According to these theoretical studies, the electronic structures near the band edge of perovskites is mainly contributed from the 3D network consisting of corner-sharing octahedra ($[BX_6]^{4-}$), while the A-site cations only contribute to electronic levels several eV below the valance band maximum (VBM), and thus mainly act as a scaffold to fill the voids of the 3D network to maintain a stable crystal structure.[25] Such a difference can be attributed to the different types of chemical bond.

The 3D network itself is formed with ionic bond, which is a much stronger interaction compared to the van der Waals force between the A-site cations and the 3D network.[26]

Taking $MAPbI_3$ as an example, the VBM is formed by an anti-bonding of Pb-6s and I-5p orbitals, while the conduction band minimum (CBM) is mainly constituted by Pb-6p orbitals.[25,27–29] The strong anti-bonding between the s and p orbitals at the VBM gives rise to a small effective mass of holes, while the strong spin-orbital coupling originated from the heavy atoms modifies the CBM leading to a small effective mass of electrons.[30] This combined mechanism accounts for the good bipolar charge transport observed in perovskites,[31] which facilitates the separation of photoexcited electron and hole pairs, and thus is one of the reasons for the excellent performance of perovskite PVs. As for MA cations, although they do not directly participate in the construction of band edge electronic levels, they can affect the dynamics of excited charge carriers, manifested by an enhanced electron-phonon coupling owing to their intrinsic dipole moment in combination with the freedom of reorientation under the weak van der Waals interaction.[32] Such an enhanced electron-phonon coupling leads to the formation of small polarons that has been found to act as charge traps and accelerate the photodegradation of perovskite PVs.[33–35] Therefore, replacing MA cations by other A-site cations with less dipole moment, such as FA^+ and Cs^+, has become a strategy to prolong the operational lifetime of perovskite PVs.[36,37]

Another important conclusion from the computational studies is that metal-halide perovskites are normally recognized as a direct bandgap material, meaning the CBM and the VBM have the same wavevector in the Brillouin zone.[25] This is particularly important in the applications of PVs. In contrast to silicon that has an indirect bandgap leading to a weak optical transition at the band edge, perovskites have been observed to show a sharp increase at the absorption onset due to their direct bandgap nature.[6] In addition, the absorption coefficient of

$MAPbI_3$ perovskite above the bandgap is on the order of 10^5 cm^{-1}, which is comparable to prototypical inorganic semiconductors like GaAs.[38,39] Given that $MAPbI_3$ has a direct bandgap of 1.6 eV, a $MAPbI_3$ active layer of 400 nm in thickness is thick enough to absorb more than 90% of incident visible light from solar illumination in thin-film solar cell structures,[39] which contributes to the merits of lightweight, flexibility and low material-consumption.

1.1.3 Defect properties

It is known that defects, especially point defects, play a significant role in manipulating the electronic properties of semiconductors in modern industries. This also applies to metal-halide perovskites. Like the studies on the electronic structures, the defect properties of perovskites are also mainly investigated by computational methods.[7,40–44] From these studies, two unique defect properties have been revealed. The first one is the so-called defect tolerance that has been used to explain many of the superior properties in perovskites.[7,40,42] Depending on the energy levels of point defects, we can categorize them into shallow defects whose energy level is located near the band edge, and deep defects whose energy level is within the bandgap. Shallow defects do not have much impact on the charge transport and recombination, while deep defects act as charge traps that can slow down carrier transport, and Shockley-Read-Hall centers that facilitate non-radiative recombination. According to the computational studies on $MAPbI_3$, the formation energy of deep defects such as I_{Pb}, I_{MA}, Pb_i and Pb_I is in the range of several eV, leading to a small density of deep defects.[40] Other defects that exhibit a low formation energy of below 1 eV, such as MA_i, V_{MA}, I_i, V_I, V_{Pb}, and MA_{Pb}, are found to be shallow defects.[40] Therefore, the dominant defects in perovskites are shallow defects, in part accounting for the long diffusion length and long lifetime of excited charge carriers.

Another unique defect property of perovskites is self-doping.[40,43,44] Although perovskites are generally regarded as intrinsic bipolar charge transport semiconductors, they can be tuned from p-type dominant conduction to n-type dominant conduction according to the synthesis conditions.[44] Introducing impurity elements into a semiconductor to modify its conduction property is a common strategy, known as external doping, whereas the intrinsic defects can also act as donors or acceptors to provide excess electrons or holes, known as self-doping. In $MAPbI_3$ perovskite, V_I is the major donor defect leading to n-type doping, while V_{Pb} is the major acceptor defect leading to p-type doping.[44] By controlling the molar ratio of MAI and PbI_2 precursors during synthesis, the relative density of V_I and V_{Pb} can be manipulated, resulting in desired conduction properties.[44] For example, PbI_2-rich $MAPbI_3$ exhibits n-type conduction, while PbI_2-deficient $MAPbI_3$ exhibits p-type conduction.[44]

1.1.4 Charge transport properties

The charge transport properties of semiconductors are generally described by several interrelated parameters, including electron and hole effective mass (m^*), mobility (μ), diffusion coefficient (D), and diffusion length (L). Here, $MAPbI_3$ perovskite is used as an example to briefly address the typical values of these parameters as well as their mathematical correlations. As one of the most fundamental physical parameters in semiconductors, the effective mass can be directly determined by the electronic structures, as it is inversely proportional to the curvature of the corresponding energy band. From the calculated band structures of $MAPbI_3$, both electron and hole show a low m^* of around $0.2m_0$,[30] where m_0 is the mass of free electron, leading to a reduced effective mass of 0.1m. This theoretical prediction has been verified by experimental results, showing consistency within a reasonable range of error.[45]

The mobility is inversely proportional to the effective mass and proportional to scattering lifetime (τ_c) according to the Boltzmann transport equation under relaxation time approximation, $\mu = q\tau_c/m^*$, where q is the elementary charge. According to experimental results, the mobility in single crystal $MAPbI_3$ is just tens of cm^2/Vs,[46–48] much lower than that in silicon with a similar effective mass. This difference should be attributed the small τ_c in perovskites. However, this small τ_c cannot be further attributed to scatterings from point defects, as perovskites exhibit long carrier lifetime (τ, hundreds of ns) associated with defect tolerance.[9] To address this issue, one plausible explanation in the literature is to consider the lattice deformation induced by excited charge carriers.[49–51] Due to the softness of perovskite crystals, charge carriers can be easily coupled with phonons, forming large polarons that slow down the charge transport.[49] In addition to the mobility, this perspective can also explain the long carrier lifetime observed in perovskites, as the large polaron acts as a shield that protects the carrier from scattering by point defects and other charge carriers.[49]

The diffusion coefficient is related to the mobility through the Einstein relation, $D = \mu k_B T/q$, where k_B is the Boltzmann constant and T is temperature. For $MAPbI_3$, typical values of the diffusion coefficient are in the range of 0.05-0.2 cm^2/s.[52] The carrier diffusion length can be derived from the diffusion coefficient and carrier lifetime through the relation, $L = \sqrt{D\tau}$, based on which a long diffusion length up to 1 μm in perovskites is expected. This anticipation is consistent with experimental measurements that show a diffusion length of several μm in single crystal $MAPbI_3$ perovskites.[46,47] The long carrier diffusion length in combination with the large absorption coefficient leading to efficient collection of photoexcited carriers in perovskite PVs.

1.1.5 Optical properties

The mechanism of radiative recombination is a fundamental factor determining the optical properties of semiconductors. From the initial studies on the radiative recombination in $MAPbI_3$, there was a debate on whether the radiative recombination at room temperature is from Coulomb bounded excitons as in organic semiconductors or from free electron-hole pairs through band-to-band transition as in inorganic semiconductors.[53] Such a controversy stems from two reasons: (i) metal-halide perovskites are a type of hybrid materials consisting of both organic and inorganic components, thereby are expected to exhibit intermediate properties between organic and inorganic semiconductors; (ii) the exciton binding energy that is used to evaluate the strength of Coulomb interaction between electrons and holes has been reported by different groups with a large variation of values ranging from several meV to several tens of meV.[45,54,55] To resolve this debate, Saba et al. employed a combined analysis of theoretical modeling and time-resolved spectroscopy.[56] Through a numerical modelling on the absorption spectrum at the band edge, they found that the band edge absorption is enhanced by excitonic correlation; while through power-dependent transient PL, they found that the radiative recombination is mainly from conducting plasma of unbound but Coulomb-correlated electron-hole pairs. Nowadays, it is generally accepted that in $MAPbI_3$ perovskites, excitons are generated after excitation, which quickly dissociate into free electron-hole pairs due to a small exciton binding energy (smaller or comparable to the thermal energy 25 meV at RT), and light emission is driven by the correlated electron-hole plasma recombination.

In addition to the radiative recombination mechanism, the dynamics of other recombination pathways are also critical to the optical properties. As is illustrated in **Fig.1.2 ,** For perovskites, the excited charge carrier dynamics undergoes decoherence, thermalization, and cooling in the conduction band in a fast timescale of 1 ps, followed by different recombination pathways that relax the carriers to the valence band.[57] Since the excited charge carriers quickly dissociated into free electron-hole pairs, the recombination dynamics can be described by a rate equation: $\mathrm{dn}/\mathrm{dt} = -\mathrm{An} - \mathrm{Bn}^2 - \mathrm{Cn}^3$, where n is the density of the excited carriers; t is the time; A, B and C are the rate coefficients corresponding to monomolecular trap-assisted recombination, bimolecular radiative recombination, and three-body Auger recombination, respectively.[58,59] From the equation, trap-assisted recombination and Auger recombination are two non-emissive pathways, which compete with the radiative recombination.

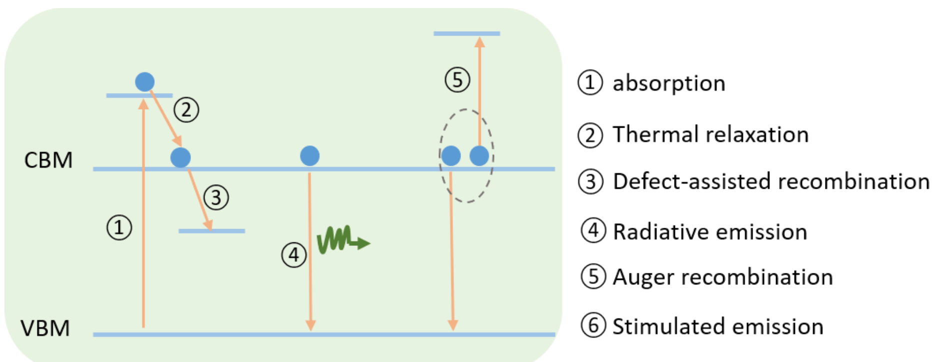

Fig.1.2 Schematic diagram showing different recombination dynamics in perovskites.

For solar cell applications, we want all the recombination pathways to be suppressed for an efficient collection of photoexcited carriers, and this happens to be the case in $MAPbI_3$ perovskites: the defect tolerance and the formation of large polarons leads to small values of A;[50,59] the weak interaction between electrons and holes leads to small values of B;[60] Auger recombination is negligible in the carrier density regime of solar cells.[59] This again explains the tremendous success of perovskites in solar cell applications. Nevertheless, for LED applications, we expect the radiative recombination to be promoted and the other two non-emissive pathways to be suppressed, especially the trap-assisted recombination. In this case, normal perovskites cannot fulfill the requirements due to the slow bimolecular radiative recombination and grain boundary defects.[60] To tackle this issue, a synergistic strategy consisting of exciton confinement and defect passivation has been widely adopted to improve the performance of perovskite LEDs through introducing low-dimensional structures in the perovskites,[61,62] which is elaborated in the subsequent section.

1.1.6 Low-dimensional perovskites

Low-dimensional perovskites can be fabricated by adding bulky organic cations, such as phenethylammonium cation (PEA^+) and n-butylammonium cation (BA^+).[63,64] Due to the large size of these organic cations, they cannot fit into the interstitial sites of the octahedra ($[BX_6]^{4-}$) network, leading to the formation of layered nanostructures, called Ruddlesden-Popper (RP) phases, or 2D phases, as is shown in **Fig.1.3**. The 2D phases can have different dimensionalities determined by the number of inorganic octahedra layers between neighboring organic spacers. Such a dimensionality is normally denoted by an index n, and the chemical formula of any 2D phases can be expressed by $C_2A_{n-1}B_nX_{3n+1}$, where C is the bulky organic cation. It should be noted that when n=1, the chemical formula becomes C_2BX_4, where A-site cations no longer exist in the crystal structure, and when n goes to infinity, the chemical formula returns to that of 3D perovskites. From the perspective of stoichiometry, we should be able to control the dimensionality of a low-dimensional perovskite by tuning the molar ratios among the precursors like PEAI, MAI and PbI_2. However, due to the robust solution-process, the resulting perovskite films contain a mixture of phases with different indices ranging from n=1 to infinity.[61,62] This leads to the complexity of the nanostructures in low-dimensional perovskites and is also the reason why they are called quasi-2D perovskites. For comparison, normal perovskites like $MAPbI_3$ are called 3D perovskites.

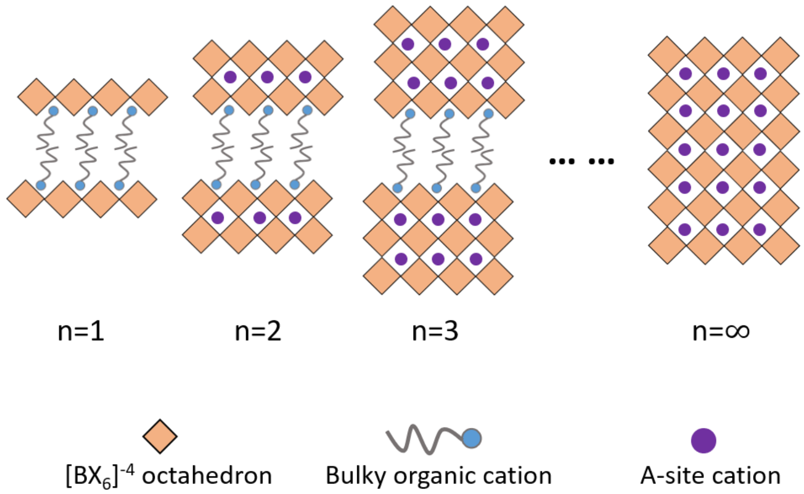

Fig.1.3 Schematic diagram showing the structure of Ruddlesden-Popper (RP) perovskite.

Quasi-2D perovskites give rise to three important effects that have significantly promoted their applications in light-emitting devices. First, the bandgap of different phases is determined by their indices according to quantum confinement, and therefore the bandgap increases with the decrease of the index.[61,62] Such an energetic landscape in combination with the mixed phases in quasi-2D perovskites create a self-assembled quantum-well system, where the excited charge carriers funnel from the larger bandgap phases to the smaller bandgap phases, known as energy transfer. It has been experimentally determined by transient absorption measurements that the energy transfer process can be very fast, within 1 ps,[65] which is much shorter than the timescale of radiative recombination. Therefore, light emission solely comes from the large bandgap phases. This is a distinct advantage in laser applications, as the fast energy transfer can promote the carrier accumulation in the small bandgap phases, thereby facilitating population inversion.[65] Second, different from 3D perovskites where excited charge carriers exist as free electron-hole pairs, in quasi-2D perovskites, excitons are used to describe the radiative recombination process due to their nonnegligible exciton binding energy.[60] This large exciton binding energy is originated from quantum confinement and dielectric confinement in the self-assembled quantum-well system, leading to a faster radiative recombination rate that is beneficial to LED applications. Third, the bulky organic cations contain an amine group that can passivate the grain boundary defects.[60] In this case, the trap-assisted non-radiative recombination can be effectively suppressed, leading to high PLQY and efficient perovskite LEDs.

1.2 Optoelectronic devices based on halide perovskites

1.2.1 Perovskite photovoltaics

The first successful application of metal-halide perovskites is in photovoltaics, manifested by an unprecedented improvement in power conversion efficiency (PCE) from 3.8 % to 25% in just one decade.[66,67] In general, due to the ambipolar transport property of perovskites, the device structure of perovskite PVs adopts p-i-n configuration and can be categorized into two types.[68] The first type is conventional structure (**Fig.1.4a**), where a transparent conducting metal oxide like indium tin oxide (ITO) or fluorine doped tin oxide (FTO) is used as the bottom cathode on a glass substrate, followed by an electron transporting layer (ETL), an active layer (perovskite), a hole transporting layer (HTL), and a reflective metal anode. The materials commonly used for the ETL is n-type semiconducting metal oxides such as TiO_2, ZnO and SnO_2. The HTL is made from p-type organic semiconductors such as 2,2',7,7'-Tetrakis[N,N-di(4-methoxyphenyl)amino]-9,9'-spirobifluorene (spiro-MeOTAD). The anode is usually made by noble metals like gold and silver. The second type is called inverted structure (**Fig.1.4b**), where the transparent anode is at the bottom, followed by a HTL, an active layer, an ETL, and a metal cathode. In this case, the HTL can be made from p-type polymers such as Poly(4-butyltriphenylamine) (Poly-TPD), or inorganic p-type metal oxides such as NiO_x. The ETL is usually made from n-type fullerene derivatives like phenyl-C61-butyric acid methyl ester (PCBM). The cathode can be made from low work function metals such as aluminum.

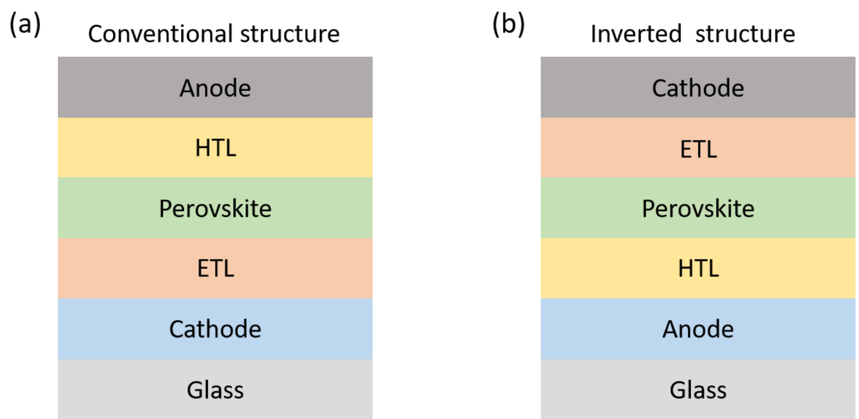

Fig.1.4 (a) Conventional structure of perovskite solar cells. (b) Inverted structure of perovskite solar cells.

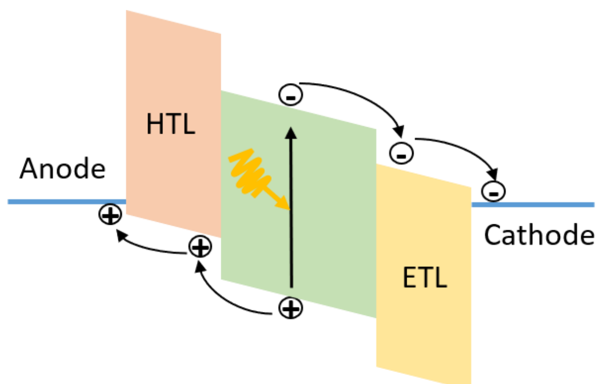

Fig.1.5 Schematic energy diagram of each functional layers in perovskite PVs showing the process of photocurrent generation.

The basic working mechanism of perovskite PVs is illustrated in **Fig. 1.5**.[69] This diagram shows the approximate energy levels of each functional layers and the critical steps of photocurrent generation. Upon the absorption of a photon by the perovskite active layer, a pair of electron and hole is generated, which stay at the conduction band and the valence band, respectively. Due to the small exciton binding energy, the electron and hole are separated and transported to the ETL and the HTL, respectively, driven by the built-in potential. Lastly, the electron is collected by the cathode through the transport of the ETL and the hole is collected by the anode through the transport of the HTL, leading to the generation of photocurrent passing through the external circuit. From the working mechanism, it can be realized that not only the properties of the active layer are important for efficient photocurrent generation, but also the other functional layers especially the ETL and HTL play a critical role. More importantly, the interface properties between adjacent layers such as ETL/perovskite and HTL/perovskite also have a significant impact on the final device performance.[70]

1.2.2 Perovskite light-emitting diodes

Following the prosperity of perovskite PVs, an increasing effort has been devoted to exploring the potential of perovskite materials in LED applications, and this leads to a fast increase in the external quantum efficiency (EQE) from less than 1% to over 20% in both green and red spectra.[71,72] The device structure of perovskite LEDs is intrinsically similar to that of perovskite PVs, where a perovskite layer is sandwiched by an ETL and a HTL. There are also two types of structures for perovskite LEDs. One is like the conventional structure of perovskite photovoltaics (**Fig.1.4a**), where the cathode is at the bottom, followed by an ETL, a perovskite emitting layer, a HTL and a metal anode. Another structure inverted (**Fig.1.4b**), where the anode is at the bottom, followed by a HTL, a perovskite emitting layer, an ETL and a metal cathode. In both structures, the materials used for each layer are like that of perovskite PVs. Nevertheless, perovskite LEDs still differ from perovskite PVs in terms of the perovskite materials used. As we mentioned previously, 3D perovskites are not suitable for LED applications due to their slow bimolecular recombination and grain boundary defects.[60] Therefore, to date, high efficiency perovskite LEDs are normally fabricated with quasi-2D perovskites.[72]

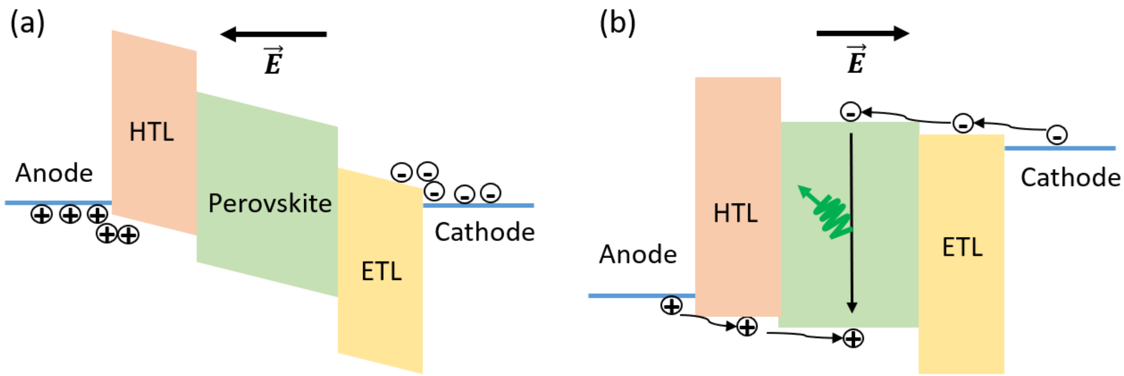

Fig.1.6 Schematic energy diagram of each functional layers in perovskite LEDs showing the process of charge injection and recombination. (a) Before turn-on. (c) After turn-on.

The working mechanism of perovskite LEDs is a reverse process of that in perovskite PVs, as is depicted in **Fig. 1.6**.[73] Instead of generating electric current by absorbing photons, light is emitted by current injection in perovskite LEDs. Without applying an external bias, the band structure is tilted, associated with the formation of a built-in potential. Upon the application of a small bias (less than the built-in potential), the overall electric field inside the device is still in the opposite direction of the external bias, leading to negligible current injection (**Fig.1.6a**). As the external bias is further increased to overcome the built-in potential, the total electric field in the device is aligned with the bias, leading to current injection (**Fig.1.6b**). This transition is called turn-on, and the amount of voltage that is needed to give sufficient current injection is called turn-on volage. In general, the turn-on voltage is mainly determined by the bandgap of the perovskite material. Above the turn-on voltage, electrons and holes can be injected from the cathode and the anode, respectively, and then transported through the ETL and the HTL, respectively, into the perovskite emitting layer where they recombine radiatively to emit photons. From this working mechanism, two major aspects play important roles in determining the device efficiency: one is charge carrier recombination and the other is charge carrier injection. The former is mainly determined by the perovskite emitting layer and can be tackled by compositional engineering to improve its PLQY and charge transport. The latter is mainly affected by the properties of other functional layers as well as their interfaces. In this case, device engineering is employed to achieve efficient and balanced charge injection.

1.2.3 Perovskite DFB lasers

In addition to PVs and LEDs, perovskites have also been found as a good candidate of gain media in laser applications.[5] Nevertheless, the development of perovskite lasers is still in its infancy, as the room-temperature laser from perovskites so far can be only achieved by pulsed optical pumping (e.g., fs pulsed laser). One exception is a work reported in September 2020, where continuous-wave optically pumped laser at room temperature is demonstrated from a quasi-2D perovskite.[74] However, in this work, the laser emission is very unstable, manifested by a fast degradation by 80% within 1 hr. To date, electrically driven laser from perovskites has not been realized yet. These obstacles are mainly originated from the instability of perovskite materials, which degrade under strong electric or optical stress due to ion migration.[75] To overcome these challenges, many research groups are working on improving the electric and optical stability of perovskites through material engineering.

The working mechanism of a perovskite laser consist of two aspects: gain medium and optical cavity.[5] In a perovskite gain medium, optical pumping leads to the excitation of electrons and holes, which subsequently undergo intraband relaxation and accumulate at the bottom of the conduction band and the top of the valance band, respectively. Such accumulations result in the formation of quasi-fermi level of electrons and quasi-fermi level of holes. When the pumping intensity is increased beyond a certain value, the energy difference between the quasi-fermi level of electrons and the quasi-fermi level of holes exceeds the bandgap, causing the stimulated emission rate larger than the absorption rate. In this case, photons traveling through the perovskite is amplified, leading to optical gain. Without optical cavity, the optical gain only gives rise to amplified spontaneous emission (ASE) whose threshold is commonly used to evaluate the potential of a material in laser applications. When an optical cavity is incorporated, the cavity provides an optical feedback that leads to the build-up of photons at the resonant frequency of the cavity, which eventually suppresses all the other optical modes, resulting in coherent, directional, and monochromatic light emission, known as laser.

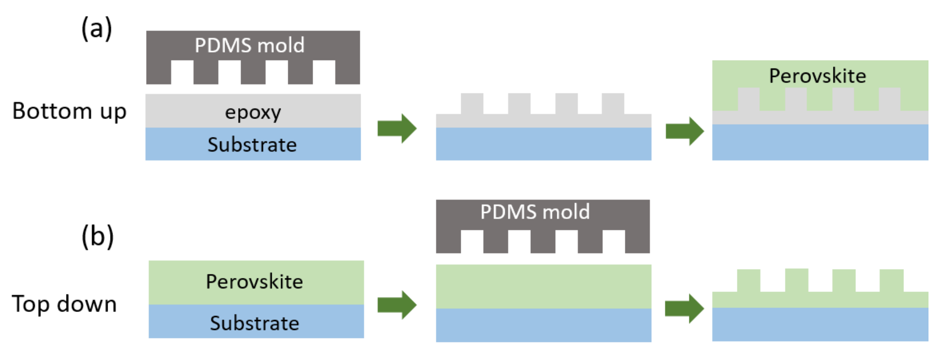

Fig.1.7 Different ways of fabricating perovskite DFB structure. (a) Bottom up. (b) Top down.

Among different perovskite laser cavities, distributed feedback (DFB) cavities have attracted the most attention due to their low fabrication-cost and single-mode operation.[76,77] A DFB cavity is a periodic variation of refractive index that provides optical feedback through Bragg diffraction. In general, perovskite DFB lasers can be fabricated with two types of configurations. The first one is called bottom-up structure, where a perovskite thin film is coated on a substrate with periodic surface relief,[76,77] as shown in **Fig.1.7a**. The corrugated substrate can be fabricated by photolithography, e-beam lithography, or nanoimprint lithography. The second configuration is top-down structure (**Fig.1.7b**), where the perovskite film is nanopatterned from the top by thermal nanoimprint lithography, and the substrate is planar.[78] Both structures provide a periodic index variation, with the former between the perovskite and the substrate, and the latter between the perovskite and the air. The resonant wavelength (λ_R) of the DFB cavity is determined by the effective (n_{eff}) of the waveguide mode and the index variation period (Λ) through $\lambda_R = 2m\Lambda n_{eff}$, where m determines the laser emission direction. The laser emission is from the edge when m=1, and from the surface when m=2. The design of the DFB cavity (selection of Λ) should also consider the emission spectrum of the gain medium. For example, in a surface-emitting DFB laser that uses a green-emitting perovskite (e.g., $MAPbBr_3$) as the gain medium, n_{eff} can be 1.7, and the desired λ_R can be 530 nm, leading to Λ at 312 nm.

REFERENCES

[1] D. Li, D. Zhang, K. S. Lim, Y. Hu, Y. Rong, A. Mei, N. G. Park, H. Han, A Review on Scaling Up Perovskite Solar Cells, *Adv. Funct. Mater.* **2020**, 2008621, 1–27.

[2] M. A. Green, A. Ho-Baillie, H. J. Snaith, The Emergence of Perovskite Solar Cells, *Nat. Photonics* **2014**, 8, 506–514.

[3] Y. Liu, P. A. Chen, Y. Hu, Recent Developments in Fabrication and Performance of Metal Halide Perovskite Field-Effect Transistors, *J. Mater. Chem. C* **2020**, 8, 16691–16715.

[4] Q. Van Le, H. W. Jang, S. Y. Kim, Recent Advances toward High-Efficiency Halide Perovskite Light-Emitting Diodes: Review and Perspective, *Small Methods* **2018**, 2, 1700419.

[5] L. Lei, Q. Dong, K. Gundogdu, F. So, Metal Halide Perovskites for Laser Applications, *Adv. Funct. Mater.* **2021**, 2010144, 2010144.

[6] C. C. Stoumpos, C. D. Malliakas, M. G. Kanatzidis, Semiconducting Tin and Lead Iodide Perovskites with Organic Cations: Phase Transitions, High Mobilities, and near-Infrared Photoluminescent Properties, *Inorg. Chem.* **2013**, 52, 9019–9038.

[7] K. X. Steirer, P. Schulz, G. Teeter, V. Stevanovic, M. Yang, K. Zhu, J. J. Berry, Defect Tolerance in Methylammonium Lead Triiodide Perovskite, *ACS Energy Lett.* **2016**, 1, 360–366.

[8] M. J. P. Alcocer, T. Leijtens, L. M. Herz, A. Petrozza, H. J. Snaith, Electron-Hole Diffusion Lengths Exceeding Trihalide Perovskite Absorber, *Science (80-.).* **2013**, 342, 341–344.

[9] M. Zhang, H. Yu, M. Lyu, Q. Wang, J. H. Yun, L. Wang, Composition-Dependent Photoluminescence Intensity and Prolonged Recombination Lifetime of Perovskite CH3NH3PbBr3−x Clxfilms, *Chem. Commun.* **2014**, 50, 11727–11730.

[10] L. Protesescu, S. Yakunin, M. I. Bodnarchuk, F. Krieg, R. Caputo, C. H. Hendon, R. X. Yang, A. Walsh, M. V. Kovalenko, Nanocrystals of Cesium Lead Halide Perovskites (CsPbX3, X = Cl, Br, and I): Novel Optoelectronic Materials Showing Bright Emission

with Wide Color Gamut, *Nano Lett.* **2015**, 15, 3692–3696.

[11] F. Guo, W. He, S. Qiu, C. Wang, X. Liu, K. Forberich, C. J. Brabec, Y. Mai, Sequential Deposition of High-Quality Photovoltaic Perovskite Layers via Scalable Printing Methods, *Adv. Funct. Mater*. **2019**, 29, 1–9.

[12] T. Oku, Crystal Structures of Perovskite Halide Compounds Used for Solar Cells, *Rev. Adv. Mater. Sci.* **2020**, 59, 264–305.

[13] M. Jeong, I. W. Choi, E. M. Go, Y. Cho, M. Kim, B. Lee, S. Jeong, Y. Jo, H. W. Choi, J. Lee, J. H. Bae, S. K. Kwak, D. S. Kim, C. Yang, Stable Perovskite Solar Cells with Efficiency Exceeding 24.8% and 0.3-V Voltage Loss, *Science (80-.).* **2020**, 369, 1615–1620.

[14] F. Gu, Z. Zhao, C. Wang, H. Rao, B. Zhao, Z. Liu, Z. Bian, C. Huang, Lead-Free Tin-Based Perovskite Solar Cells: Strategies Toward High Performance, *Sol. RRL* **2019**, 3, 1–26.

[15] W. Chen, X. Li, Y. Li, Y. Li, A Review: Crystal Growth for High-Performance All-Inorganic Perovskite Solar Cells, *Energy Environ. Sci.* **2020**, 13, 1971–1996.

[16] S. Pathak, N. Sakai, F. Wisnivesky Rocca Rivarola, S. D. Stranks, J. Liu, G. E. Eperon, C. Ducati, K. Wojciechowski, J. T. Griffiths, A. A. Haghighirad, A. Pellaroque, R. H. Friend, H. J. Snaith, Perovskite Crystals for Tunable White Light Emission, *Chem. Mater.* **2015**, 27, 8066–8075.

[17] W. Travis, E. N. K. Glover, H. Bronstein, D. O. Scanlon, R. G. Palgrave, On the Application of the Tolerance Factor to Inorganic and Hybrid Halide Perovskites: A Revised System, *Chem. Sci.* **2016**, 7, 4548–4556.

[18] Z. Li, M. Yang, J. S. Park, S. H. Wei, J. J. Berry, K. Zhu, Stabilizing Perovskite Structures by Tuning Tolerance Factor: Formation of Formamidinium and Cesium Lead Iodide Solid-State Alloys, *Chem. Mater*. **2016**, 28, 284–292.

[19] C. Li, X. Lu, W. Ding, L. Feng, Y. Gao, Z. Guo, Formability of ABX 3 (X = F, Cl, Br, I) Halide Perovskites, *Acta Crystallogr. Sect. B Struct. Sci.* **2008**, 64, 702–707.

[20] C. Quarti, E. Mosconi, J. M. Ball, V. D'Innocenzo, C. Tao, S. Pathak, H. J. Snaith, A. Petrozza, F. De Angelis, Structural and Optical Properties of Methylammonium Lead Iodide across the Tetragonal to Cubic Phase Transition: Implications for Perovskite Solar Cells, *Energy Environ. Sci.* **2016**, 9, 155–163.

[21] J. S. Manser, J. A. Christians, P. V. Kamat, Intriguing Optoelectronic Properties of Metal Halide Perovskites, *Chem. Rev.* **2016**, 116, 12956–13008.

[22] F. Brivio, K. T. Butler, A. Walsh, M. Van Schilfgaarde, Relativistic Quasiparticle Self-Consistent Electronic Structure of Hybrid Halide Perovskite Photovoltaic Absorbers, *Phys. Rev. B - Condens. Matter Mater. Phys.* **2014**, 89, 1–6.

[23] Y. Y. Pan, Y. H. Su, C. H. Hsu, L. W. Huang, C. C. Kaun, The Electronic Structure of Organic-Inorganic Hybrid Perovskite Solar Cell: A First-Principles Analysis, *Comput. Mater. Sci.* **2016**, 117, 573–578.

[24] J. Even, L. Pedesseau, J. M. Jancu, C. Katan, Importance of Spin-Orbit Coupling in Hybrid Organic/Inorganic Perovskites for Photovoltaic Applications, *J. Phys. Chem. Lett.* **2013**, 4, 2999–3005.

[25] A. Filippetti, A. Mattoni, Hybrid Perovskites for Photovoltaics: Insights from First Principles, *Phys. Rev. B - Condens. Matter Mater. Phys.* **2014**, 89, 1–8.

[26] Y. Wang, T. Gould, J. F. Dobson, H. Zhang, H. Yang, X. Yao, H. Zhao, Density Functional Theory Analysis of Structural and Electronic Properties of Orthorhombic Perovskite CH3NH3PbI3, *Phys. Chem. Chem. Phys.* **2014**, 16, 1424–1429.

[27] J. Kim, S. C. Lee, S. H. Lee, K. H. Hong, Importance of Orbital Interactions in Determining Electronic Band Structures of Organo-Lead Iodide, *J. Phys. Chem. C* **2015**, 119, 4627–4634.

[28] L. Lang, J. H. Yang, H. R. Liu, H. J. Xiang, X. G. Gong, First-Principles Study on the Electronic and Optical Properties of Cubic ABX3 Halide Perovskites, *Phys. Lett. Sect. A Gen. At. Solid State Phys.* **2014**, 378, 290–293.

[29] F. Brivio, A. B. Walker, A. Walsh, Structural and Electronic Properties of Hybrid Perovskites for High-Efficiency Thin-Film Photovoltaics from First-Principles, *APL Mater.* **2013**, 1, DOI 10.1063/1.4824147.

[30] G. Giorgi, J. I. Fujisawa, H. Segawa, K. Yamashita, Small Photocarrier Effective Masses Featuring Ambipolar Transport in Methylammonium Lead Iodide Perovskite: A Density Functional Analysis, *J. Phys. Chem. Lett.* **2013**, 4, 4213–4216.

[31] G. Xing, N. Mathews, S. Sun, S. S. Lim, Y. M. Lam, M. Gratzel, S. Mhaisalkar, T. C. Sum, Long-Range Balanced Electron- and Hole-Transport Lengths in Organic-Inorganic CH3NH3PbI3, *Science (80-.).* **2013**, 342, 344–347.

[32] A. J. Neukirch, W. Nie, J. C. Blancon, K. Appavoo, H. Tsai, M. Y. Sfeir, C. Katan, L. Pedesseau, J. Even, J. J. Crochet, G. Gupta, A. D. Mohite, S. Tretiak, Polaron Stabilization by Cooperative Lattice Distortion and Cation Rotations in Hybrid Perovskite Materials, *Nano Lett.* **2016**, 16, 3809–3816.

[33] X. Gong, O. Voznyy, A. Jain, W. Liu, R. Sabatini, Z. Piontkowski, G. Walters, G. Bappi, S. Nokhrin, O. Bushuyev, M. Yuan, R. Comin, D. McCamant, S. O. Kelley, E. H. Sargent, Electron-Phonon Interaction in Efficient Perovskite Blue Emitters, *Nat. Mater.* **2018**, 17, 550–556.

[34] X. Wu, M. T. Trinh, D. Niesner, H. Zhu, Z. Norman, J. S. Owen, O. Yaffe, B. J. Kudisch, X.-Y. Y. Zhu, Trap States in Lead Iodide Perovskites, *J. Am. Chem. Soc.* **2015**, 137, 2089–2096.

[35] W. Nie, J. C. Blancon, A. J. Neukirch, K. Appavoo, H. Tsai, M. Chhowalla, M. A. Alam, M. Y. Sfeir, C. Katan, J. Even, S. Tretiak, J. J. Crochet, G. Gupta, A. D. Mohite, Light-Activated Photocurrent Degradation and Self-Healing in Perovskite Solar Cells, *Nat. Commun.* **2016**, 7, 1–9.

[36] A. J. Neukirch, I. I. Abate, L. Zhou, W. Nie, H. Tsai, L. Pedesseau, J. Even, J. J. Crochet, A. D. Mohite, C. Katan, S. Tretiak, Geometry Distortion and Small Polaron Binding Energy Changes with Ionic Substitution in Halide Perovskites, *J. Phys. Chem. Lett.* **2018**, 9, 7130–

7136.

[37] J.-W. W. Lee, D.-H. H. Kim, H.-S. S. Kim, S.-W. W. Seo, S. M. Cho, N.-G. G. Park, Formamidinium and Cesium Hybridization for Photo- and Moisture-Stable Perovskite Solar Cell, *Adv. Energy Mater.* **2015**, 5, 1501310.

[38] E. T. Hoke, D. J. Slotcavage, E. R. Dohner, A. R. Bowring, H. I. Karunadasa, M. D. McGehee, Reversible Photo-Induced Trap Formation in Mixed-Halide Hybrid Perovskites for Photovoltaics, *Chem. Sci.* **2015**, 6, 613–617.

[39] S. De Wolf, J. Holovsky, S. J. Moon, P. Löper, B. Niesen, M. Ledinsky, F. J. Haug, J. H. Yum, C. Ballif, Organometallic Halide Perovskites: Sharp Optical Absorption Edge and Its Relation to Photovoltaic Performance, *J. Phys. Chem. Lett.* **2014**, 5, 1035–1039.

[40] W. J. Yin, T. Shi, Y. Yan, Unusual Defect Physics in CH3NH3PbI3 Perovskite Solar Cell Absorber, *Appl. Phys. Lett.* **2014**, 104, 063903.

[41] A. Buin, P. Pietsch, J. Xu, O. Voznyy, A. H. Ip, R. Comin, E. H. Sargent, Materials Processing Routes to Trap-Free Halide Perovskites, *Nano Lett.* **2014**, 14, 6281–6286.

[42] D. Meggiolaro, S. G. Motti, E. Mosconi, A. J. Barker, J. Ball, C. Andrea Riccardo Perini, F. Deschler, A. Petrozza, F. De Angelis, Iodine Chemistry Determines the Defect Tolerance of Lead-Halide Perovskites, *Energy Environ. Sci.* **2018**, 11, 702–713.

[43] T. Shi, W. J. Yin, F. Hong, K. Zhu, Y. Yan, Unipolar Self-Doping Behavior in Perovskite CH3NH3PbBr3, *Appl. Phys. Lett.* **2015**, 106, DOI 10.1063/1.4914544.

[44] Q. Wang, Y. Shao, H. Xie, L. Lyu, X. Liu, Y. Gao, J. Huang, Qualifying Composition Dependent p and n Self-Doping in CH3NH3PbI3, *Appl. Phys. Lett.* **2014**, 105, DOI 10.1063/1.4899051.

[45] A. Miyata, A. Mitioglu, P. Plochocka, O. Portugall, J. T. W. Wang, S. D. Stranks, H. J. Snaith, R. J. Nicholas, Direct Measurement of the Exciton Binding Energy and Effective Masses for Charge Carriers in Organic-Inorganic Tri-Halide Perovskites, *Nat. Phys.* **2015**, 11, 582–587.

[46] Q. Dong, Y. Fang, Y. Shao, P. Mulligan, J. Qiu, L. Cao, J. Huang, Electron-Hole Diffusion Lengths > 175 Mm in Solution-Grown CH 3 NH 3 PbI 3 Single Crystals, *Science (80-.).* **2015**, 347, 967–970.

[47] D. Shi, V. Adinolfi, R. Comin, M. Yuan, E. Alarousu, A. Buin, Y. Chen, S. Hoogland, A. Rothenberger, K. Katsiev, Y. Losovyj, X. Zhang, P. A. Dowben, O. F. Mohammed, E. H. Sargent, O. M. Bakr, Low Trap-State Density and Long Carrier Diffusion in Organolead Trihalide Perovskite Single Crystals, *Science (80-.).* **2015**, 347, 519–522.

[48] M. I. Saidaminov, A. L. Abdelhady, B. Murali, E. Alarousu, V. M. Burlakov, W. Peng, I. Dursun, L. Wang, Y. He, G. MacUlan, A. Goriely, T. Wu, O. F. Mohammed, O. M. Bakr, High-Quality Bulk Hybrid Perovskite Single Crystals within Minutes by Inverse Temperature Crystallization, *Nat. Commun.* **2015**, 6, 1–6.

[49] X. Y. Zhu, V. Podzorov, Charge Carriers in Hybrid Organic-Inorganic Lead Halide Perovskites Might Be Protected as Large Polarons, *J. Phys. Chem. Lett.* **2015**, 6, 4758–4761.

[50] K. Miyata, D. Meggiolaro, M. Tuan Trinh, P. P. Joshi, E. Mosconi, S. C. Jones, F. De Angelis, X.-Y. Y. Zhu, M. T. Trinh, P. P. Joshi, E. Mosconi, S. C. Jones, F. De Angelis, X.-Y. Y. Zhu, Large Polarons in Lead Halide Perovskites, *Sci. Adv.* **2017**, 3, e1701217.

[51] K. Miyata, T. L. Atallah, X.-Y. Y. Zhu, Lead Halide Perovskites: Crystal-Liquid Duality, Phonon Glass Electron Crystals, and Large Polaron Formation, *Sci. Adv.* **2017**, 3, e1701469.

[52] T. M. Brenner, D. A. Egger, L. Kronik, G. Hodes, D. Cahen, Hybrid Organic - Inorganic Perovskites: Low-Cost Semiconductors with Intriguing Charge-Transport Properties, *Nat. Rev. Mater.* **2016**, 1, 1–16.

[53] Y. Jiang, X. Wang, A. Pan, Properties of Excitons and Photogenerated Charge Carriers in Metal Halide Perovskites, *Adv. Mater.* **2019**, 31, 1806671.

[54] M. Saba, F. Quochi, A. Mura, G. Bongiovanni, Excited State Properties of Hybrid Perovskites, *Acc. Chem. Res.* **2016**, 49, 166–173.

[55] K. Tanaka, T. Takahashi, T. Ban, T. Kondo, K. Uchida, N. Miura, Comparative Study on the Excitons in Lead-Halide-Based Perovskite-Type Crystals CH3NH3PbBr3 CH3NH 3PbI3, *Solid State Commun.* **2003**, 127, 619–623.

[56] M. Saba, M. Cadelano, D. Marongiu, F. Chen, V. Sarritzu, N. Sestu, C. Figus, M. Aresti, R. Piras, A. Geddo Lehmann, C. Cannas, A. Musinu, F. Quochi, A. Mura, G. Bongiovanni, Correlated Electron–Hole Plasma in Organometal Perovskites, *Nat. Commun.* **2014**, 5, 5049.

[57] L. M. Herz, Charge-Carrier Dynamics in Organic-Inorganic Metal Halide Perovskites, *Annu. Rev. Phys. Chem.* **2016**, 67, 65–89.

[58] C. Wehrenfennig, G. E. Eperon, M. B. Johnston, H. J. Snaith, L. M. Herz, High Charge Carrier Mobilities and Lifetimes in Organolead Trihalide Perovskites, *Adv. Mater.* **2014**, 26, 1584–1589.

[59] Y. Yamada, T. Nakamura, M. Endo, A. Wakamiya, Y. Kanemitsu, Photocarrier Recombination Dynamics in Perovskite CH 3 NH 3 PbI 3 for Solar Cell Applications, *J. Am. Chem. Soc.* **2014**, 136, 11610–11613.

[60] G. Xing, B. Wu, X. Wu, M. Li, B. Du, Q. Wei, J. Guo, E. K. L. L. Yeow, T. C. Sum, W. Huang, Transcending the Slow Bimolecular Recombination in Lead-Halide Perovskites for Electroluminescence, *Nat. Commun.* **2017**, 8, 14558.

[61] M. Yuan, L. N. N. Quan, R. Comin, G. Walters, R. Sabatini, O. Voznyy, S. Hoogland, Y. Zhao, E. M. M. Beauregard, P. Kanjanaboos, Z. Lu, D. H. H. Kim, E. H. H. Sargent, Perovskite Energy Funnels for Efficient Light-Emitting Diodes, *Nat. Nanotechnol.* **2016**, 11, 872–877.

[62] N. Wang, L. Cheng, R. Ge, S. Zhang, Y. Miao, W. Zou, C. Yi, Y. Sun, Y. Cao, R. Yang, Y. Wei, Q. Guo, Y. Ke, M. Yu, Y. Jin, Y. Liu, Q. Ding, D. Di, L. Yang, G. Xing, H. Tian, C. Jin, F. Gao, R. H. H. Friend, J. Wang, W. Huang, Perovskite Light-Emitting Diodes Based on Solution-Processed Self-Organized Multiple Quantum Wells, *Nat. Photonics* **2016**, 10, 699–704.

[63] D. H. Cao, C. C. Stoumpos, O. K. Farha, J. T. Hupp, M. G. Kanatzidis, 2D Homologous Perovskites as Light-Absorbing Materials for Solar Cell Applications, *J. Am. Chem. Soc.* **2015**, 137, 7843–7850.

[64] I. C. Smith, E. T. Hoke, D. Solis-Ibarra, M. D. McGehee, H. I. Karunadasa, A Layered Hybrid Perovskite Solar-Cell Absorber with Enhanced Moisture Stability, *Angew. Chemie - Int. Ed.* **2014**, 53, 11232–11235.

[65] L. Lei, D. Seyitliyev, S. Stuard, J. Mendes, Q. Dong, X. Fu, Y. Chen, S. He, X. Yi, L. Zhu, C. Chang, H. Ade, K. Gundogdu, F. So, Efficient Energy Funneling in Quasi-2D Perovskites: From Light Emission to Lasing, *Adv. Mater.* **2020**, 32, 1906571.

[66] A. Kojima, K. Teshima, Y. Shirai, T. Miyasaka, Organometal Halide Perovskites as Visible-Light Sensitizers for Photovoltaic Cells, *J. Am. Chem. Soc.* **2009**, 131, 6050–6051.

[67] J. J. Yoo, G. Seo, M. R. Chua, T. G. Park, Y. Lu, F. Rotermund, Y. K. Kim, C. S. Moon, N. J. Jeon, J. P. Correa-Baena, V. Bulović, S. S. Shin, M. G. Bawendi, J. Seo, Efficient Perovskite Solar Cells via Improved Carrier Management, *Nature* **2021**, 590, 587–593.

[68] P. Roy, N. Kumar Sinha, S. Tiwari, A. Khare, A Review on Perovskite Solar Cells: Evolution of Architecture, Fabrication Techniques, Commercialization Issues and Status, *Sol. Energy* **2020**, 198, 665–688.

[69] P. Lopez-Varo, J. A. Jiménez-Tejada, M. García-Rosell, S. Ravishankar, G. Garcia-Belmonte, J. Bisquert, O. Almora, Device Physics of Hybrid Perovskite Solar Cells: Theory and Experiment, *Adv. Energy Mater.* **2018**, 8, DOI 10.1002/aenm.201702772.

[70] J. Chen, N. G. Park, Materials and Methods for Interface Engineering toward Stable and Efficient Perovskite Solar Cells, *ACS Energy Lett.* **2020**, 5, 2742–2786.

[71] Z. Tan, R. S. Moghaddam, M. L. Lai, P. Docampo, R. Higler, F. Deschler, M. Price, A. Sadhanala, L. M. Pazos, D. Credgington, F. Hanusch, T. Bein, H. J. Snaith, R. H. Friend, Bright Light-Emitting Diodes Based on Organometal Halide Perovskite, *Nat. Nanotechnol.* **2014**, 9, 687–692.

[72] X. K. Liu, W. Xu, S. Bai, Y. Jin, J. Wang, R. H. Friend, F. Gao, Metal Halide Perovskites for Light-Emitting Diodes, *Nat. Mater.* **2021**, 20, 10–21.

[73] S. D. Stranks, R. L. Z. Hoye, D. Di, R. H. Friend, F. Deschler, The Physics of Light Emission in Halide Perovskite Devices, *Adv. Mater.* **2019**, 31, DOI 10.1002/adma.201803336.

[74] C. Qin, A. S. D. Sandanayaka, C. Zhao, T. Matsushima, D. Zhang, T. Fujihara, C. Adachi, Stable Room-Temperature Continuous-Wave Lasing in Quasi-2D Perovskite Films, *Nature* **2020**, 585, 53–57.

[75] Q. Dong, L. Lei, J. Mendes, F. So, Operational Stability of Perovskite Light Emitting Diodes, *J. Phys. Mater.* **2020**, 3, 012002.

[76] M. R. Leyden, S. Terakawa, T. Matsushima, S. Ruan, K. Goushi, M. Auffray, A. S. D. D. Sandanayaka, C. Qin, F. Bencheikh, C. Adachi, Distributed Feedback Lasers and Light-Emitting Diodes Using 1-Naphthylmethylamnonium Low-Dimensional Perovskite, *ACS Photonics* **2019**, 6, 460–466.

[77] M. Saliba, S. M. Wood, J. B. Patel, P. K. Nayak, J. Huang, J. A. Alexander-Webber, B. Wenger, S. D. Stranks, M. T. Hörantner, J. T. Wang, R. J. Nicholas, L. M. Herz, M. B. Johnston, S. M. Morris, H. J. Snaith, M. K. Riede, Structured Organic-Inorganic Perovskite toward a Distributed Feedback Laser, *Adv. Mater.* **2016**, 28, 923–929.

[78] N. Pourdavoud, T. Haeger, A. Mayer, P. J. J. Cegielski, A. L. L. Giesecke, R. Heiderhoff, S. Olthof, S. Zaefferer, I. Shutsko, A. Henkel, D. Becker-Koch, M. Stein, M. Cehovski, O. Charfi, H. H. Johannes, D. Rogalla, M. C. C. Lemme, M. Koch, Y. Vaynzof, K. Meerholz, W. Kowalsky, H. C. Scheer, P. Görrn, T. Riedl, Room-Temperature Stimulated Emission and Lasing in Recrystallized Cesium Lead Bromide Perovskite Thin Films, *Adv. Mater.* **2019**, 31, 1903717.

CHAPTER 2: INTERFACIAL PASSIVATION IN PEROVSKITE PVS

This chapter has been previously published in:

Q. Dong, C. H. Y. Ho, H. Yu, A. Salehi, F. So, Defect Passivation by Fullerene Derivative in Perovskite Solar Cells with Aluminum-Doped Zinc Oxide as Electron Transporting Layer, *Chem. Mater*. **2019**, 31, 6833–6840.

2.1 Abstract

ZnO is a potential replacement for TiO_2 as an electron transport layer (ETL) used in low-temperature processed hybrid perovskite solar cells. However, poor thermal stability of perovskites on ZnO and interfacial traps introduced during processing are obstacles to achieve a good device performance. In this Chapter, we demonstrate perovskite solar cells using aluminum doped zinc oxide (AZO) nanoparticles for the ETL having a better thermal stability compared with ZnO. However, the device shows a lower short circuit current density and a large photocurrent hysteresis, which are attributed to the poor interfacial properties between the ETL and the perovskite layer. To address this issue, a thin interfacial modification layer of phenyl-C61-butyric acid methyl ester (PCBM) is employed. The resulting device show the efficiency is improved from 13% to 17% along with a significant reduction in hysteresis. Results from our thermal admittance spectroscopy show that the interface defect states are significantly reduced with the PCBM passivation layer.

2.2 Introduction

Metal-halide perovskite solar cell is considered as a promising candidate for photovoltaics in recent years. The power conversion efficiency (PCE) has been improved from 3.8% to over 25% in one decade.[1,2] Different approaches have been employed to enhance the device performance, and they include morphological control,[3–6] chemical composition engineering,[7,8] interfacial modification,[9] and defect passivation of the active layer.[10,11] Today, pinhole-free perovskite films with a grain size larger than 300 nm can be obtained by non-polar solvent washing during the spin coating process.[3,4] In addition, solvent vapor assisted annealing can increase the grain size of the perovskite film, leading to improved crystallinity and device performance.[6] Compared to the study on the morphology and crystallinity of the active layer, in-depth study on electron transporting layer (ETL) in perovskite solar cells is still lacking. Today, titanium oxide (TiO_2) is the most used ETL for high efficiency perovskite solar cells.[1,3–5] However, the high processing temperature of TiO_2, which is usually above 450 ℃, presents a problem to fabricate perovskite cells on flexible substrates. To overcome this limitation, zinc oxide (ZnO) has been used as an alternative candidate, owing to its good optical transparency in the visible spectrum, high electron mobility, low processing temperature, and energy level matching with perovskites.[12,13] However, the thermal instability of perovskite films deposited directly on ZnO is an obstacle to achieve good efficiencies.[14,15] It is known that perovskite films on ZnO tend to decompose when the post-annealing temperature is above 70 ℃.[14] Lowering the annealing temperature will lead to incomplete crystallization and poor morphology.[12,14] Further, under operation conditions, photovoltaic devices are inevitably heated up due to illumination of sunlight, leading to an accelerated degradation of the perovskite film.[16] As a result, both the efficiency and the stability of perovskite solar cells using ZnO as an ETL are inferior to the devices using TiO_2.

To address the thermal instability issue of the perovskites caused by the underlying ZnO film, two approaches have been reported. One approach is to avoid the direct contact between ZnO and perovskite by inserting a passivation interlayer between the ETL and the perovskite film,[14] while another approach is to dope a small amount of aluminum (1~3 wt%) into ZnO to change its surface properties.[17–20] To passivate ZnO films, the most common passivation layers are polyethylenimine (PEI) and phenyl-C61-butyric acid methyl ester (PCBM). However, it was found that a passivation layer is insufficient to completely suppress the decomposition of perovskite on ZnO.[14] Alternatively, aluminum zinc oxide (AZO) is a potential candidate as an ETL for low temperature processed perovskite cells. To fabricate AZO films, various methods have been used. Mahmud *et al.* doped Al into sol gel ZnO, resulting in a more stable device and an enhanced efficiency from 12% to 14%.[19] Li *et al*. and Zhao *et al*. employed sputtered AZO as the bottom cathode in perovskite solar cells, with the best efficiency only around 13% having a large hysteresis effect due to a large amount charge traps at the AZO/perovskite interface.[17,18] Although using AZO as an ETL can address the issue of thermal instability of perovskite, the device efficiency is inferior due to the defects at AZO and perovskite interface. As discussed above, phenyl-C61-butyric acid methyl ester (PCBM) has been used as a passivation layer for ZnO [14] as well as for perovskite films.[10,14] Here, we attempt to use PCBM as a passivation layer for the perovskite solar cells and study its passivation properties on perovskite solar cells having AZO as an ETL.

In this work, we fabricated conventional perovskite solar cells using AZO nanoparticles as the ETL with and without a PCBM passivation layer. Without the PCBM interlayer, the average device efficiency is about 13%, which is comparable to the values from the literature.[17–20] By adding PCBM as a passivation layer, the average efficiency has been improved to 17%. In addition to the efficiency enhancement, the hysteresis effect is significantly reduced. To investigate the efficiency enhancement mechanism, both photoluminescence and thermal admittance spectroscopy (TAS) measurements were conducted to probe the interfacial properties including electron extraction efficiency and interfacial charge traps. We found that PCBM not only facilitates electron extraction from perovskite to ETLs, but also passivates the interfacial charge traps, resulting in a much better device performance.

2.3 Thin film characterizations

AZO nanoparticle (3.15 mol% Al) films were fabricated by spin coating of commercially purchased nanoparticle ink on ITO patterned glass substrates. The optical properties of AZO nanoparticle film are shown in **Figure 2.1a**. The absorbance was measured by ellipsometry, and we estimate the film thickness is 40 nm based on the transmittance and the SEM data. Through the Tauc plot, the direct optical band gap is determined to be 3.25 eV, which is consistent with the value reported in the literature.[21] The transmission data show that the AZO film has a high transparency of 95% in the visible spectrum. **Figure 2.1b** shows the SEM micrograph of the AZO nanoparticle film having an average grain size of around 10 nm. The thermal stability of perovskite on the AZO film was investigated by XRD as shown in **Figure 2.1c**. The relative intensity of the peak corresponding to PbI_2 and the full width at half maximum (FWHM) of the perovskite (110) peak gives information on the crystallinity and the possible decomposition of perovskite. Here perovskites films were fabricated by one-step spin coating method with a subsequent annealing step at 100 ℃ for 10 min to complete the crystallization process. It is known that perovskite films on ZnO can easily be decomposed at high annealing temperatures due to residual hydroxide groups on the surface of ZnO.[14,15] Based on our XRD results, the very low intensity of PbI_2 peak on AZO is similar with that on glass substrate, indicating that there is no decomposition of perovskite on AZO during processing. In addition, the FWHMs of the perovskite (110) peak in the two samples are almost the same, indicating that AZO does not impede the crystallization of perovskite. As a result, a pin hole-free perovskite device-quality film with a grain size of 300 nm can be fabricated on AZO as shown in **Figure 2.1d**.

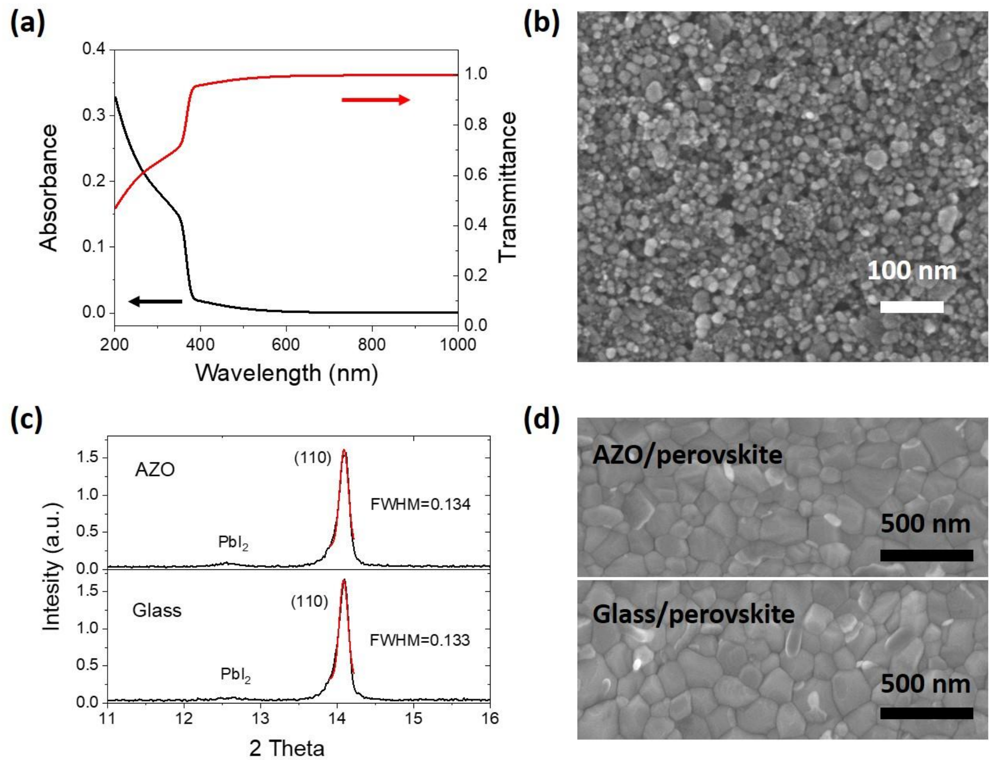

Figure 2.1 (a) UV-visible absorption and transmittance of AZO film. (b) SEM image of AZO nanoparticle film. (c) XRD of perovskites on different substrates. (d) Top view SEM of perovskites on different substrates.

2.4 Device performance

In this work, a conventional device architecture of ITO/AZO/PCBM/Perovskite/2,2',7,7'-Tetrakis-(N, N-di-4-methoxyphenylamino)-9,9'-spirobifluorene (spiro-MeOTAD) /MoO_x/Al was adopted as shown in **Figure 2.2**. PCBM functions as an interfacial modification layer, while spiro-MeOTAD serves as a hole transporting layer. It is known that DMF solvent used in the perovskite precursors can dissolve PCBM during solution processing. However, we found that having an AZO bottom layer in the stack, depositing the perovskite layer on top of PCBM does not wash away PCBM. Consequently, PCBM still remains after the deposition of perovskites and avoid the direct contact between perovskite and the underlying AZO layer, which is clearly observed in the device cross-section SEM in **Figure 2.3a&b**. Based on the morphology results shown by SEM in **Figure 2.3d**, the morphology of perovskite is not affected by the PCBM interlayer. In addition, the XRD data in **Figure 2.3c** also show similar crystallization characteristics of the perovskite films with or without the PCBM interlayer. Therefore, the insertion of the PCBM interlayer can affect the interfacial properties of the perovskite at the bottom, but not the upper part of the perovskite film.

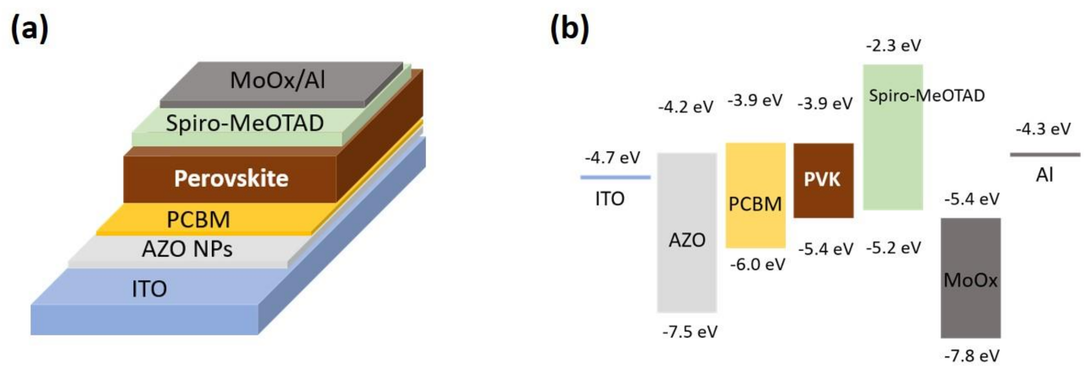

Figure 2.2 (a) Device structure of perovskite solar cells. (b) Energy diagram.

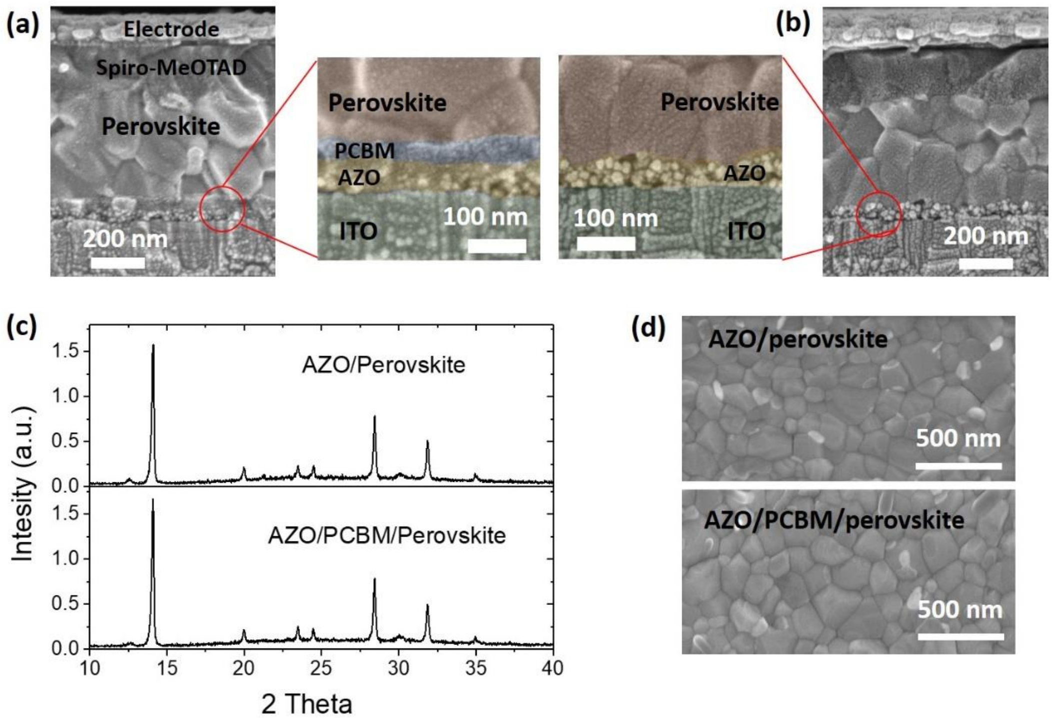

Figure 2.3 (a) & (b) Cross-section SEM images of perovskite solar cells, (a) Device with PCBM, (b) Device without PCBM. (c) XRD of perovskite films on different ETLs. (d) SEM morphology of perovskites on AZO and AZO/PCBM.

To compare the device performance between the two devices, the device data with and without the PCBM interlayer are shown in **Figure 2.4** and a summary is given in **Table 2.1**. Without the PCBM interlayer, while both open circuit voltage (V_{oc}) and fill factor (FF) are comparable to the perovskite solar cells having an AZO layer reported in the literature,[17–20] a strong photocurrent hysteresis is observed in the device without PCBM interlayer,[10] as shown in **Figure 2.4c**. When the PCBM interlayer is used, the device performance is significantly improved, due to an increase in J_{sc} from 16.3 to 20.1 mA/cm^2 and fill factor from 0.71 to 0.78. As a result, the average PCE is increased to around 17%. In addition, photocurrent hysteresis effect has also been largely reduced as shown **Figure 2.4d**. As discussed above, the bulk properties of perovskites are not altered by adding the PCBM interlayer, suggesting that the enhancement is due to the changes at the ETLs/perovskite interface. Among the PV device parameters, only V_{oc} is not changed by adding the PCBM interlayer, indicating that the energy level alignment should not be a reason for the improved device performance. The increase in J_{sc} should not be due to the change in light absorption, considering that the thickness and the bulk properties of perovskite with and without PCBM are same. This can also be supported by EQE data shown in **Figure 2.4b** where we found there are no changes in the shape of the EQE spectrum and an increase in EQE overall all wavelengths due to the presence of the PCBM interlayer. Hence, we attribute the increase in J_{sc} to the improved electron extraction and charge collection facilitated by the PCBM interlayer. In the absence of PCBM, we speculate that due to the ineffective electron extraction, electrons accumulate at the AZO/perovskite interface give rise to charge carrier recombination, resulting in a lower fill factor. The improvement in fill factor might also be partially attributed to the enhanced electron extraction and defect passivation facilitated by the PCBM interlayer.

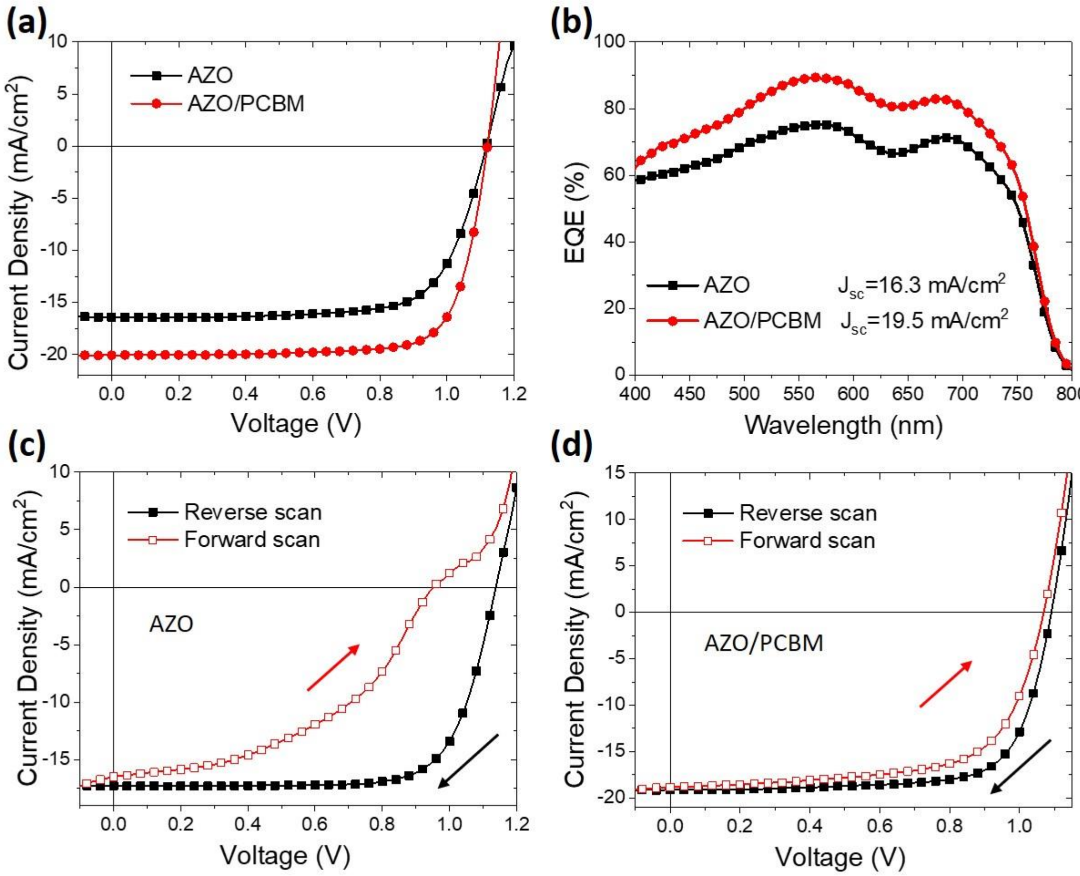

Figure 2.4 (a) J-V curves and (b) EQE spectrum of perovskite solar cells with and without PCBM interlayer. The integrated short circuit currents are shown for both cases. (c) and (d) J-V curves obtained from forward and reverse scan directions.

Table 2.1 Device performance of perovskite solar cells (average of 16 devices).

	J_{sc} (mA/cm^2)	V_{oc} (V)	FF	PCE (%)
AZO	16.3 ± 1.0	1.12 ± 0.02	0.71 ± 0.04	12.9 ± 0.8
AZO/PCBM	20.1 ± 0.4	1.12 ± 0.02	0.75 ± 0.02	16.9 ± 0.7

To confirm the function of PCBM on facilitating electron extraction, spectral photoluminescence (PL) measurements were conducted on the perovskite films. Three thin film samples were prepared on glass substrates including AZO/perovskite, AZO/PCBM/perovskite and perovskite/spiro-MeOTAD. The relative photoluminescence intensity indicates the quenching effect at the interface of perovskite with either the ETL or HTL due to the carrier transfer across the interface.[22] Therefore, the change in the photoluminescence intensity of perovskites on AZO or AZO/PCBM can be correlated with the electron extraction efficiency from perovskite to ETLs. To exclude the light scattering and absorption by Spiro-MeOTAD and AZO/PCBM, the PL signal of perovskite/Spiro-MeOTAD was measured from the backside of the glass substrate, while the PL signal of AZO/PCBM/perovskite was measured from the top of the perovskite films. The light scattering and absorption by glass in the case of perovskite/Spiro-MeOTAD can be neglected. **Figure 2.5** shows that PL quenching in the perovskite film is the strongest with Spiro-MeOTAD and is the weakest with AZO, indicating the hole extraction efficiency from perovskite to HTLs is stronger than the electron extraction to the AZO layer. The resulting unbalanced electron and hole extraction efficiency might be one of the reasons for charge accumulation at the AZO/perovskite interface, resulting in carrier recombination, a lower fill factor and poor device performance. When the PCBM interlayer is added, PL quenching is significantly increased to a value closer to the perovskite with spiro-MeOTAD, indicating that PCBM interlayer can facilitate electron extraction, resulting in a more balanced electron and hole extraction efficiency. The improved device performance with the PCBM interlayer can be partially attributed to the reduced electron accumulation at ETLs/perovskite interface, which is important for achieving low recombination rate and high fill factor.

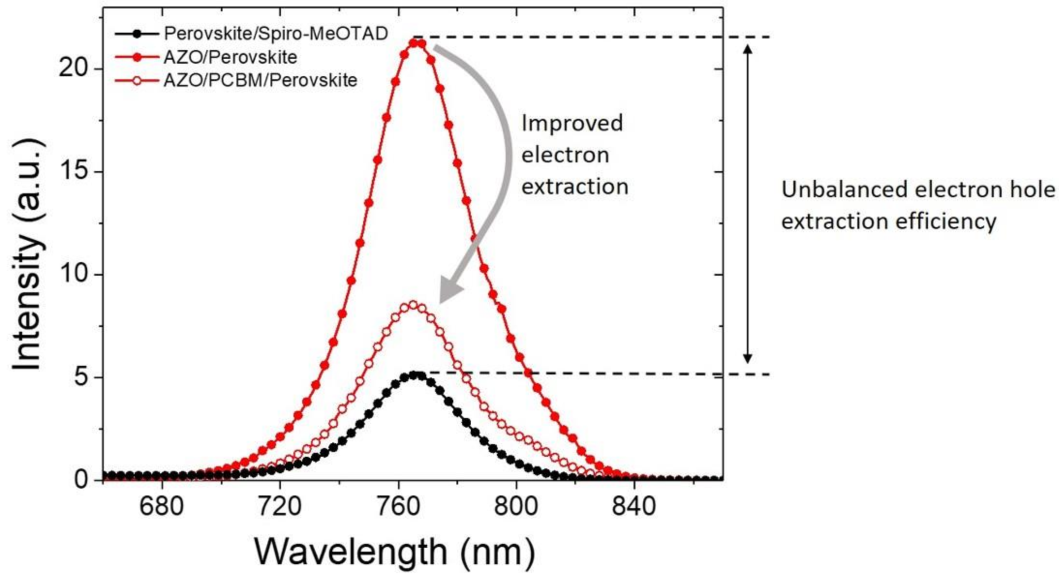

Figure 2.5 Photoluminescence of perovskite films combined with different layers.

2.5 Thermal admittance spectroscopy

In addition to the improvement in the PV device due to the use of the PCBM interlayer, we have observed a strong suppression of hysteresis in the solar cell with PCBM. In the literature, several mechanisms have been proposed to explain the hysteresis phenomenon in perovskite solar cells,[23] including capacitance effect,[24] ferroelectric effect,[25] charge trapping,[10,26] and ion migration.[27] As mentioned above, the addition of the PCBM interlayer does not affect the bulk properties of the perovskite film. The reduction in hysteresis in the device with PCBM can be attributed to a reduction of defects at the ETL/perovskite interface. Therefore, we conjecture that the PCBM interlayer acts as an interfacial passivation layer suppressing the photocurrent hysteresis. The charge traps are defect states introduced either during the processing of the perovskite layer or on the AZO film surface. The hysteresis induced by interfacial charge traps can be explained by a slow dynamic process of trap charging and discharging. When the applied external bias starts from the short circuit condition to the open circuit condition, the interfacial traps are partially filled by charge carriers, resulting in charge accumulation at the interface impeding the extraction of charge carriers out of the perovskite layer. Under reverse scan conditions, the traps are filled in the beginning under large forward bias such that charge carriers can be more efficiently extracted from perovskite.[10,23,26] This is probably the reason why the photocurrent obtained from the reverse scan direction is larger than that from the forward scan direction.

Here, we characterize the interfacial charge traps by thermal admittance spectroscopy (TAS), which is a characterization technique used for probing the electronic defect profile within the bandgap in semiconductors.[28–30] In TAS measurements, the complex admittance of a device is measured versus the probing frequency and temperature. The complex admittance can be represented by conductance (G) and capacitance (C):

$$Y = G(\omega, T) + i\omega C(\omega, T) \qquad (2.1)$$

where $\omega = 2\pi f$ is the angular frequency of the probing ac-signal, and T is the temperature. The existence of defects is revealed by a decrease of the measured capacitance obtained from low frequency to high frequency. The contribution to capacitance by defects is realized by charging and discharging of traps under the ac-signal. At low frequencies, the dynamic process of charging and discharging of most traps follows the change of alternating electric field, contributing to the measured capacitance. When the frequency is increased, some defects cannot respond to the ac-excitation, thus not contributing to the capacitance, resulting in a decrease in the capacitance. If we consider a single defect, the dependence of the capacitance on frequency can be represented by a combination of depletion capacitance and the capacitance from the trapped charges[31]

$$C(\omega) = C_{depletion} + \frac{1}{1+\omega^2\tau^2} C_{trap} \qquad (2.2)$$

where τ is the time constant of charging and discharging process, which can be extracted from the measured capacitance-frequency (C-f) curve. From the equation, we observe that there is a clear step in the C-f curve, and the characteristic transition frequency $\omega_t = 1/\tau$ is where the step occurs. The energy of the defect is reflected by a shift of the step when the temperature changes, since the dynamic process of charging and discharging is related to the thermal energy by:[28]

$$\omega_t = \beta T^2 \exp\left(\frac{-E_a}{kT}\right) \qquad (2.3)$$

where β is a constant, k is the Boltzmann constant and E_a is the activation energy of the defect. The activation energy is the energy of the defect level above valence band for hole trap or below conduction band for electron trap.

2.6 Quantifying interfacial defects

Figure 2.6 shows the capacitance-frequency curves of the devices with and without the PCBM passivation layer at different temperatures. The temperature ranges from 220 K to 290 K with a temperature step of 10 K. It has been reported that there are phase changes in $MAPbI_3$ at 160 K and 330 K.[32] Since these transition temperatures are outside the temperature range at our TAS measurements, phase changes should not be considered here. At 290 K, the low frequency capacitance of the device without the PCBM passivation layer is already much larger than that with the PCBM passivation layer, indicating a higher charge trap density in the former case. When the temperature decreases, for both cases, the step in the C-f curves shifts from high frequency to low frequency, consistent with Equation (2.3). To gain a more quantitative understanding on the change of defects profile due to passivation by PCBM, we firstly extract the characteristic transition frequency through a plot of $(-\omega \cdot \frac{dC}{d\omega})$ versus ω, where the transition frequency is at its maximum. Then we rewrite Equation (2.3) as:

$$\ln\left(\frac{\omega_t}{T^2}\right) = -\frac{E_a}{k}\frac{1}{T} + \ln(\beta) \qquad (2.4)$$

The activation energy can be extracted through linear regression according to Equation (2.4) as shown in **Figure 2.7**. The slope of the fitted line represents the activation energy of the defects. We found that the activation energy is reduced from 490 meV to 350 meV with the PCBM passivation. It should be noted that there is a distribution of defects in the device instead of just a single defect, and the activation energy extracted here is the median value. The reduction on defects energy indicates the deep traps become shallower due to the presence of the PCBM layer.

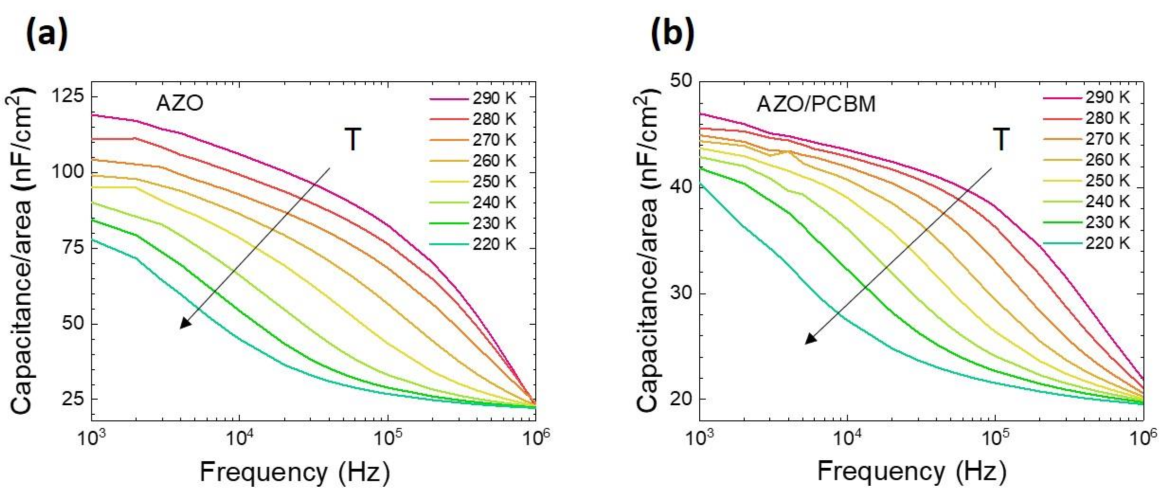

Figure 2.6 Capacitance-frequency curves at different temperature. (a) Device without PCBM interlayer. (b) Device with PCBM interlayer.

Based on the extracted activation energy, the charge trap density can be quantitatively obtained from the measured C-F curves through the following equation:[28]

$$N_t(E_\omega) = -\frac{V_{bi}}{eW}\frac{dC}{d\omega}\frac{\omega}{kT} \qquad (2.5),$$

where N_t is the trap density V_{bi} is the built-in potential, e is the elementary charge, W is the depletion width, and E_ω is the defect energy. The built-in potential of perovskite solar cells reported in the literature is generally 1.0 V,[33] which is also consistent with the V_{oc} our devices. Therefore, 1.0 V was used as the built-in potential in Equation (2.5). The energy distribution of charge trap density is plotted in **Figure 2.8**. Without the PCBM passivation layer, the peak value of trap density is around $2.1 \times 10^{17}\ cm^{-3}eV^{-1}$, while with the PCBM passivation layer, the peak value is reduced to $7.5 \times 10^{16}\ cm^{-3}eV^{-1}$. By integrating the traps over energy, the total trap densities of devices with and without PCBM passivation are $5.9 \times 10^{15}\ cm^{-3}$ and $1.8 \times 10^{16}\ cm^{-3}$ respectively, indicating there is a three-time reduction of the trap density. Compared to the shifting of trap energy from 490 meV to 350 mV, the reduction in trap density is more pronounced. Therefore, it is the reduced charge trap density that mainly accounts for the reduction in the hysteresis effect shown by the perovskite solar cells. From the TAS data, we verify that the passivation effect of PCBM resulting in reduced hysteresis and enhancement in the photovoltaic device performance.

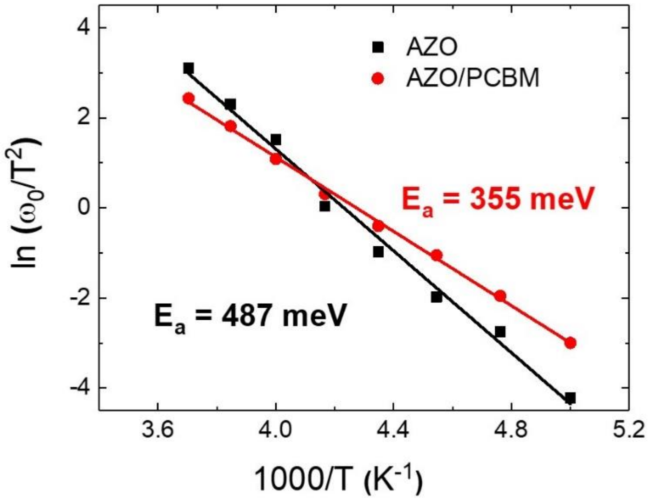

Figure 2.7 Linear fitting of characteristic frequency versus temperature.

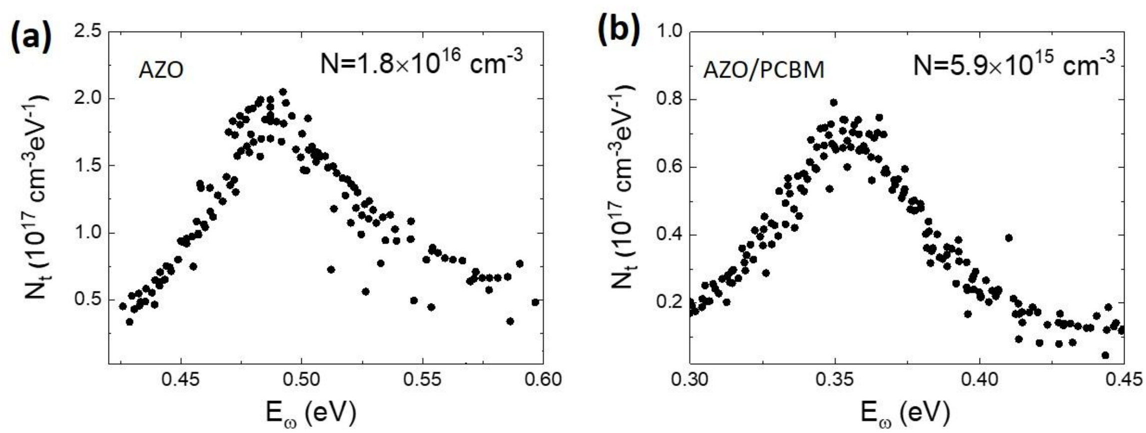

Figure 2.8 Charge trap density distribution over energy. (a) Device without PCBM interlayer. (b) Device with PCBM interlayer.

2.7 Conclusion

In this Chapter, we demonstrated that perovskite films on AZO nanoparticles show good thermal stability. The device performance can be improved by inserting a PCBM interlayer between the AZO and perovskite layers. Since PCBM does not affect the bulk properties of the perovskite film, the enhanced power conversion efficiency of the resulting solar cell is attributed to the passivation on the ETLs/perovskite interfacial properties. The increase in photocurrent and fill factor can be attributed to improved electron extraction facilitated by PCBM, while the reduction in hysteresis can be attributed to the defect passivation of the interfacial traps by PCBM. The passivation effect of PCBM not only shifts the defect activation energy to a lower value, but also reduces the total trap density by three times from $1.8 \times 10^{16}\ cm^{-3}$ to $5.9 \times 10^{15}\ cm^{-3}$. We demonstrated that PCBM functions as an effective interfacial defect passivation material in perovskite solar cells having an AZO ETL.

2.8 Methods

Materials

Aluminum-doped zinc oxide (2.5 wt.%) nanoparticle ink, lead iodide (99.999%), dimethylformamide (99.9%) and chlorobenzene (99.9%) are purchased from Sigma Aldrich. Dimethyl sulfoxide is from Fisher Chemical. PCBM is from Nano-C. Methylammonium iodide is from Dyesol. 2,2',7,7'-Tetrakis-(N, N-di-4-methoxyphenylamino)-9,9'-spirobifluorene (Spiro-MeOTAD) is from Xi'an Polymer Light Technology Corp. D.

Device Fabrication

ITO patterned glass substrates are cleaned by isopropanol and acetone in ultrasonic bath in sequence. The substrates are subjected to UV-Ozone for 15 min before using. All the solution-processed films are deposited in nitrogen-filled glove box. AZO nanoparticle ink is spin coated on the substrates at a speed of 3000 rpm, followed by annealing at 150 ℃ for 10 min. For devices with PCBM interlayer, precursor solution with a concentration of 20 mg/mL PCBM in CB is spin coated on AZO film at 4500 rpm. Then the samples are annealed at 80 ℃ for 10 min to evaporate residual CB solvent. Perovskite films are fabricated by one-step method reported in the literature.[3] Perovskite precursor solution is prepared by dissolving PbI_2, MAI and DMSO (molar ratio is 1: 1:

1) in DMF with a concentration of 1 M. The precursor solution is spin coated on ETLs, during which 100 uL of toluene is dropped on the sample at 8th second. The precursor film is then annealed at 100 ℃ for 10 min to complete the crystallization. After that, hole transporting layer (Spiro-MeOTAD) is deposited on perovskite. Finally, 15 nm of MoO_x and 100 nm of Aluminum are deposited on HTL as electrode.

Characterizations

J-V curves are measured by Keithley 2400 under illumination of AM 1.5 generated by solar simulator. SEM images are taken by FEI Verios 460L field-emission scanning electron microscope, and XRD measurements are conducted by Rigaku SmartLab X-Ray Diffractometer. Photoluminescence is measured by FLS920 Fluorescence Spectrometer from Edinburgh Instruments. Optical Absorption and transmission were measured by ellipsometer (ESM300) from J. A. Woollam. For the thermal admittance spectroscopy (TAS) measurements, an AC signal of 20 mV is applied on perovskite solar cells to probe the capacitance at different frequencies. During the measurement, the samples are put in vacuum with temperature controlled by heater and liquid nitrogen.

REFERENCES

[1] A. Kojima, K. Teshima, Y. Shirai, T. Miyasaka, Organometal Halide Perovskites as Visible-Light Sensitizers for Photovoltaic Cells, *J. Am. Chem. Soc.* **2009**, 131, 6050–6051.

[2] J. J. Yoo, G. Seo, M. R. Chua, T. G. Park, Y. Lu, F. Rotermund, Y. K. Kim, C. S. Moon, N. J. Jeon, J. P. Correa-Baena, V. Bulović, S. S. Shin, M. G. Bawendi, J. Seo, Efficient Perovskite Solar Cells via Improved Carrier Management, *Nature* **2021**, 590, 587–593.

[3] N. J. Jeon, J. H. Noh, Y. C. Kim, W. S. Yang, S. Ryu, S. Il Seok, Solvent Engineering for High-Performance Inorganic-Organic Hybrid Perovskite Solar Cells, *Nat. Mater.* **2014**, 13, 897–903.

[4] M. Xiao, F. Huang, W. Huang, Y. Dkhissi, Y. Zhu, J. Etheridge, A. Gray-Weale, U. Bach, Y.-B. Cheng, L. Spiccia, A Fast Deposition-Crystallization Procedure for Highly Efficient Lead Iodide Perovskite Thin-Film Solar Cells, *Angew. Chemie* **2014**, 126, 10056–10061.

[5] J. Burschka, N. Pellet, S. J. Moon, R. Humphry-Baker, P. Gao, M. K. Nazeeruddin, M. Grätzel, Sequential Deposition as a Route to High-Performance Perovskite-Sensitized Solar Cells, *Nature* **2013**, 499, 316–319.

[6] Z. Xiao, Q. Dong, C. Bi, Y. Shao, Y. Yuan, J. Huang, Solvent Annealing of Perovskite-Induced Crystal Growth for Photovoltaic-Device Efficiency Enhancement, *Adv. Mater.* **2014**, 26, 6503–6509.

[7] S. Colella, E. Mosconi, P. Fedeli, A. Listorti, F. Gazza, F. Orlandi, P. Ferro, T. Besagni, A. Rizzo, G. Calestani, G. Gigli, F. De Angelis, R. Mosca, MAPbI3-XClx Mixed Halide Perovskite for Hybrid Solar Cells: The Role of Chloride as Dopant on the Transport and Structural Properties, *Chem. Mater.* **2013**, 25, 4613–4618.

[8] N. J. Jeon, J. H. Noh, W. S. Yang, Y. C. Kim, S. Ryu, J. Seo, S. Il Seok, Compositional Engineering of Perovskite Materials for High-Performance Solar Cells, *Nature* **2015**, 517, 476–480.

[9] H. Zhou, Q. Chen, G. Li, S. Luo, T. -b. Song, H.-S. Duan, Z. Hong, J. You, Y. Liu, Y. Yang,

Interface Engineering of Highly Efficient Perovskite Solar Cells, *Science (80-.)*. **2014**, 345, 542–546.

[10] Y. Shao, Z. Xiao, C. Bi, Y. Yuan, J. Huang, Origin and Elimination of Photocurrent Hysteresis by Fullerene Passivation in CH3NH3PbI3 Planar Heterojunction Solar Cells, *Nat. Commun.* **2014**, 5, 1–7.

[11] X. Zheng, B. Chen, J. Dai, Y. Fang, Y. Bai, Y. Lin, H. Wei, X. C. Zeng, J. Huang, Defect Passivation in Hybrid Perovskite Solar Cells Using Quaternary Ammonium Halide Anions and Cations, *Nat. Energy* **2017**, 2, 1–9.

[12] D. Liu, T. L. Kelly, Perovskite Solar Cells with a Planar Heterojunction Structure Prepared Using Room-Temperature Solution Processing Techniques, *Nat. Photonics* **2014**, 8, 133–138.

[13] J. Song, W. Hu, X. F. Wang, G. Chen, W. Tian, T. Miyasaka, HC(NH2)2PbI3 as a Thermally Stable Absorber for Efficient ZnO-Based Perovskite Solar Cells, *J. Mater. Chem. A* **2016**, 4, 8435–8443.

[14] Y. Cheng, Q. D. Yang, J. Xiao, Q. Xue, H. W. Li, Z. Guan, H. L. Yip, S. W. Tsang, Decomposition of Organometal Halide Perovskite Films on Zinc Oxide Nanoparticles, *ACS Appl. Mater. Interfaces* **2015**, 7, 19986–19993.

[15] J. Yang, B. D. Siempelkamp, E. Mosconi, F. De Angelis, T. L. Kelly, Origin of the Thermal Instability in CH3NH3PbI3 Thin Films Deposited on ZnO, *Chem. Mater.* **2015**, 27, 4229–4236.

[16] Q. Dong, F. Liu, M. K. Wong, H. W. Tam, A. B. Djurišić, A. Ng, C. Surya, W. K. Chan, A. M. C. Ng, Encapsulation of Perovskite Solar Cells for High Humidity Conditions, *ChemSusChem* **2016**, 9, 2597–2603.

[17] X. Li, W. Ye, X. Zhou, F. Huang, D. Zhong, Increased Efficiency for Perovskite Photovoltaics Based on Aluminum-Doped Zinc Oxide Transparent Electrodes via Surface Modification, *J. Phys. Chem. C* **2017**, 121, 10282–10288.

[18] X. Zhao, H. Shen, Y. Zhang, X. Li, X. Zhao, M. Tai, J. Li, J. Li, X. Li, H. Lin, Aluminum-Doped Zinc Oxide as Highly Stable Electron Collection Layer for Perovskite Solar Cells, *ACS Appl. Mater. Interfaces* **2016**, 8, 7826–7833.

[19] M. A. Mahmud, N. K. Elumalai, M. B. Upama, D. Wang, M. Wright, T. Sun, C. Xu, F. Haque, A. Uddin, Simultaneous Enhancement in Stability and Efficiency of Low-Temperature Processed Perovskite Solar Cells, *RSC Adv.* **2016**, 6, 86108–86125.

[20] J. Dong, Y. Zhao, J. Shi, H. Wei, J. Xiao, X. Xu, J. Luo, J. Xu, D. Li, Y. Luo, Q. Meng, Impressive Enhancement in the Cell Performance of ZnO Nanorod-Based Perovskite Solar Cells with Al-Doped ZnO Interfacial Modification, *Chem. Commun.* **2014**, 50, 13381–13384.

[21] S. Zellmer, A. Kockmann, I. Dosch, B. Temel, G. Garnweitner, Aluminum Zinc Oxide Nanostructures with Customized Size and Shape by Non-Aqueous Synthesis, *CrystEngComm* **2015**, 17, 6878–6883.

[22] C. Liu, K. Wang, P. Du, T. Meng, X. Yu, S. Z. D. Cheng, X. Gong, High Performance Planar Heterojunction Perovskite Solar Cells with Fullerene Derivatives as the Electron Transport Layer, *ACS Appl. Mater. Interfaces* **2015**, 7, 1153–1159.

[23] B. Chen, M. Yang, S. Priya, K. Zhu, Origin of J-V Hysteresis in Perovskite Solar Cells, *J. Phys. Chem. Lett.* **2016**, 7, 905–917.

[24] O. Almora, I. Zarazua, E. Mas-Marza, I. Mora-Sero, J. Bisquert, G. Garcia-Belmonte, Capacitive Dark Currents, Hysteresis, and Electrode Polarization in Lead Halide Perovskite Solar Cells, *J. Phys. Chem. Lett.* **2015**, 6, 1645–1652.

[25] J. Wei, Y. Zhao, H. Li, G. Li, J. Pan, D. Xu, Q. Zhao, D. Yu, Hysteresis Analysis Based on the Ferroelectric Effect in Hybrid Perovskite Solar Cells, *J. Phys. Chem. Lett.* **2014**, 5, 3937–3945.

[26] K. Wojciechowski, S. D. Stranks, A. Abate, G. Sadoughi, A. Sadhanala, N. Kopidakis, G. Rumbles, C. Z. Li, R. H. Friend, A. K. Y. Jen, H. J. Snaith, Heterojunction Modification for Highly Efficient Organic-Inorganic Perovskite Solar Cells, *ACS Nano* **2014**, 8, 12701–

12709.

[27] W. Tress, N. Marinova, T. Moehl, S. M. Zakeeruddin, M. K. Nazeeruddin, M. Grätzel, Understanding the Rate-Dependent J-V Hysteresis, Slow Time Component, and Aging in CH3NH3PbI3 Perovskite Solar Cells: The Role of a Compensated Electric Field, *Energy Environ. Sci.* **2015**, 8, 995–1004.

[28] T. Walter, R. Herberholz, C. Müller, H. W. Schock, Determination of Defect Distributions from Admittance Measurements and Application to Cu(In,Ga)Se2 Based Heterojunctions, *J. Appl. Phys.* **1996**, 80, 4411–4420.

[29] S. Khelifi, K. Decock, J. Lauwaert, H. Vrielinck, D. Spoltore, F. Piersimoni, J. Manca, A. Belghachi, M. Burgelman, Investigation of Defects by Admittance Spectroscopy Measurements in Poly (3-Hexylthiophene):(6,6)-Phenyl C61-Butyric Acid Methyl Ester Organic Solar Cells Degraded under Air Exposure, *J. Appl. Phys.* **2011**, 110, DOI 10.1063/1.3658023.

[30] H. S. Duan, H. Zhou, Q. Chen, P. Sun, S. Luo, T. Bin Song, B. Bob, Y. Yang, The Identification and Characterization of Defect States in Hybrid Organic-Inorganic Perovskite Photovoltaics, *Phys. Chem. Chem. Phys.* **2015**, 17, 112–116.

[31] Y. Zohta, Frequency Dependence of C and ΔV/Δ(C-2) of Schottky Barriers Containing Deep Impurities, *Solid State Electron.* **1973**, 16, 1029–1035.

[32] C. Quarti, E. Mosconi, J. M. Ball, V. D'Innocenzo, C. Tao, S. Pathak, H. J. Snaith, A. Petrozza, F. De Angelis, Structural and Optical Properties of Methylammonium Lead Iodide across the Tetragonal to Cubic Phase Transition: Implications for Perovskite Solar Cells, *Energy Environ. Sci.* **2016**, 9, 155–163.

[33] O. Almora, C. Aranda, E. Mas-Marzá, G. Garcia-Belmonte, On Mott-Schottky Analysis Interpretation of Capacitance Measurements in Organometal Perovskite Solar Cells, *Appl. Phys. Lett.* **2016**, 109, DOI 10.1063/1.4966127.

CHAPTER 3: THE IMPACT OF ION MIGRATION IN PEROVSKITE LEDS

This chapter has been previously published in:

Q. Dong, J. Mendes, L. Lei, D. Seyitliyev, L. Zhu, S. He, K. Gundogdu, F. So, Understanding the Role of Ion Migration in the Operation of Perovskite Light-Emitting Diodes by Transient Measurements, *ACS Appl. Mater. Interfaces* **2020**, 12, 48845–48853.

3.1 Abstract

Perovskite light emitting diodes (LEDs) have been gaining attention in recent years due to the high efficiencies. Despite of the recent progress made in device efficiency, the operation mechanisms of these devices are still not well-understood, especially the effects of ion migration. In this Chapter, the role of ion migration is investigated by measuring the transient electroluminescence and current responses, with both the current and efficiency showing a slow response in a time scale of tens of milliseconds. The results of the charge injection dynamics show that the slow response of the current is attributed to the migration and accumulation of halide ions at the anode interface, facilitating hole injection and leading to a strong charge imbalance. Further, the results of the charge recombination dynamics show that the slow response of the efficiency is attributed to enhanced charge injection facilitated by ion migration, which leads to an increased carrier density favoring bimolecular radiative recombination. Through a combined analysis of both charge injection and recombination dynamics, we finally present a comprehensive picture of the role of ion migration in device operation.

3.2 Introduction

Organometal halide perovskites have shown a great potential over the past decade for their applications of next-generation optoelectronic devices including photovoltaics,[1] transistors,[2] light-emitting diodes (LEDs)[3,4] and lasers[3,5] due to their unique properties of defect tolerance,[6–9] long carrier diffusion length,[10] high color purity,[11] bandgap tunability[12,13] and solution processability. Perovskite LEDs are specifically interesting because of the narrow emission bandwidth[11] compared with organic LEDs (OLEDs). To date, external quantum efficiencies (EQEs) above 20% have been achieved in both red[14,15] and green[16] perovskite LEDs. The rapid progress in device efficiency is mainly attributed to the structural and compositional engineering of perovskite light-emitting materials.[14–21] For example, high efficiency perovskite LEDs can be made by adding bulky organic cations in perovskites, not only promoting radiative recombination by forming low-dimensional nanostructures (quasi-2D perovskite[17–19] or nanocrystal perovskite[20]), but also suppressing non-radiative recombination through defect passivation.[21]

Despite the high efficiencies achieved by perovskite LEDs, an in-depth study of the role of ion migration on device operation is still lacking. Ion migration has been recognized as a key reason for photocurrent hysteresis in perovskite photovoltaics (PVs).[22–24] For perovskite light-emitting devices, ion migration leads to changes in the internal electric field affecting charge injection and electroluminescence (EL).[25–27] As a result, two interesting phenomena have been reported. The first phenomenon is polarity switchable EL which is done by applying an external bias in either direction to a device with two high work function electrodes.[25] Another phenomenon is reversible enhancement in charge injection and EL by pre-bias poling.[26,27] Both can be explained by enhanced charge injection as a result of ion accumulation at the electrode interfaces.[25–27] However, to further understand the role of ion migration in the operation of perovskite LEDs, three important issues need to be addressed. First, since ion migration and hence the ion distribution is a dynamic process affected by the applied electric field, it will affect the results of device measurements during the luminescence-current-voltage (LIV) scans. Therefore, the EL intensity and current are strongly affected by the voltage scan rate as well as the scan direction, leading to an uncertainty in device measurements. Specifically, the apparent measured efficiency has been found to vary with the measurement parameters such as the scan rate, scan direction and pre-bias conditions.[20,27,28] Second, mobile ions accumulated at the electrode interface affect charge injection. Specifically, mobile cations affect hole injection and mobile anions affect electron injection.[25–27] Therefore, it is important to differentiate the effects of ion migration on electron and hole injection and their roles in the overall device performance. Third, in addition to charge injection, ion migration can also affect charge recombination through increased charge carrier density and defect annihilation,[29–31] which eventually contributes to the dynamics of EL. Therefore, to better understand the device operation mechanism, it is necessary to carry out transient EL and current measurements to monitor the dynamics of charge injection and recombination in perovskite LEDs and study the interplay of the effects on charge injection and recombination due to ion migration.

To synthesize perovskite nanocrystals for LED fabrication, we first passivate grain boundary defects and constrain the growth of perovskite crystals by adding a bulky organic cation phenethylammonium bromide (PEABr) to methylammonium lead bromide ($MAPbBr_3$). To study the device operation mechanism and the effects of ion migration on the device performance, transient electroluminescence (Tr-EL) and transient current (Tr-J) measurements were carried out, from which the transient efficiency (Tr-CE) data were also extracted. From the results, all three parameters show a very slow response in a time scale of tens of milliseconds. To have an in-depth understanding of the origin of the slow current response, Tr-J measurements on single carrier devices were conducted to investigate the electron and hole injection dynamics separately and the results show that the slow response is due to a slow hole injection response as a result of migration and accumulation of Br ions at the anode interface facilitating hole injection. On the contrary, electron injection is not affected by Br ion migration. Such a different effect of ion migration on electron and hole injection leads to a strong charge imbalance in the resulting LEDs. To study the origin of the slow efficiency response, photoluminescence (PL) under pulse voltage measurements were conducted to investigate the charge recombination dynamics and the results show that the defect density is not reduced under an external electric field. Therefore, we attribute the increase of the efficiency to the enhanced charge injection facilitated by ion migration leading to an increased carrier density favoring bimolecular radiative recombination. Finally, a comprehensive picture of the device operation mechanisms will be presented.

3.3 Film characterizations and device performance

In this work, perovskite films were made by adding PEABr in $MAPbBr_3$ (in a molar ratio of 30%) to passivate grain boundary defects as well as to form low-dimensional perovskites for exciton confinement.[17–21] It is known that by adding bulky organic cations (PEABr in our case) to the perovskite precursors, either quasi-2D perovskite[17–19] or nanocrystal perovskite[20] can be formed. To determine the nanostructure of our perovskite films, UV-visible absorption and X-ray diffraction (XRD) measurements were conducted, and the results are shown in **Figure 3.1a&b** respectively. From the UV-visible absorption spectrum, we do not observe any absorption peaks from 2D perovskites and the absorption band edge at 530 nm indicates that only 3D perovskite is formed in our film. From the XRD pattern, again, we only observe a (100) diffraction peak of 3D perovskite at 14.8 degree. By doing Scherrer analysis on the (100) peak, we determined that the grain size is around 14 nm, indicating the existence of perovskite nanocrystals. Since the bulky organic cations do not contribute to forming quasi-2D perovskite, they function as an organic matrix in the presence of perovskite nanocrystals. Therefore, we conclude that our perovskite film consists of perovskite nanocrystals ($MAPbBr_3$) embedded in an organic matrix (PEABr).[20]

The perovskite LEDs used in our study have the following structure: ITO/ nickel oxide (NiO_x)/ perovskite (30% PEABr in $MAPbBr_3$)/ 2,2′,2"-(1,3,5-Benzinetriyl)-tris(1-phenyl-1-H-benzimidazole) (TPBi)/ Cs_2CO_3/ Al, where NiO_x is used as hole transporting layer (HTL) and TPBi is used as electron transporting layer (ETL) (**Figure 3.1c**). The device LIV characteristics are shown in **Figure 3.1d**, and a luminance above 2000 cd/m^2 is observed at 5 V, indicating a good quality device. The device shows a maximum current efficiency of 22 cd/A corresponding to an EQE of 7.7% as shown in **Figure 3.1e**. The FWHM of the EL spectrum is 21 nm, indicating a good color purity (**Figure 3.1f**). The peak wavelength of the EL spectrum is at 521 nm which is shorter than that of bulk $MAPbBr_3$ perovskite, corresponding to the reduced crystal size of 14 nm.[20] Here, the performance of the perovskite LED is comparable to those reported in the literature,[17–20] and therefore these devices can be used as a good reference to study ion migration in perovskite LEDs.

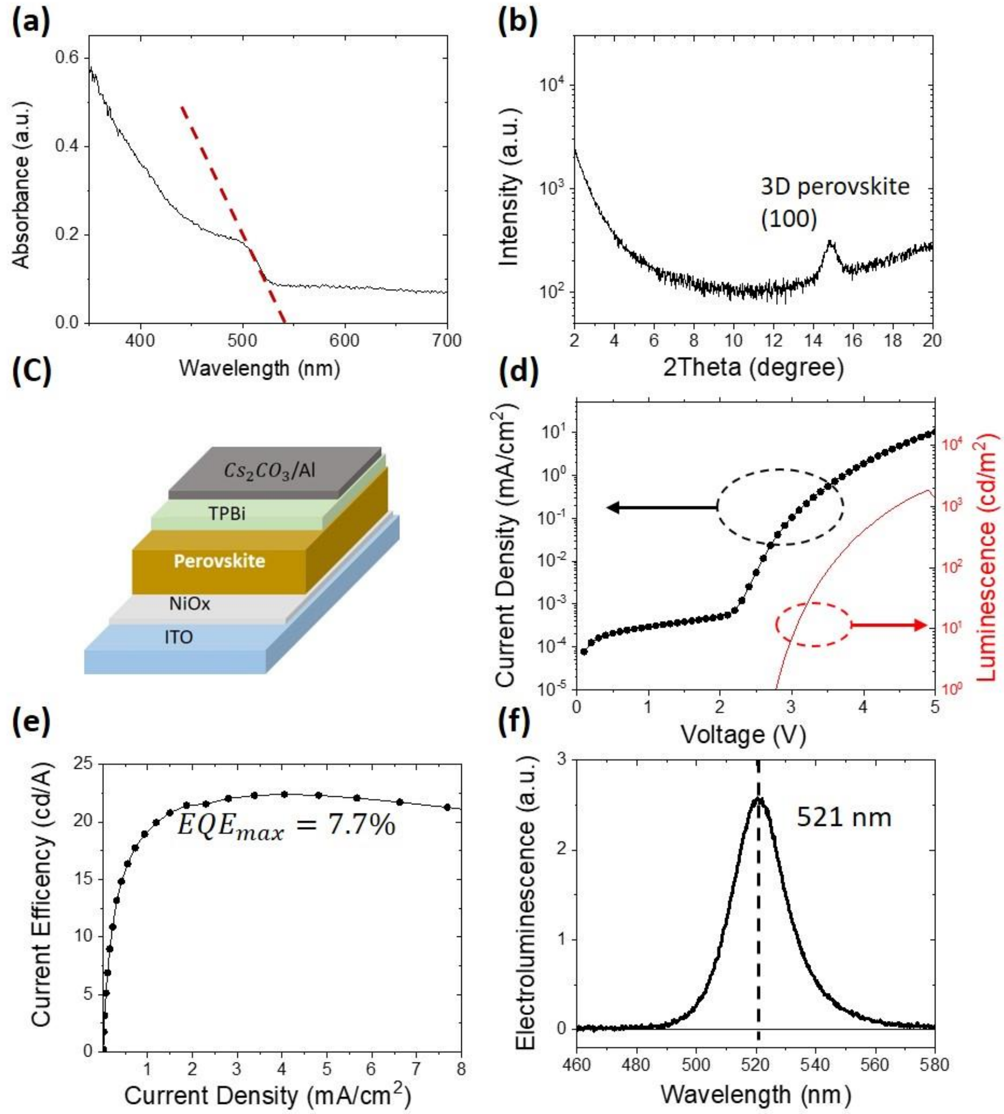

Figure 3.1 (a) Absorption and (b) X-ray diffraction of the perovskite film. (c) Schematic diagram of the device structure. (d) JVL curve and (e) current efficiency of the perovskite LED. (f) Spectrum of electroluminescence at 3.8 V.

3.4 Transient behaviors of perovskite LEDs

To study the device operation mechanism and the effects of ion migration on device performance, Tr-EL and Tr-J measurements were conducted by applying a pulse voltage (pulse width is 50 ms; frequency is 4 Hz; reference voltage is 0 V) on the device and monitoring the transient EL intensity and current density, and the results are shown in **Figures 3.2a&b**. From the results of the Tr-EL measurements, we found that the EL response time is up to 20 ms, which is almost four orders of magnitude longer than that in typical OLEDs.[32,33] It should be noted that the EL response time in OLEDs is mostly limited due to the carrier transit time in the devices which is typically on the order of a few microseconds depending of the carrier mobilities of the electron and hole transporting layers. From the results of Tr-J measurements, we observed a sharp peak in the beginning, followed by a slow increase also in a time scale of tens of milliseconds. The initial sharp rise comes from the RC response (estimated to be 0.125 ms) of the equivalent circuit of the device,[34] which is much longer than that in typical OLEDs.[33] We attribute this large RC response to ion migration in the perovskite resulting from the capacitance contribution due to ionic polarization.[25] The subsequent slow increase of the current partially accounts for the slow EL response. In order to determine whether the slow increase of the current is the only reason for the slow EL response, we divided the EL by the current density to extract the transient current efficiency of the device (**Figure 3.2c**). From the results, the efficiency also shows a slow response in a similar time scale. Therefore, the slow EL response is a combined result of the slow current response and the slow efficiency response. Since the transient current is an indication of the charge injection dynamics and the transient efficiency is an indication of the charge recombination dynamics, to better understand the operation mechanism of the perovskite LED, we carried out in-depth studies on these two aspects in the following sections.

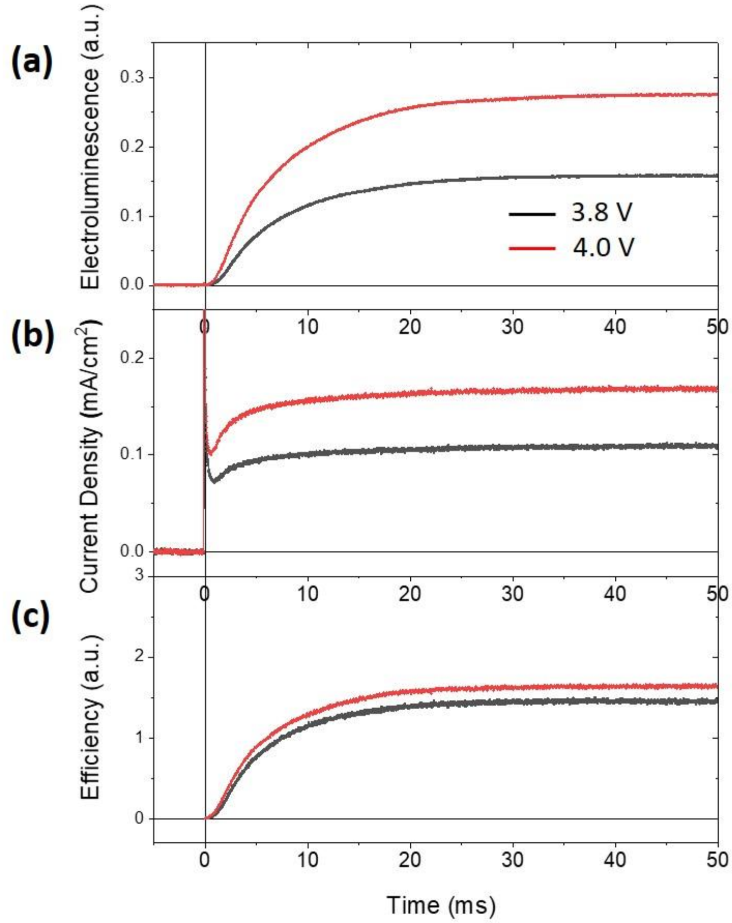

Figure 3.2 Transient (a) electroluminescence and (b) current (c) efficiency of the perovskite LED at different pulse voltages (pulse width=50 ms, frequency=4 Hz, reference voltage=0 V).

3.5 Charge injection dynamics

The slow current response (**Figure 3.2b**) of our perovskite LED can be attributed to ion migration in the perovskite. It has been reported that mobile ions in perovskites under electric field can migrate to the electrode interface.[25–27] When applying a forward bias to a perovskite LED, negative halide ions migrate to the anode interface facilitating hole injection, while positive MA^+ migrate to the cathode interface facilitating electron injection. Compared with the transport of charge carriers, the migration of ions is much slower, typically in a time scale of millisecond to second.[24] Therefore, the enhancement of charge injection facilitated by ion migration is expected to be slow, leading to a slow increase in the current. However, the slow current response of the perovskite LED is a combined result of electron and hole injection dynamics. To have a detailed understanding of the effect of ion migration on charge injection, we conducted Tr-J measurements on single carrier devices to examine the injection dynamics of electrons and holes separately.

Electron-only and hole-only devices fabricated have the following structures respectively: ITO/ aluminum-doped zinc oxide (AZO)/ perovskite/ TPBi/ Cs_2CO_3/ Al and ITO/ NiO_x/ perovskite/ MoO_x/ Au. In both cases, EL was not observed when current was injected into the devices, indicating they are truly single carrier devices. Tr-J measurements were conducted on single carrier devices by applying a pulse voltage (pulse width is 50 ms, frequency is 4 Hz, reference voltage is 0 V) and monitoring the evolution of the current density with time, and the results are shown in Figure 3. From the hole-only device Tr-J data (**Figure 3.3a**), after the initial RC response, there is a slow increase in the hole current with a time scale on the order of tens of milliseconds, similar to that of the current response of the perovskite LED. Therefore, we conclude that hole injection is enhanced by the accumulation of Br ions at the anode interface, contributing to the slow current response of the perovskite LED. From the electron-only device Tr-J data (**Figure 3.3b**), we observed a decrease after the initial RC response, indicating it does not contribute to the slow current response of the perovskite LED. The decrease of the electron current can be attributed to a screening effect of ionic polarization on the external electric field (the pulse voltage):[34] ion-migration-induced polarization generates an internal electric field which is in the opposite direction of the external electric field, leading to a decrease in the total electric field in the perovskite layer, thereby impeding the charge transport. In principle, hole transport in perovskite should also be affected by this screening effect. However, the enhanced hole injection at the anode interface due to ion migration plays a dominant role such that we mainly observed the slow increase in hole current. The very different electron and hole injection dynamics indicate that Br ions are the primary species responsible for ion migration in the perovskite layer. More importantly, due to such a different effect of ion migration on electron and hole injection, the steady-state hole current is more than one order of magnitude larger than the steady-state electron current (**Figure 3.3**), indicating a strong charge imbalance of the resulting perovskite LED during steady-state operation, leading to a narrow recombination zone located at the ETL interface and limiting the device efficiency. The implication of this important finding is that electron injection is the bottleneck to the device performance. Finally, it should be noted that the origin of the charge imbalance cannot be revealed by steady-state measurements, and temperature-dependent transient current measurements are needed to understand the device operation mechanism.

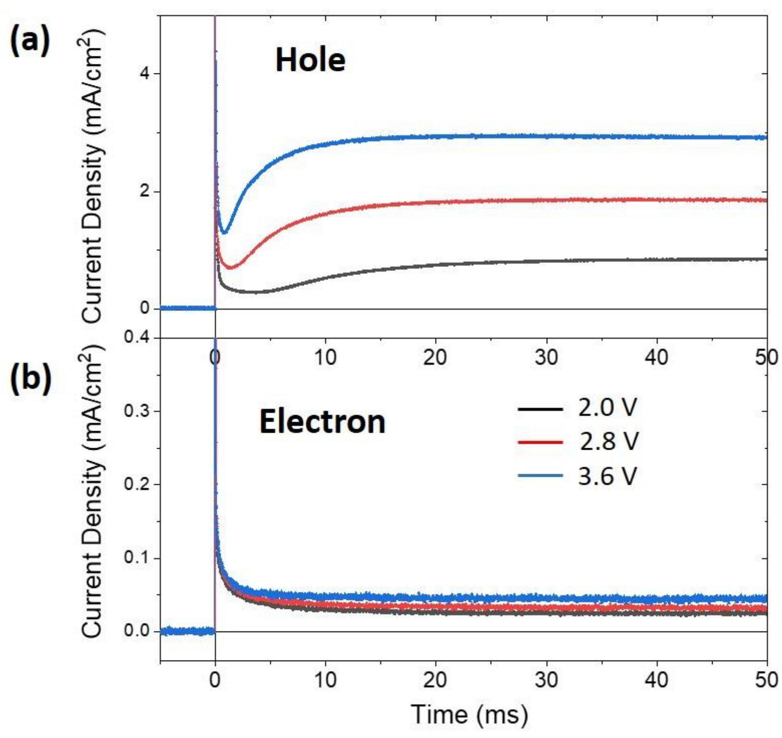

Figure 3.3 Transient current of (a) the hole-only device and (b) the electron-only device under different pulse voltages (reference voltage=0, frequency=4 Hz, pulse width=50 ms).

Here, we conducted temperature-dependent Tr-J measurements on hole-only devices to extract the activation energy of Br ion migration and the results are shown in **Figure 3.4**. As expected, we observed slower responses of hole current at lower temperatures. In addition, at lower temperatures, there is a decrease of the initial RC response prior the slow increase. As mentioned previously, this decrease is attributed to the screening effect of ionic polarization resulted in reduction of the electric field in the perovskite layer.[34] Therefore, to quantify the hole current, we divide it into three components with each one expressed by an exponential term:[34] (i) the initial RC response, $A_1\exp(-t/\tau_1)$; (ii) the decrease of the hole current due to the screening effect induced by Br ion migration, $A_2\exp(-t/\tau_2)$; (iii) the increase of the hole current due to the enhanced hole injection facilitated by the accumulation of Br ions at the anode interface, $A_3\exp(-t/\tau_3)$. Therefore, the hole current can be expressed using the equation below:

$$J = A_1 \exp\left(-\frac{t}{\tau_1}\right) + A_2 \exp\left(-\frac{t}{\tau_2}\right) + A_3 \exp\left(-\frac{t}{\tau_3}\right) + A_0 \qquad (3.1)$$

We fitted the measured hole current with Equation (3.1) and the results are shown in **Figure 3.4**. Fitting parameters are summarized in **Table 3.1**. Here, τ_2 and τ_3 are both due to Br ion migration, thus indicating the characteristic time of Br ion migration in the perovskite. Therefore, we have the following approximate relationships:[34]

$$k_2 = \frac{1}{\tau_2} \sim \sigma = C \exp\left(-\frac{E_a}{kT}\right) \qquad (3.2) \qquad\qquad k_3 = \frac{1}{\tau_3} \sim \sigma = C \exp\left(-\frac{E_a}{kT}\right) \qquad (3.3)$$

where σ is the ionic conductivity, C is a constant coefficient, E_a is the activation energy of Br ion migration, k is the Boltzmann constant and T is the temperature. To extract the activation energy, we conducted linear fittings on ln (k_2) and ln (k_3) versus 1/kT, and the results are shown in **Figure 3.5**. The slopes of the linear fittings give the activation energy. From the results, we found that the activation energy extracted from k_2 (0.20 eV) is close to that of k_3 (0.18 eV), which is about the same as expected since they are both induced by Br ion migration. Therefore, the activation energy of Br ion migration in our perovskite is calculated to be 0.18~0.20 eV, consistent with the values reported in the literature.[35–37] This quantitative analysis verifies that the slow hole current response is induced by Br ion migration.

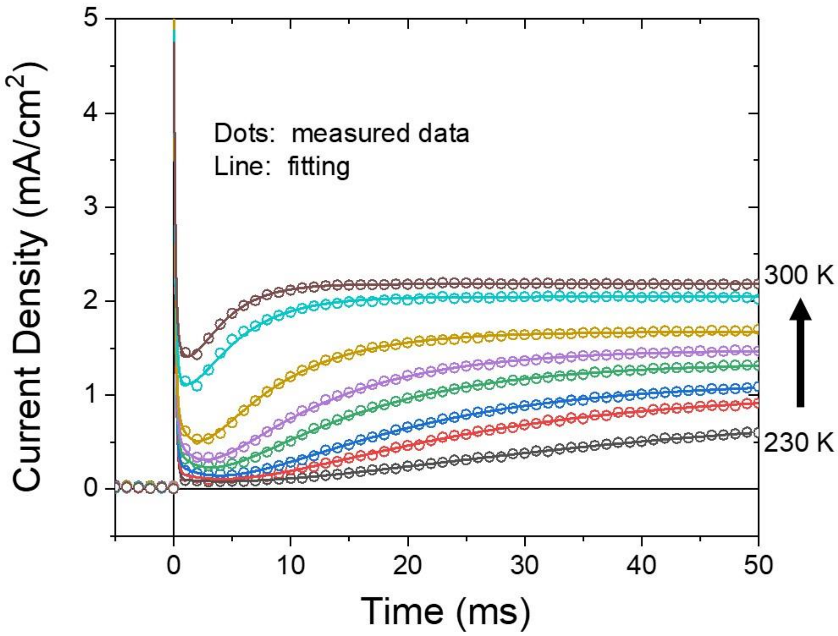

Figure 3.4 Transient current of the hole-only device at different temperatures with pulse voltage being 3.0 V (reference voltage=0 V, frequency=4 Hz, pulse width=50 ms). The temperature increment is 10 K. Hollow dots are experimental data, while solid lines are fitted curves.

Table 3.1 Fitting parameters of hole injection current at different temperatures.

T (K)	τ_1(s)	τ_2 (s)	τ_3 (s)	k_1 (s^{-1})	k_2 (s^{-1})	k_3 (s^{-1})
230	1.27E-04	1.23E-02	2.75E-02	7.87E+03	8.13E+01	3.64E+01
240	1.25E-04	7.16E-03	1.81E-02	8.00E+03	1.40E+02	5.52E+01
250	1.22E-04	5.22E-03	1.47E-02	8.20E+03	1.92E+02	6.80E+01
260	1.32E-04	3.25E-03	1.23E-02	7.58E+03	3.08E+02	8.13E+01
270	1.29E-04	2.35E-03	1.03E-02	7.75E+03	4.26E+02	9.71E+01
280	1.18E-04	1.64E-03	6.91E-03	8.47E+03	6.10E+02	1.45E+02
290	1.23E-04	1.40E-03	4.00E-03	8.13E+03	7.14E+02	2.50E+02
300	1.25E-04	1.18E-03	2.82E-03	8.00E+03	8.47E+02	3.55E+02

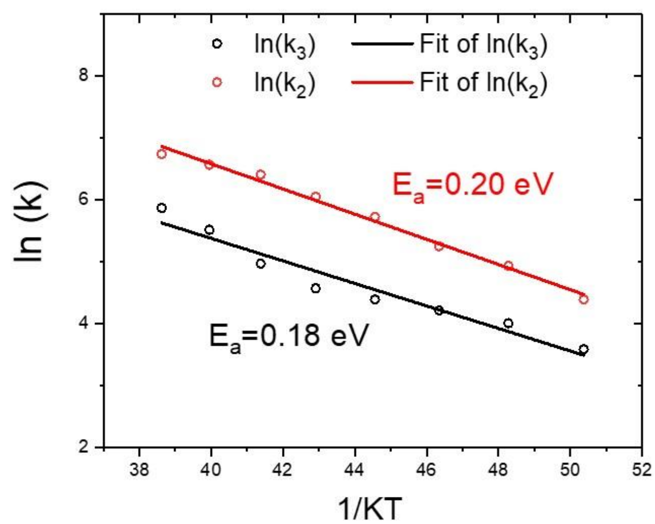

Figure 3.5 Extract activation energy of Br ion migration by linear fitting.

3.6 Charge recombination dynamics

In addition to the charge injection dynamics as we addressed in the last section, charge recombination dynamics is another fundamental process in the operation of a perovskite LED, resulting in a slow efficiency response (**Figure 3.2c**). One of the reasons for the slow efficiency response is the enhanced charge injection facilitated by ion migration increasing the carrier density in the perovskite layer. Since defect-assisted non-radiative recombination is monomolecular and radiative recombination is bimolecular, we expect that a higher carrier density in the perovskite layer favors radiative recombination.[21] Under forward bias, hole injection in the perovskite LED is enhanced, leading to an accumulation of excess holes at the ETL/perovskites interface, which subsequently facilitates electron injection into the perovskite layer. Therefore, the increased injected carrier density in the perovskite layer results in an enhanced efficiency, leading to a slow increase in efficiency. Further, a reduction of defect density in perovskite under electric field could be another reason for the higher efficiency. It has been reported that under photoexcitation or electric field, pairs of halide interstitials and vacancies migrate and annihilate in perovskite, leading to a reduction of defect density and an increase in radiative recombination efficiency.[29–31] To determine whether this effect also contributes to the slow response of the efficiency, we conducted PL measurements under pulse voltage to investigate the effects of electric field on radiative recombination.

In order to rule out EL and the effects of charge injection on PL, the device used for the PL measurements has a structure of ITO/ HfO_2 (40 nm)/ perovskite/ Poly (methyl methacrylate) (PMMA) (40 nm)/Al, where HfO_2 and PMMA are two insulating layers blocking charge injection. The experimental set-up is shown in **Figure 3.6a**: the perovskite sample is excited by a 405 nm diode laser under an applied pulse voltage and the PL intensity is monitored by a photodetector with the signal connected to an oscilloscope. The measurement results are shown in **Figure 3.6b**. From the results, we found that the applied electric field has a small effect on the PL intensity, indicating that the radiative recombination efficiency is only slightly perturbed by the electric field. To understand the origin of this perturbation, we magnified the signals, and the data are shown in

Figure 3.6c. Here, the PL data shows five characteristic regions: region 1 is a constant PL intensity without external electric field; region 2 is an abrupt drop of the PL intensity right after the application of the external electric field (pulse voltage); region 3 is a slow increase in the PL intensity under the external electric field; region 4 is an abrupt drop of the PL intensity right after the removal of the external electric field; region 5 is a slow recovering of PL after the removal of the external electric field.

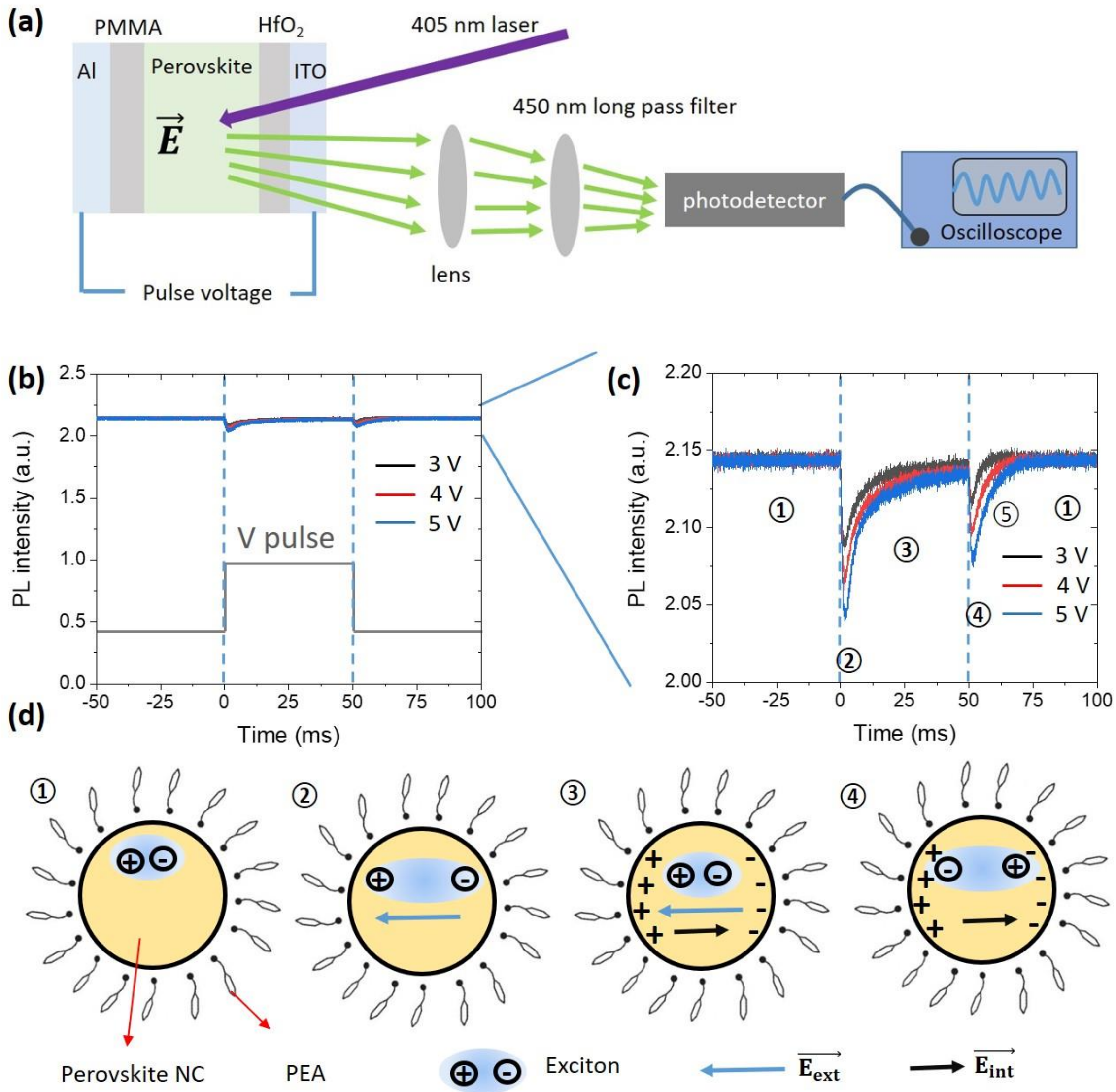

Figure 3.6 (a) Schematic diagram showing the set-up of PL under pulse voltage. (b) Photoluminescence (PL) of a perovskite device (ITO/HfO_2/perovskite/PMMA/Al) under different pulse voltages. (c) Magnification of (b). (d) Schematic diagrams illustrating the effects of electric field on exciton dynamics at different regions of (b): ① no electric field; ② external electric field separates exciton; ③ external electric field is screened by internal electric field induced by ion migration; ④ ion-migration-induced internal electric field separates exciton.

We propose that the evolution of the PL intensity can be explained by Br ion migration in the perovskite layer. As we mentioned previously, we have perovskite nanocrystals ($MAPbBr_3$) embedded in an organic matrix (PEABr), as shown in **Figure 3.6d①**. Therefore, both excitons and mobile ions are confined in the nanocrystals. From region 1 to region 2, upon an application of the electric field, electrons and holes are pulled away from each other in the nanocrystals, leading to an abrupt decrease in the radiative recombination efficiency[38] (**Figure 3.6d①&②**). From region 2 to region 3, ion-migration-induced polarization driven by the external electric field generates an internal electric field that is in the opposite direction. As a result, the total electric field is decreased, leading to a slow increase in the radiative recombination efficiency (**Figure 3.6d②&③**). From region 3 to region 4, the external electric field is instantly removed, leaving the internal electric field alone in the perovskite. Therefore, the total electric field is abruptly reversed and increased, leading to an abrupt decrease in the radiative recombination efficiency (**Figure 3.6d③&④**). From region 4 to region 5, without external electric field, mobile halide ions diffuse back, leading to a decrease in the total electric field and a recovery of the radiative recombination efficiency.

Based on the analysis above, we conclude that the small perturbation (about 10%) on PL by the voltage pulse is due to the interplay between the applied external electric field and the ion-migration-induced internal electric field. Here, we do not observe any evidence of the reduction of defect density in perovskite under electric field. It should be noted that the change in the PL intensity due to electric field is very small compared with the change in the EL efficiency, indicating that the slow efficiency response of the perovskite LED is mainly due to the enhanced charge injection that increases the carrier density in the perovskite layer.

Combining the investigations on charge injection and recombination dynamics, we present the operation of the device in **Figure 3.7**. As soon as a forward bias is applied (**Figure 3.7a**), limited charge carriers are injected into the perovskite layer resulting in a low EL intensity. As the electrical stress continues (**Figure 3.7b**), mobile Br ions in the perovskite layer migrate to the HTL/perovskite interface, facilitating hole injection. The increased hole injection efficiency leads to an accumulation of excess holes at the ETL/perovskites interface, which subsequently facilitates electron injection into the perovskite layer, resulting in a slow increase of the current. In addition, due to the enhanced charge injection efficiency, both the density of electron and hole are increased in the perovskite layer, which favors bimolecular radiative recombination, leading to a slow increase of the efficiency. The slow current response and the slow efficiency response together result in the slow EL response.

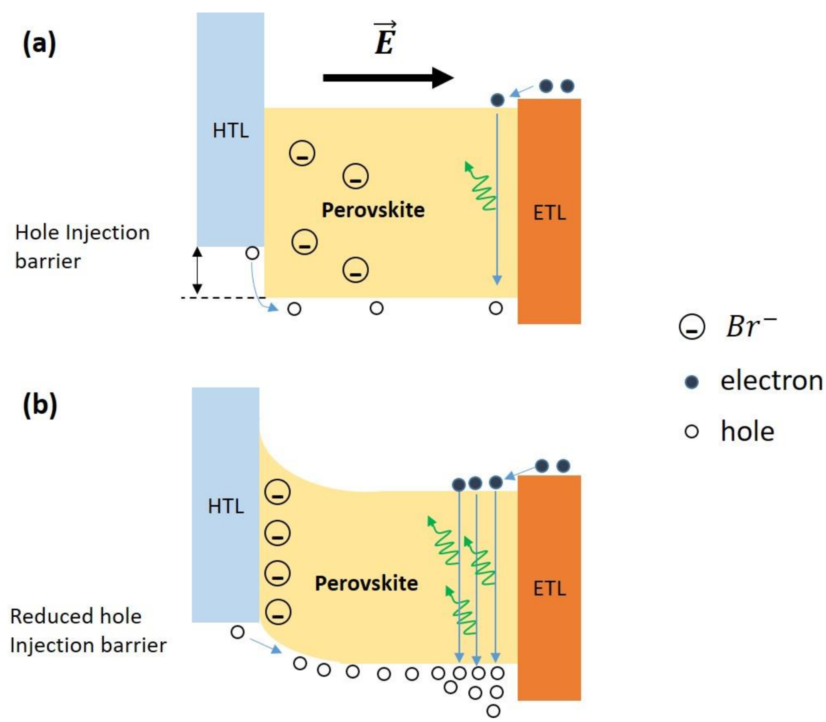

Figure 3.7 Schematic diagram showing the role of halide ions in the operation of perovskite LED. (a) In the beginning of the pulse voltage. (b) At 10 ms of the pulse voltage.

3.7 Conclusion

In this work, we studied the role of ion migration in the operation of perovskite LEDs by transient measurements, where the EL intensity, the current density and the device efficiency all show a slow response in a time scale of tens of milliseconds. Through Tr-J measurements on single carrier devices, the data revealed that the slow current response is due to a slow hole injection response which is attributed to the migration and accumulation of the Br ions at the anode interface facilitating hole injection. On the contrary, electron injection is not affected by ion migration. Such a different effect of ion migration on electron and hole injection leads to a strong charge imbalance, suggesting that to enhance the device efficiency electron injection needs to be significantly enhanced to compensate for the enhanced hole injection facilitated by halide ion migration. In addition, through PL measurements under pulse voltage, we identified that the slow efficiency response is mainly attributed to the enhanced charge injection which leads to an increased carrier density favoring bimolecular radiative recombination. Our findings shed light on the understanding of the device physics of perovskite LEDs, thereby paved the way for the future design of device architecture and materials to realize the full potential of perovskites LEDs.

3.8 Methods

Materials

Nickel acetate tetrahydrate (99.998% trace metal basis), ethanol (99.5%, anhydrous), ethanolamine (99.0% ACS reagent), lead bromide (99.999% trace metals basis), N,N-dimethylformamide (DMF) (99.8%, anhydrous), dimethyl sulfoxide (DMSO) (99.9%, anhydrous), chlorobenzene (CB) (99.8%, anhydrous) cesium carbonate (Cs_2CO_3) (99.9%, trace metal basis), polyvinylpyrrolidone (PVP), Aluminum-doped zinc oxide (AZO) (2.5 wt %) nanoparticle ink and Poly(methyl methacrylate) (PMMA) are from Sigma Aldrich. Phenethylammonium bromide

(PEABr) and methylammonium bromide (MABr) are from Dyesol. 2,2′,2"-(1,3,5-Benzinetriyl)-tris(1-phenyl-1-H-benzimidazole) (TPBi) is from Lumtec. Aluminum pellets, Gold pellets and MoO_x are from Kurt J. Lesker.

Device fabrications

For the perovskite LEDs, glass substrates with ITO pattern were cleaned by acetone and isopropanol in sequence in ultrasonic bath, followed by UV ozone treatment for 15 min before using. Nickel oxide thin films were fabricated by sol-gel method: 248.8 mg of nickel acetate tetrahydrate and 60 uL of ethanolamine were dissolved into 5 mL of ethanol, which was stirred at 65 ℃ for 45 min to form a stable sol-gel. Then the nickel oxide precursor was spin coated on the cleaned substrates at a speed of 3000 rpm for 1 min, followed by annealing in ambient at 500 ℃ for 1 hour. Perovskite films were fabricated on the nickel oxide film by spin coating method assisted with anti-solvent treatment in nitrogen-filled glove box. The precursor solution of the perovskite was prepared by dissolving 108 mg of lead bromide, 33 mg of MABr and 17.8 mg of PEABr into 1 mL of a mixed solvent (DMSO/DMF=12/88). Before fabricating perovskite films, a solution of PVP (4 mg/mL in DMF) was spin coated on the nickel oxide film at a speed of 4000 rpm to passivate the surface defects of the nickel oxide, followed by annealing at 120 ℃ for 10 min. Then the perovskite solution was spin coated on the passivated nickel oxide film at a speed of 4000 rpm for 2 min, during which 100 uL of CB was dropped on the sample at 5^{th} second. After spin coating, the sample was annealed at 80 ℃ for 10 min to evaporate the residual solvents and complete the crystallization of perovskite. To complete the device, 40 nm of TPBi as electron transporting layer and Cs_2CO_3 (2nm)/Al (100nm) as cathode were thermally evaporated in sequence on the perovskite film. For the electron-only devices, the NiO_x layer was replaced by AZO layer which was fabricated by spin coating AZO nanoparticle ink at a speed of 3000 rpm, followed by thermal annealing at 150 degree for 10 min in ambient. For the hole-only devices, TPBi and cathode were replaced by 15 nm of MoO_x and 80 nm of Au, which were thermally evaporated on the as-prepared perovskite films. For the device that is used for the PL measurement under pulse voltage, 40 nm of HfO_2 was fabricated by atomic layer deposition (Ultratech/Cambridge Nanotech Savannah) on cleaned ITO substrate. Then perovskite film was fabricated on the HfO_2 layer, followed by spin coating 40 nm of PMMA (20 mg/mL in CB) on the top of the perovskite. Lastly, 100 nm of Al was evaporated on the PMMA layer to complete the device fabrication.

Characterizations

Current-voltage-luminance (J-V-L) measurements were conducted by Keithley 2400 and a photodetector. Electroluminescence spectrum was measured by a high-resolution spectrometer (HR4000) from Ocean Optics. In the transient measurements, a pulse voltage generated by a function generator (Agilent 33220A) was applied to the device. To monitor the dynamics of the electroluminescence in the transient measurements, a photomultiplier tube (PMT) powered by a voltage source (C9525-02 from Hamamatsu) was used, whose signal is connected to an oscilloscope (Tektronix MDO3014). In addition, the device is connected in series with a resistor (9850 ohm) whose voltage signal was led into the oscilloscope to monitor the dynamics of current density. X-ray diffraction was conducted by Rigaku SmartLab X-Ray Diffractometer (XRD). UV-visible absorption was done by Lambda 750 UV/Vis spectrometer from PerkinElmer.

REFERENCES

[1] F. Huang, M. Li, P. Siffalovic, G. Cao, J. Tian, From Scalable Solution Fabrication of Perovskite Films towards Commercialization of Solar Cells, *Energy Environ. Sci.* **2019**, 12, 518–549.

[2] X. Liu, D. Yu, X. Song, H. Zeng, Metal Halide Perovskites: Synthesis, Ion Migration, and Application in Field-Effect Transistors, *Small* **2018**, 14, 1801460.

[3] S. A. Veldhuis, P. P. Boix, N. Yantara, M. Li, T. C. Sum, N. Mathews, S. G. Mhaisalkar, Perovskite Materials for Light-Emitting Diodes and Lasers, *Adv. Mater.* **2016**, 28, 6804–6834.

[4] Q. Shan, J. Song, Y. Zou, J. Li, L. Xu, J. Xue, Y. Dong, B. Han, J. Chen, H. Zeng, High Performance Metal Halide Perovskite Light-Emitting Diode: From Material Design to Device Optimization, *Small* **2017**, 13, 1701770.

[5] M. M. Stylianakis, T. Maksudov, A. Panagiotopoulos, G. Kakavelakis, K. Petridis, Inorganic and Hybrid Perovskite Based Laser Devices: A Review, *Materials (Basel).* **2019**, 16, 859.

[6] W. J. Yin, T. Shi, Y. Yan, Unusual Defect Physics in CH3NH3PbI3 Perovskite Solar Cell Absorber, *Appl. Phys. Lett.* **2014**, 104, 063903.

[7] A. Buin, P. Pietsch, J. Xu, O. Voznyy, A. H. Ip, R. Comin, E. H. Sargent, Materials Processing Routes to Trap-Free Halide Perovskites, *Nano Lett.* **2014**, 14, 6281–6286.

[8] K. X. Steirer, P. Schulz, G. Teeter, V. Stevanovic, M. Yang, K. Zhu, J. J. Berry, Defect Tolerance in Methylammonium Lead Triiodide Perovskite, *ACS Energy Lett.* **2016**, 1, 360–366.

[9] D. Meggiolaro, S. G. Motti, E. Mosconi, A. J. Barker, J. Ball, C. Andrea Riccardo Perini, F. Deschler, A. Petrozza, F. De Angelis, Iodine Chemistry Determines the Defect Tolerance of Lead-Halide Perovskites, *Energy Environ. Sci.* **2018**, 11, 702–713.

[10] M. J. P. Alcocer, T. Leijtens, L. M. Herz, A. Petrozza, H. J. Snaith, Electron-Hole Diffusion

Lengths Exceeding Trihalide Perovskite Absorber, *Science (80-.).* **2013**, 342, 341–344.

[11] J. Si, Y. Liu, Z. He, H. Du, K. Du, D. Chen, J. Li, M. Xu, H. Tian, H. He, D. Di, C. Lin, Y. Cheng, J. Wang, Y. Jin, Efficient and High-Color-Purity Light-Emitting Diodes Based on in Situ Grown Films of CsPbX3 (X = Br, I) Nanoplates with Controlled Thicknesses, *ACS Nano* **2017**, 11, 11100–11107.

[12] D. P. McMeekin, G. Sadoughi, W. Rehman, G. E. Eperon, M. Saliba, M. T. Hörantner, A. Haghighirad, N. Sakai, L. Korte, B. Rech, M. B. Johnston, L. M. Herz, H. J. Snaith, M. T. Horantner, A. Haghighirad, N. Sakai, L. Korte, B. Rech, M. B. Johnston, L. M. Herz, H. J. Snaith, A Mixed-Cation Lead Mixed-Halide Perovskite Absorber for Tandem Solar Cells, *Science (80-.).* **2016**, 351, 151–155.

[13] S. Pathak, N. Sakai, F. Wisnivesky Rocca Rivarola, S. D. Stranks, J. Liu, G. E. Eperon, C. Ducati, K. Wojciechowski, J. T. Griffiths, A. A. Haghighirad, A. Pellaroque, R. H. Friend, H. J. Snaith, Perovskite Crystals for Tunable White Light Emission, *Chem. Mater.* **2015**, 27, 8066–8075.

[14] Y. Cao, N. Wang, H. Tian, J. Guo, Y. Wei, H. Chen, Y. Miao, W. Zou, K. Pan, Y. He, H. Cao, Y. Ke, M. Xu, Y. Wang, M. Yang, K. Du, Z. Fu, D. Kong, D. Dai, Y. Jin, G. Li, H. Li, Q. Peng, J. Wang, W. Huang, Perovskite Light-Emitting Diodes Based on Spontaneously Formed Submicrometre-Scale Structures, *Nature* **2018**, 562, 249–253.

[15] B. Zhao, S. Bai, V. Kim, R. Lamboll, R. Shivanna, F. Auras, J. M. Richter, L. Yang, L. Dai, M. Alsari, X.-J. She, L. Liang, J. Zhang, S. Lilliu, P. Gao, H. J. Snaith, J. Wang, N. C. Greenham, R. H. Friend, D. Di, High-Efficiency Perovskite–Polymer Bulk Heterostructure Light-Emitting Diodes, *Nat. Photonics* **2018**, 12, 783–789.

[16] K. Lin, J. Xing, L. N. Quan, F. P. G. de Arquer, X. Gong, J. Lu, L. Xie, W. Zhao, D. Zhang, C. Yan, W. Li, X. Liu, Y. Lu, J. Kirman, E. H. Sargent, Q. Xiong, Z. Wei, Perovskite Light-Emitting Diodes with External Quantum Efficiency Exceeding 20 per Cent, *Nature* **2018**, 562, 245–248.

[17] M. Yuan, L. N. N. Quan, R. Comin, G. Walters, R. Sabatini, O. Voznyy, S. Hoogland, Y.

Zhao, E. M. M. Beauregard, P. Kanjanaboos, Z. Lu, D. H. H. Kim, E. H. H. Sargent, Perovskite Energy Funnels for Efficient Light-Emitting Diodes, *Nat. Nanotechnol.* **2016**, 11, 872–877.

[18] X. Yang, X. Zhang, J. Deng, Z. Chu, Q. Jiang, J. Meng, P. Wang, L. Zhang, Z. Yin, J. You, Efficient Green Light-Emitting Diodes Based on Quasi-Two-Dimensional Composition and Phase Engineered Perovskite with Surface Passivation, *Nat. Commun.* **2018**, 9, 570.

[19] N. Wang, L. Cheng, R. Ge, S. Zhang, Y. Miao, W. Zou, C. Yi, Y. Sun, Y. Cao, R. Yang, Y. Wei, Q. Guo, Y. Ke, M. Yu, Y. Jin, Y. Liu, Q. Ding, D. Di, L. Yang, G. Xing, H. Tian, C. Jin, F. Gao, R. H. H. Friend, J. Wang, W. Huang, Perovskite Light-Emitting Diodes Based on Solution-Processed Self-Organized Multiple Quantum Wells, *Nat. Photonics* **2016**, 10, 699–704.

[20] Z. Xiao, R. A. A. Kerner, L. Zhao, N. L. L. Tran, K. M. M. Lee, T.-W. Koh, G. D. D. Scholes, B. P. P. Rand, Efficient Perovskite Light-Emitting Diodes Featuring Nanometre-Sized Crystallites, *Nat. Photonics* **2017**, 11, 108–115.

[21] G. Xing, B. Wu, X. Wu, M. Li, B. Du, Q. Wei, J. Guo, E. K. L. L. Yeow, T. C. Sum, W. Huang, Transcending the Slow Bimolecular Recombination in Lead-Halide Perovskites for Electroluminescence, *Nat. Commun.* **2017**, 8, 14558.

[22] B. Chen, M. Yang, X. Zheng, C. Wu, W. Li, Y. Yan, J. Bisquert, G. Garcia-Belmonte, K. Zhu, S. Priya, Impact of Capacitive Effect and Ion Migration on the Hysteretic Behavior of Perovskite Solar Cells, *J. Phys. Chem. Lett.* **2015**, 6, 4693–4700.

[23] P. Calado, A. M. Telford, D. Bryant, X. Li, J. Nelson, B. C. O'Regan, P. R. F. Barnes, Evidence for Ion Migration in Hybrid Perovskite Solar Cells with Minimal Hysteresis, *Nat. Commun.* **2016**, 7, 13831.

[24] Y. Yuan, J. Huang, Ion Migration in Organometal Trihalide Perovskite and Its Impact on Photovoltaic Efficiency and Stability, *Acc. Chem. Res.* **2016**, 49, 286–293.

[25] H. Zhang, H. Lin, C. Liang, H. Liu, J. Liang, Y. Zhao, W. Zhang, M. Sun, W. Xiao, H. Li, S. Polizzi, D. Li, F. Zhang, Z. He, W. C. H. Choy, Organic-Inorganic Perovskite Light-

Emitting Electrochemical Cells with a Large Capacitance, *Adv. Funct. Mater.* **2015**, 25, 7226–7232.

[26] P. Andričević, X. Mettan, M. Kollár, B. Náfrádi, A. Sienkiewicz, T. Garma, L. Rossi, L. Forró, E. Horváth, Light-Emitting Electrochemical Cells of Single Crystal Hybrid Halide Perovskite with Vertically Aligned Carbon Nanotubes Contacts, *ACS Photonics* **2019**, 6, 967–975.

[27] E. Bandiello, J. Ávila, L. Gil-Escrig, E. Tekelenburg, M. Sessolo, H. J. Bolink, Influence of Mobile Ions on the Electroluminescence Characteristics of Methylammonium Lead Iodide Perovskite Diodes, *J. Mater. Chem. A* **2016**, 4, 18614–18620.

[28] H. Kim, L. Zhao, J. S. Price, A. J. Grede, K. Roh, A. N. Brigeman, M. Lopez, B. P. Rand, N. C. Giebink, Hybrid Perovskite Light Emitting Diodes under Intense Electrical Excitation, *Nat. Commun.* **2018**, 9, 4893.

[29] D. W. DeQuilettes, W. Zhang, V. M. Burlakov, D. J. Graham, T. Leijtens, A. Osherov, V. Bulović, H. J. Snaith, D. S. Ginger, S. D. Stranks, Photo-Induced Halide Redistribution in Organic-Inorganic Perovskite Films, *Nat. Commun.* **2016**, 7, 11683.

[30] L. Zhao, J. Gao, Y. H. L. Lin, Y. W. Yeh, K. M. Lee, N. Yao, Y. L. Loo, B. P. Rand, Electrical Stress Influences the Efficiency of CH3NH3PbI3 Perovskite Light Emitting Devices, *Adv. Mater.* **2017**, 29, 1605317.

[31] E. Mosconi, D. Meggiolaro, H. J. Snaith, S. D. Stranks, F. De Angelis, Light-Induced Annihilation of Frenkel Defects in Organo-Lead Halide Perovskites, *Energy Environ. Sci.* **2016**, 9, 3180–3187.

[32] M. Te Lin, M. Li, W. H. Chen, M. A. Omary, N. D. Shepherd, Transient Electroluminescence Determination of Carrier Mobility and Charge Trapping Effects in Heavily Doped Phosphorescent Organic Light-Emitting Diodes, *Solid. State. Electron.* **2011**, 56, 196–200.

[33] J. H. Lee, C. H. Chen, B. Y. Lin, Y. C. Shih, K. F. Lin, L. Wang, T. L. Chiu, C. F. Lin, Effect of Trapped Electrons on the Transient Current Density and Luminance of Organic

Light-Emitting Diode, *J. Phys. D. Appl. Phys.* **2018**, 51, 144003.

[34] D. Li, H. Wu, H. C. Cheng, G. Wang, Y. Huang, X. Duan, Electronic and Ionic Transport Dynamics in Organolead Halide Perovskites, *ACS Nano* **2016**, 10, 6933–6941.

[35] S. Meloni, T. Moehl, W. Tress, M. Franckeviius, M. Saliba, Y. H. Lee, P. Gao, M. K. Nazeeruddin, S. M. Zakeeruddin, U. Rothlisberger, M. Graetzel, Ionic Polarization-Induced Current-Voltage Hysteresis in CH3NH3PbX3 Perovskite Solar Cells, *Nat. Commun.* **2016**, 7, 10334.

[36] M. Chen, X. Shan, T. Geske, J. Li, Z. Yu, Manipulating Ion Migration for Highly Stable Light-Emitting Diodes with Single-Crystalline Organometal Halide Perovskite Microplatelets, *ACS Nano* **2017**, 11, 6312–6318.

[37] A. Oranskaia, J. Yin, O. M. Bakr, J. L. Brédas, O. F. Mohammed, Halogen Migration in Hybrid Perovskites: The Organic Cation Matters, *J. Phys. Chem. Lett.* **2018**, 9, 5474–5480.

[38] Z. Xu, T. De Rosia, K. Weeks, Photoluminescence-Voltage (PL-V) Hysteresis of Perovskite Solar Cells, *J. Phys. Chem. C* **2017**, 121, 24389–24396.

CHAPTER 4: CAVITY FINE-TUNING FOR PEROVSKITE DFB LASERS

This chapter will be published:

Q. Dong, X. Fu, D. Seyitliyev, K. Darabi, J. Mendes, L. Lei, Y. Chen, K. Gundogdu, A. Amassian, C.-H. Chang, F. So, Facile Fabrication of High-Performance Solution-Processed Distributed Feedback Lasers, manuscript under revision.

4.1 Abstract

Solution processed distributed-feedback (DFB) lasers have been regarded as the next-generation coherent light sources due to their low fabrication-cost and single-mode operation. Although good laser performance has been demonstrated from these devices, fine-tuning of the cavity is still a challenge due to the lack of a systematic guidance and the time-consuming cavity-fabrication process. In this Chapter, a metal-halide perovskite is used as a prototypical gain material to demonstrate a facile and systematic methodology for fine-tuning the cavity of solution-processed surface-emitting DFB lasers. The cavity-fabrication is simplified by adding a polymer polyvinylpyrrolidone (PVP) into the perovskite solution, enabling a simple nanoimprint on the perovskite film, while the cavity fine-tuning is guided by a systematic analysis of the optical modes in the DFB structures, aiming at an optimal overlap of the resonant wavelength with the gain spectrum. Using this methodology, the process of fine-tuning the laser cavity is very much simplified.

4.2 Introduction

Solution-processed semiconductors including organic small molecules, conjugated polymers, colloidal quantum dots and metal-halide perovskites have been recognized as promising gain media for coherent light sources in various photonic applications due to their low-cost fabrications.[1–3] Among different optical resonators, distributed feedback (DFB) cavities are of great interest due to their single-mode operation, low threshold, and the utilization of Bragg diffraction instead of fabrication of high-quality facets or mirrors to provide the optical feedback. Although optically pumped DFB lasers based on these solution-processed semiconductors have been reported to show a decent performance,[1–3] the process to fine-tune the cavity is laborious, making it extremely tedious to achieve an optimized performance. Specifically, the resonant wavelength of the DFB cavity should be located within the gain spectrum of the gain medium, and for the optimal laser performance, the resonant wavelength should also be located at the gain maximum. To do that, first, the gain spectrum needs to be determined, and subsequently the cavity needs to be fine-tuned to match the gain maximum. Fine-tuning the cavity enables the tuning of the resonant wavelength, which is commonly achieved by changing the grating period.[4] However, without knowing the fine-tuning direction, a random try of a series of grating periods is needed, which greatly slows down the fine-tuning process.

In addition to the guidance on the cavity fine-tuning, a facile fabrication of the cavities is also critical to reduce the amount of effort for achieving an optimized laser performance. Here, we choose metal-halide perovskites as a prototypical solution-processed semiconductor for the study due to their high photoluminescence quantum yield (PLQY),[5] large absorption coefficient,[6] defect tolerance,[7,8] and broadband tunability.[9,10] The common ways to fabricate a perovskite DFB cavity in the literature is to nanopattern a substrate followed by depositing a perovskite film, which can be done by either etching the substrate or nanoimprinting on an UV-curable epoxy.[11–14] However, the former is tedious and time-consuming, and the latter results in low-quality perovskite films due to the poor wettability of the perovskite solutions on the nanopatterned epoxy.[15] Instead of nanopatterning the substrate, nanoimprinting on the perovskite film has recently been reported to be a better approach, as the large refractive index contrast at the corrugation interface between the perovskite and the air can lead to a higher quality-factor of the cavity.[16,17] However, this approach is also challenging due to the thermal instability and the unmanageable crystal growth of the perovskites during the nanoimprint process, where the pressure and temperature need to be carefully controlled to obtain good-quality perovskites as well as gratings.[18–21]

To address the issues above, in this work, we demonstrate a facile and systematic methodology to accelerate the cavity fine-tuning process of solution-processed surface-emitting DFB lasers by using a metal-halide perovskite (methylammonium lead bromide, $MAPbBr_3$) as an example. To realize a facile fabrication of the cavities, a polymer polyvinylpyrrolidone (PVP) is added into the perovskite precursor solutions, enabling the formation of a stable and soft precursor film after spin coating, which can be readily nanoimprinted by a polydimethylsiloxane (PDMS) mold, forming well-shaped gratings. To guide the cavity fine-tuning process, we first analyze the optical modes in the DFB structures, base on which the fine-tuning process can be determined by an angle-resolved PL spectra (ARPS) characterization or the spatial pattern of the amplified-spontaneous-emission (ASE) diffraction. Based on this methodology, we greatly reduced the workload to achieve an optimal overlap of the resonant wavelength with the gain spectrum, leading to an optimized laser performance at 530 nm with a threshold of 20 $\mu J\ cm^{-2}$ and a linewidth of 0.85 nm.

4.3 Fabrications of perovskite DFB cavities

4.3.1 Nanoimprint on perovskite films

Perovskite DFB cavities are fabricated by nanoimprint lithography as illustrated in **Figure 4.1a**: (i) a solution of $MAPbBr_3$ precursor using dimethyl sulfoxide (DMSO) as a solvent is spin-coated on a glass substrate, forming a precursor film where the perovskite crystallization is not yet completed due to the presence of the residual solvent; (ii) a nanopatterned PDMS mold is subsequently placed on top of the precursor film while the sample is heated at 80 ℃ to complete the crystallization under the constraining of the mold, thereby forming a grating; and (iii) upon complete crystallization, the PDMS mold is peeled off, leaving a nanopatterned crystalline perovskite film. More details of the fabrication procedures can be found in the experimental section.

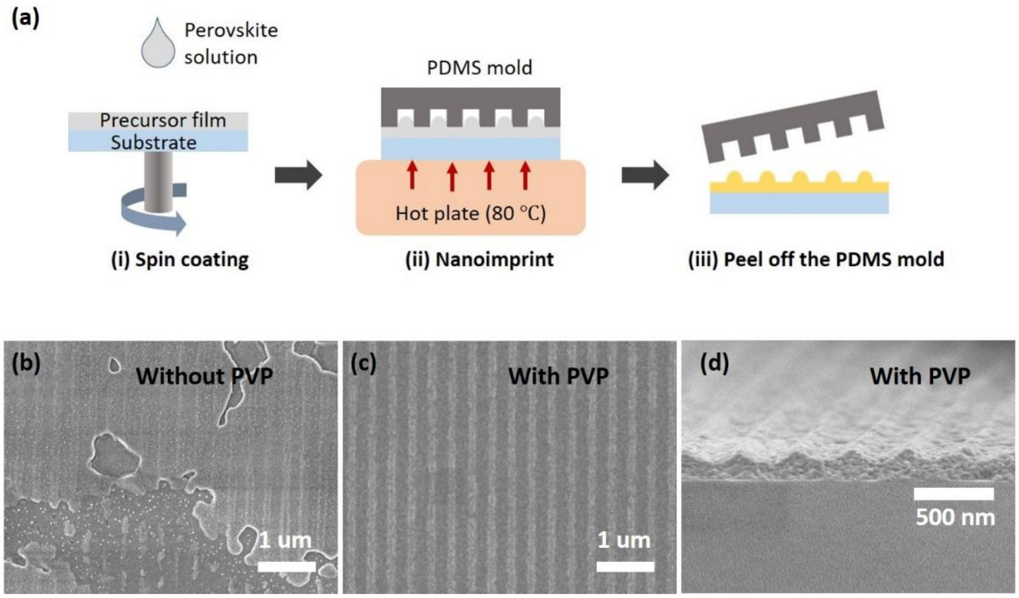

Figure 4.1 (a) Schematic diagram showing the procedures of fabricating the perovskite DFB cavities. Top SEM images of nanopatterned perovskite films without (b) and with (c) 20% of PVP. (d) Cross-section SEM image of nanopatterned perovskite film with 20% of PVP. The grating period in all the SEM images here is 320 nm.

As mentioned previously, the crystal growth of perovskite during the nanoimprint process is difficult to control, thus leading to a poor morphology, as shown in **Figure 4.1b**, where the perovskite film is not continuous with disconnected domains and defective grating. To improve the film quality during the nanoimprint process, a polymer Polyvinylpyrrolidone (PVP) is added to the precursor solution (mass ratio of PVP/$PbBr_2$ is 20%). From the results shown in **Figure 4.1c&d**, the perovskite film shows a much better morphology as manifested by closely packed perovskite nanocrystals and a well-shaped grating. In addition, the spin coating duration is also found to be critical to the success of the subsequent nanoimprint. As can be seen from **Figure 4.2**, with 20% of PVP, the spin coating duration should be around 20 s to obtain a good-quality grating. Shorter (15 s) or longer (30 s) spin coating duration both result in a poor-quality grating.

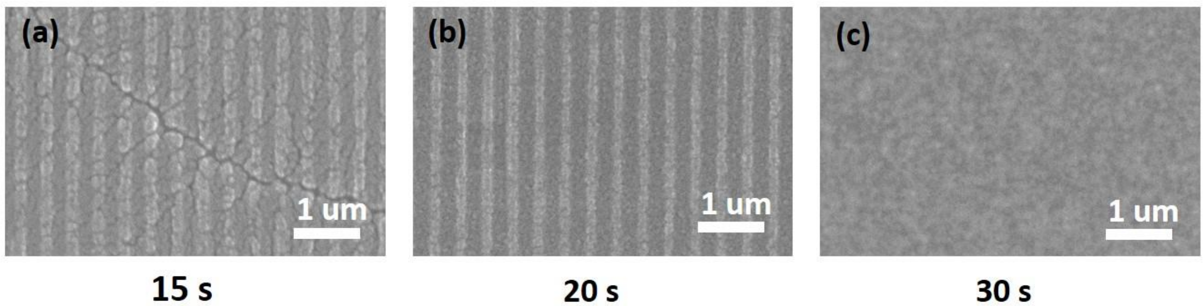

Figure 4.2. Nanopatterned perovskite films fabricated by adding 20% of PVP with different spin coating durations: (a) 15 s; (b) 20 s; (c) 30 s. The grating period is 320 nm.

4.3.2 Film formation dynamics

To understand the role of PVP and the crystallization kinetics duration the nanoimprint process, in-situ absorption measurements are conducted to monitor the film formation dynamics,[21] where the time evolutions of the absorbance spectra with different PVP ratios (mass ratio of PVP/$PbBr_2$) are recorded during spin coating. The in-situ absorption data of the precursor solution with different PVP ratios are shown in **Figure 4.3**. From the results, for all the PVP ratios, 3 phases can be identified: (i) a solution phase with an absorption peak at 305 nm; (ii) an intermediate phase with a peak at 320 nm; (iii) a perovskite phase with a broad absorption spectrum. As shown in the data, as soon as the spin coating starts, the absorbance mainly comes from the solution, as indicated by the 305 nm peak which decreases quickly in the very beginning, corresponding to the solution volume shrinkage. As the spin coating continues, the peak shifts from 305 nm to 320 nm due to the formation of a $PbBr_2$-MABr-DMSO complex (intermediate phase) due to the evaporation of the residual solvent.[22] Finally, perovskite crystals start to form and grow as the residual solvent further evaporates, leading to a broad absorbance spectrum.

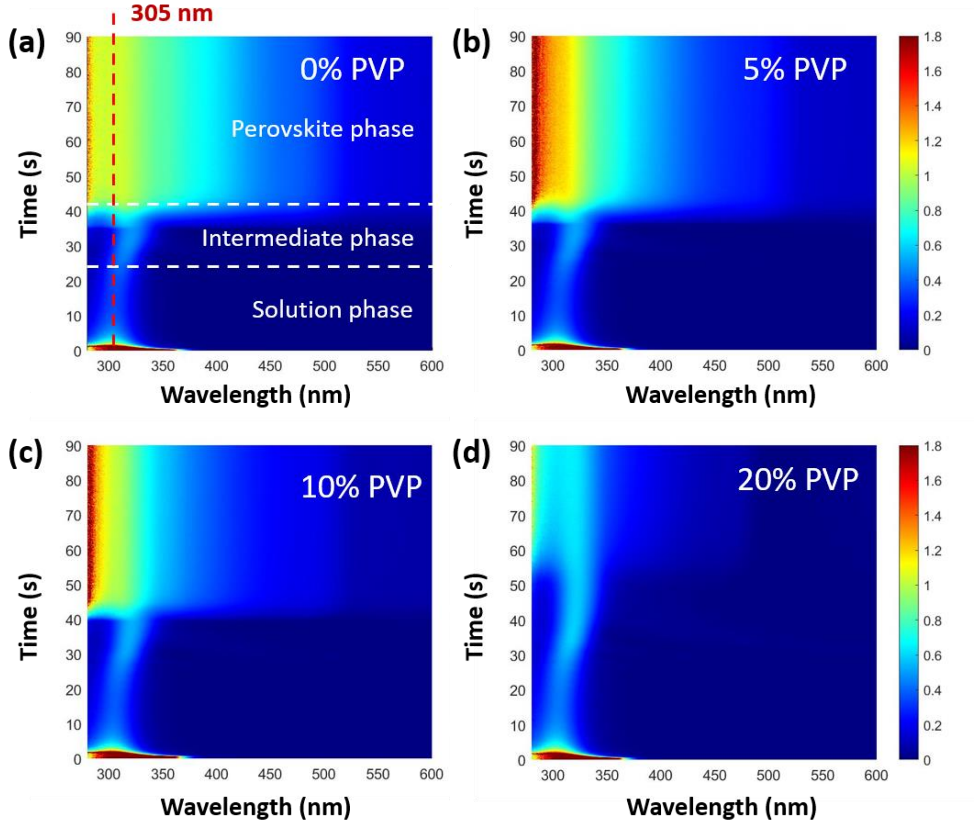

Figure 4.3 2D plot of the in-situ absorption during the spin coating of the perovskite solution with different PVP ratios: (a) 0%; (b) 5%; (c) 10%; (d) 20%. The colormap indicates absorbance.

To gain a better perspective on the film formation dynamics, the absorbance at 305 nm versus time is plotted in **Figure 4.4**, showing the time evolution of the disappearance and formation of different phases. From the figure, with the increase of the PVP ratio, not only the transition to the intermediate phase is delayed, but also the amount of solution before the transition is increased. These results indicate that PVP can slow down the evaporation of the solvent and maintain a larger amount of the solution, thereby enabling the formation of a soft and stable precursor film that can be readily nanoimprinted.[18] In addition, for the 20% PVP case, the transition to the intermediate phase occurs at 25th second, which explains why the spin coating duration should be around 20 s (**Figure 4.2**): at the 15th second, the 305 nm peak has not yet reached a plateau before the transition to the intermediate phase, indicating the precursor film is not yet stable for the subsequent nanoimprint, leading to cracks (**Figure 4.2a**); at the 30th second, the precursor film already reaches the intermediate phase that is not soft enough to be nanoimprinted (**Figure 4.2c**).

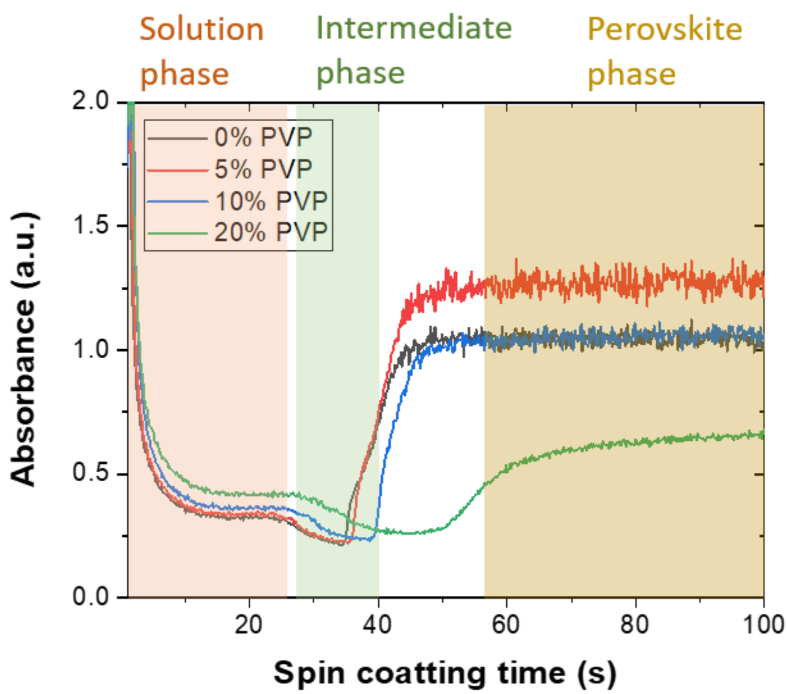

Figure 4.4 In-situ absorbance of perovskite solutions at 305 nm with different PVP ratios (0%, 5%, 10% and 20%).

4.3.3 Photophysical studies

In addition to facilitate the nanoimprint process, the effects of PVP on the threshold of the ASE of the perovskites are also investigated since it is the most important parameter to evaluate a gain material. To investigate the intrinsic optical properties of the perovskite films due to the effects of PVP, planar perovskite films with and without PVP (20%) are fabricated by the same procedure using a planar PDMS mold. ASE measurements were carried out for these planar perovskite films by a femtosecond pulsed laser at 400 nm. We found that the perovskite film without PVP does not show ASE even at a very high energy fluence (185 µJ cm^{-2}), while the film with PVP shows ASE at 531.3 nm with a threshold of 37 µJ cm^{-2} (**Figure 4.5**).

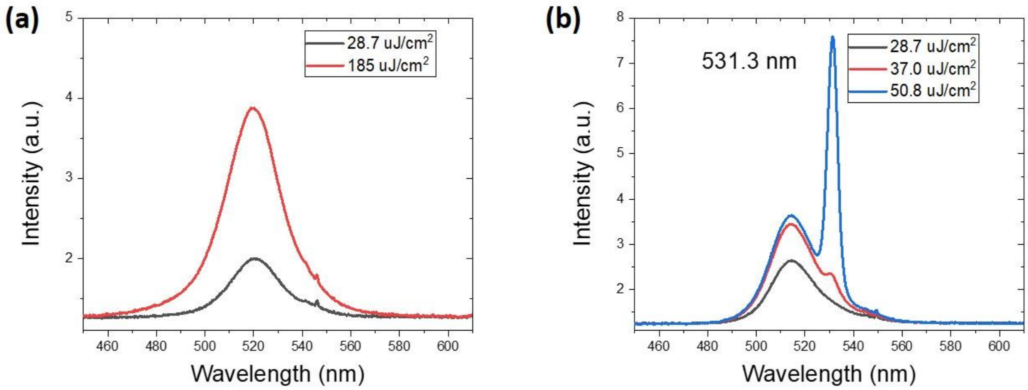

Figure 4.5 (a) Emission spectra of a planar perovskite film without PVP; no ASE is observed even at a high excitation fluence (185 µJ/cm^2). (b) Emission spectra of a planar perovskite film with 20% of PVP; ASE peak starts to appear at an excitation fluence of 37.0 µJ/cm^2.

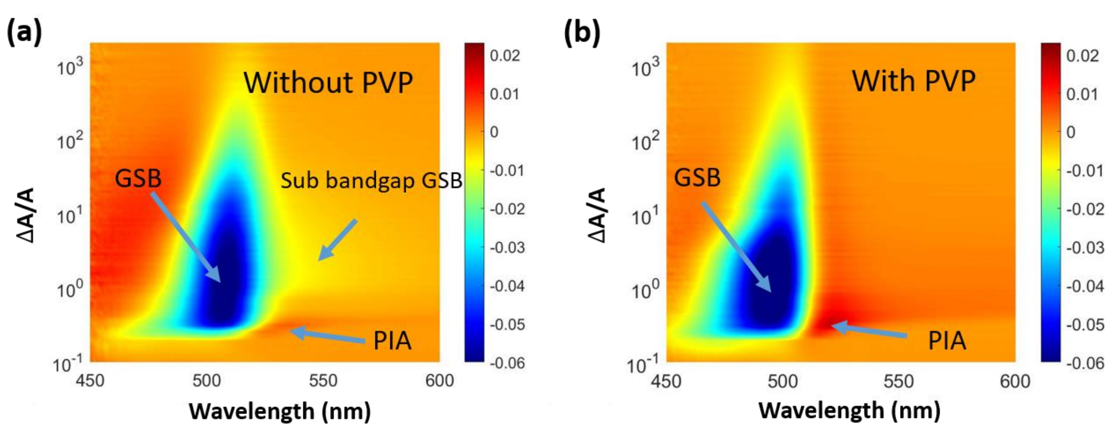

Figure 4.6 Transient absorption of planar perovskite films fabricated without (c) and with (d) 20% of PVP; GSB is ground state bleaching; PIA is photo-induced absorption.

To understand the mechanism behind the effect of PVP on the ASE performance, transient absorption (TA) measurements are conducted on planar perovskite films to probe the charge carrier dynamics using a pumping fluence of 53 μJ cm^{-2} which is above the ASE threshold of the perovskite film with PVP, and the results are shown in **Figure 4.6**. Here, ground state bleaching (GSB) due to band-to-band transition is observed in both films. For the film without PVP (**Figure 4.6a**), photo-induced absorption (PIA) is observed at 530 nm during the initial 0.5 ps, thereafter quickly followed by a broad sub-bandgap GSB. The initial PIA comes from the excited charge carriers in the conduction band, while the sub-bandgap GSB comes from the occupancy of the sub-bandgap defect states by the photo-excited carriers. Such a quick transition from the initial PIA to the sub-bandgap GSB during the first 1 ps indicates a rapid loss of excited carriers from the conduction band to the defect states, instead of accumulating carriers in the conduction band for population inversion, and this is the reason why ASE cannot be observed. For the film with PVP (**Figure 4.6b**), a strong PIA at 520 nm is observed, and sub-bandgap GSB was not observed, leading to accumulation of excited carriers in the conduction band for population inversion and hence ASE with a relatively moderate threshold. It has also been reported that PVP can passivate the grain boundary and surface defects of perovskites.[23,24] Therefore, in this work, the improved ASE performance by adding PVP can be attributed the reduced grain boundary defects by PVP passivation. This is further supported by transient PL measurements (**Figure 4.7**), where the PL lifetime is significantly extended with addition of PVP into the perovskite film.

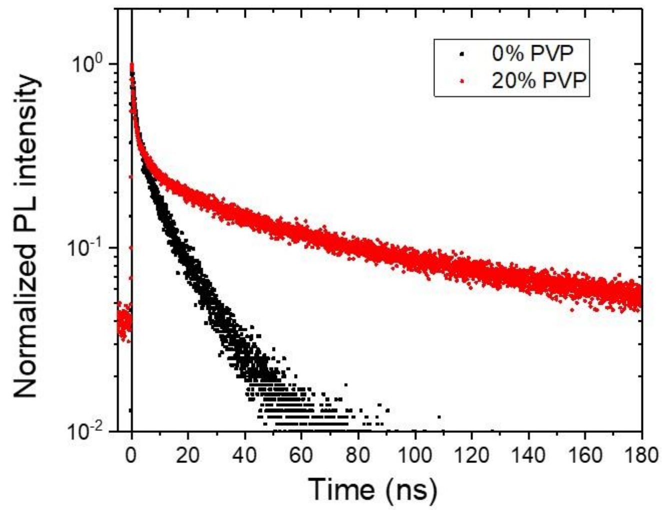

Figure 4.7. Transient PL of planar perovskite films with 20% of PVP and without PVP.

4.4 Fundamentals of DFB Cavity Fine-Tuning

Although a facile approach of fabricating perovskite DFB cavities has been established in this work, fine-tuning the cavity for an optimal overlap of the resonant wavelength (λ_R) with the gain spectrum is also crucial to realize an optimized laser performance. The gain spectrum can be estimated from the ASE spectrum with a peak wavelength (λ_{ASE}) corresponding to the gain maximum at 531 nm from **Figure 4.5b**. Since the gain spectrum is an intrinsic property of the gain material, the cavity fine-tuning is realized by manipulating λ_R by tuning the cavity to match with λ_{ASE}.[25] However, in many cases, the exact value of λ_R is unknown. As mentioned previously, to reduce the amount of effort of fine-tuning a cavity, it is critical to determine the fine-tuning direction, such that the tuning process is conducted in a guided way. Here, we introduce a systematic approach to determine to fine-tuning direction, which consists of the analysis and characterizations of optical modes in DFB lasers.

4.4.1 Optical modes in DFB structures

We first analyze the optical modes in perovskite thin films and how they interact with the DFB structures. In a planar perovskite thin film, due to the larger refractive index of the perovskite than its surrounding air, the propagation of light undergoes total internal reflection when the propagation angle is larger than the critical angle. In other words, only light with an in-plane wavevector (**k**) less than the wavevector in the air ($\mathbf{k}_0$) can be outcoupled, forming air modes. Light with a larger **k** value is trapped inside the perovskite film forming waveguide modes.

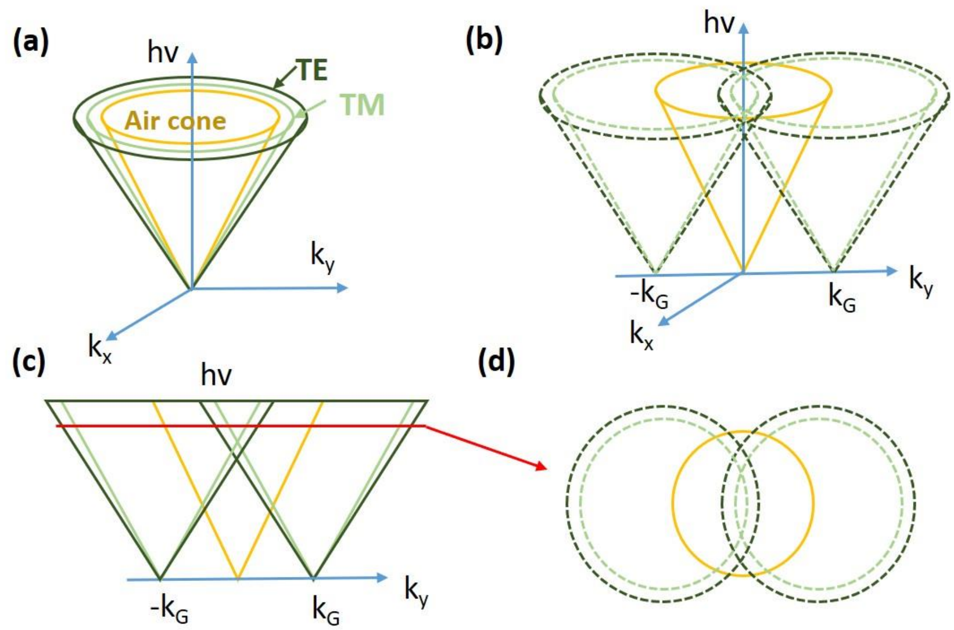

Figure 4.8 Schematic diagrams showing the light outcoupling physics in a DFB structure: (a) mode distribution of a planar thin film in the hν-$k_{//}$ space; (b) mode distribution of a nanopatterned thin film in the hν-$k_{//}$ space; **(c)** cross section of (b) along hν-k_y plane at $h\nu_{ASE}$; (d) cross section of (b) along k_x-k_y plane with hν larger than the TM mode cross point.

We illustrate the dispersion of the optical modes in an energy-momentum space, where the z-axis is the photon energy (hν) and the x-y plane corresponds to **k** (**Figure 4.8a**).[26] From the diagram, the air mode forms a solid cone which defines the dispersion of the outcoupled light, while the transverse electric (TE) and transverse magnetic (TM) waveguide modes (WG) form hollow cones. Because the perovskite film is isotropic in the x-y plane, the optical modes are all concentric circles with different radii: air < TM WG < TE WG. The radii of the waveguide cones are large than that of the air cone because the waveguide modes are trapped inside the planar perovskite film. When a grating structure is introduced to the perovskite film, the trapped waveguide modes are diffracted, and the in-plane wavevector of the diffracted waveguide modes become $\mathbf{k}_{WG}'(\lambda) = \mathbf{k}_{WG}(\lambda) \pm m \cdot \mathbf{k}_G$, where m is the diffraction order and $\mathbf{k}_G = 2\pi/\Lambda$ is the grating wavevector. In the mode dispersion plot, this is represented by a shift of the waveguide cones by $\pm m \cdot \mathbf{k}_G$ leading to partial overlaps between the diffracted waveguide modes and the air cone (**Figure 4.8b**).[26]

For a surface-emitting DFB laser, the grating is responsible for both the cavity resonance and surface emission, and the resonant wavelength is determined by the equation below:

$$\mathbf{k}_{WG}(\lambda_R) = \mathbf{k}_G \qquad (4.1)$$

This equation governs the second order diffraction to be $\mathbf{k}_{WG}'(\lambda_R) = \mathbf{k}_{WG}(\lambda_R) - 2 \cdot \mathbf{k}_G = -\mathbf{k}_{WG}(\lambda_R)$, therefore the grating provides the optical feedback to revert the waveguide mode propagation direction, which forms a resonance in the x-y plane normal to the grating grooves. Equation (4.1) also results in the first order diffraction to be $\mathbf{k}_{WG}'(\lambda_R) = \mathbf{k}_{WG}(\lambda_R) - \mathbf{k}_G = 0$, therefore the resonance mode is diffracted towards the z-axis. Below the lasing threshold, multiple waveguide modes across a broad range of wavelength are present. Above the lasing threshold, given λ_R in the gain spectrum, the resonance mode is amplified by stimulated emission thereby suppressing the other modes, leading to surface-emitting lasing at λ_R.

Based on the understanding of the optical modes in the DFB structure, here we introduce two approaches to guide the cavity fine-tuning process. The first approach aims at directly determining λ_R below the ASE or laser threshold by measuring the angle-resolved PL spectra (ARPS), while the second approach uses the spatial pattern of the waveguide emission above the ASE or laser threshold to determine the fine-tuning direction.

4.4.2 Angle-resolved PL spectra

In angle-resolved PL spectra (ARPS) measurements, the PL spectra of the perovskite film are measured at different angles (**Figure 4.9a)**, generating a 2D mode dispersion plot with the vertical axis being the photon energy converted from the emission wavelength, and the horizontal axis being the in-plane wavevector converted from the measurement angle. More details of the characterization can be found in the experimental section. From **Figure 4.8b**, the first order diffraction of the grating shifts the waveguide cones in the hν-k space by a vector of $\mathbf{k}_G$. When we measure the ARPS normal to the grating grooves (along $\mathbf{k}_G$), the 3D mode dispersion along the k_y axis is shifted by $\mathbf{k}_G$ in the hν-k_y plane and falls within the air cone. Hence, the WG mode can be extracted as two pairs of crossed stripes within the air cone, from which λ_R can be determined as the wavelength corresponding to the cross point (**Figure 4.8c**).[27] Note that both the TM and TE waveguide modes can be present in the mode dispersion, therefore we can use a polarizer in the ARPS measurements to differentiate them.

To illustrate the approach above, we first measure the mode dispersion of a nanopatterned perovskite film using ARPS. From the plot, two pairs of crossed stripes are observed, which is consistent with the measurements illustrated in **Figure 4.9b**. We infer that the upper crossed stripes are the TM WG modes, while the lower crossed stripes are the TE WG modes, which is confirmed by inserting a polarizer in the ARPS setup. Based on the cross point of the TE WG modes, we can determine that λ_R is 570 nm (2.18 eV),[27] which is far away from the ASE peak of 531 nm (2.34 eV). Therefore, to achieve an optimized laser performance, cavity fine-tuning should be conducted to reduce λ_R.

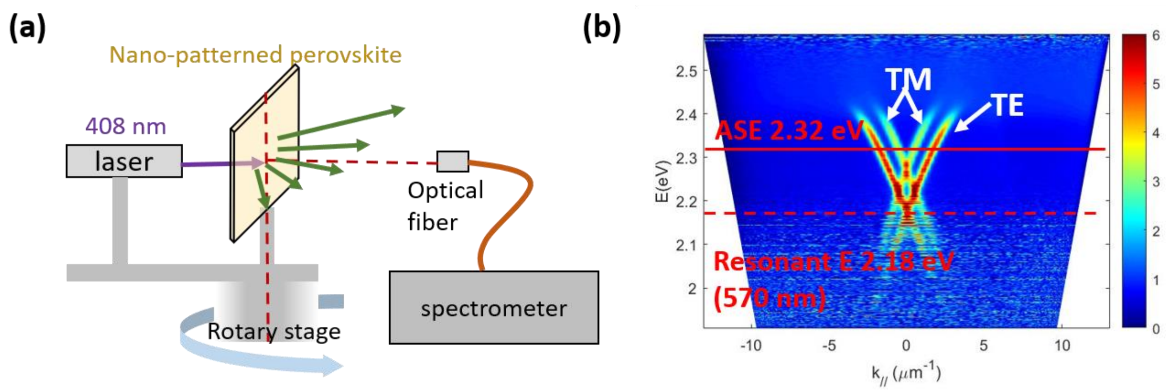

Figure 4.9 (a) Schematic diagram showing the setup of the ARPS characterization. (b) ARPS plot of a nanopatterned perovskite.

4.4.3 Diffraction pattern of ASE

The spatial pattern of ASE emission is another approach to determine the fine-tuning direction, which relies on an understanding of the ASE diffraction pattern within the context of the optical mode analysis in **Figure 4.8**. As described previously, the difficulty of cavity fine-tuning occurs when λ_R is out of the gain spectrum such that the waveguide modes at λ_R cannot be amplified, leading to the failure of laser emission, from which λ_R cannot be determined. Meanwhile, the waveguide modes at λ_{ASE} are amplified resulting in ASE emission. Because the ASE peak is much stronger than the other wavelengths, the spatial pattern of the extracted waveguide modes at λ_{ASE} stands out from the background, which can be visualized by cutting the 3D mode dispersion (**Figure 4.8b**) along the k_x-k_y plane at the ASE photon energy ($h\nu_{ASE}$) (**Figures 4.8d**). To illustrate this, consider the spatial patterns projected on a flat surface at a distance of d (**Figure 4.10**). Each point in the k_x-k_y plane corresponds to a point on the flat surface (x, y) based on (k_x, k_y) = (k_0 sinθ cosϕ, k_0 sinθ sinϕ) and (x, y) = (d tanθ cosϕ, d tanθ sinϕ), where θ is the polar angle relative to the substrate normal direction, ϕ is the azimuthal angle in the x-y plane. At small angles θ, (x, y) = (d·k_x/k_0, d·k_y/k_0), indicating the spatial pattern resembles the mode dispersion in the k_x-k_y plane.

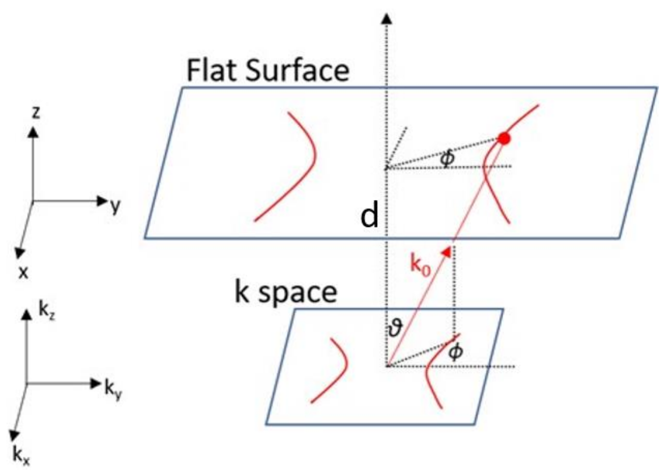

Figure 4.10 Schematic diagram showing the spatial pattern in the x-y plane resembles the mode dispersion in the k_x-k_y plane.

Based on the illustration above, we can easily determine the fine-tuning direction when λ_R is out of the gain spectrum. Remember that λ_R is located at the cross point of the TE WG modes in the hν-k_y plane (**Figure 4.8c**). If λ_R is on the longer side of the gain spectrum (hν_R < hν_{ASE}), then the ASE diffraction pattern is manifested by crossed arcs in the k_x-k_y plane (**Figure 4.11a**); if λ_R is on the shorter side of the gain spectrum (hν_R < hν_{ASE}), then the ASE diffraction pattern is manifested by separated arcs in the k_x-k_y plane (**Figure 4.11c**). When λ_R is within the gain spectrum, the spatial pattern is laser emission, which is formed by just touching of the TE waveguide arcs (**Figure 4.11b**).

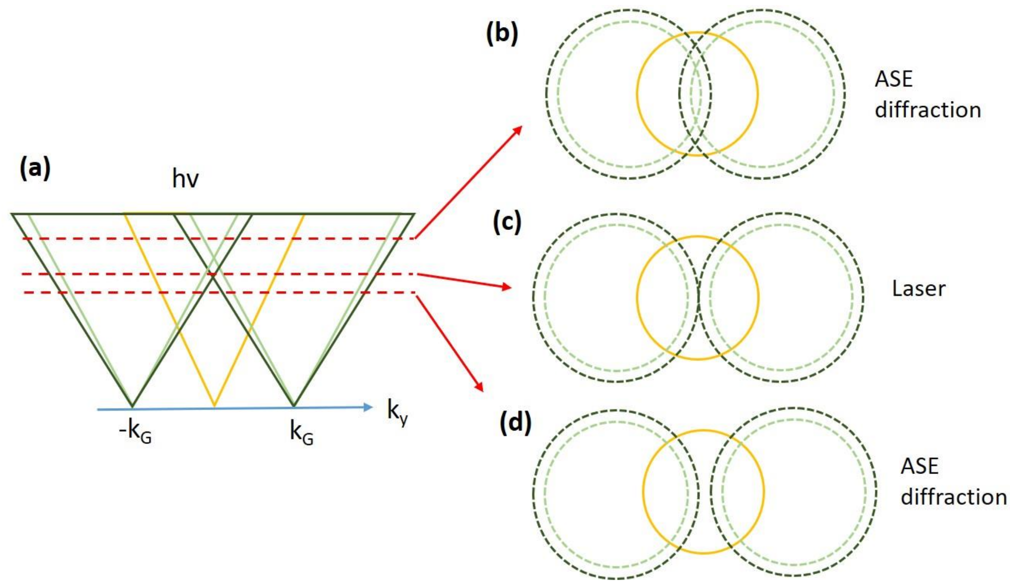

Figure 4.11. (a) Mode dispersion in hν-ky plane. Cut of the 3D mode dispersion along k_x-k_y plane (b) when λ_R is on the longer side of the gain spectrum ($h\nu_{resonant} < h\nu_{ASE}$), (c) when λ_R is within the gain spectrum, (d) when λ_R is on the shorter side of the gain spectrum ($h\nu_{resonant} > h\nu_{ASE}$)

4.5 Results of DFB cavity fine-tuning

Based on the optical analysis and the ARPS characterization, we now introduce an effective and systematic strategy to fine-tune the perovskite DFB cavities. First, instead of changing Λ that can lead to a heavy workload as discussed previously, here we change the effective refractive index (n_{eff}) through changing the thickness of the perovskite film. It has been reported that n_{eff} decreases as the film thickness is reduced, indicating that the resonant wavelength also decreases as the film thickness is reduced.[25,28] In this work, the film thickness is manipulated by varying the concentration of the precursor solutions. Second, the ARPS characterization is used to determine the resonant wavelength that is compared with the ASE wavelength, so that the direction of cavity fine-tuning can be determined.

To demonstrate the fine-tuning of the cavity, we first fabricate perovskite films having a DFB structure (Λ=320 nm) using different solution concentrations (mass of $PbBr_2$ in DMSO). The films are then subjected to both laser and ARPS characterizations with results summarized in **Figure 4.12**. In all ARPS plots, we can clearly identify the crossed upper TM mode stripes and the lower TE mode stripes, from which the resonant photon energy (wavelength) in each condition is also determined. In addition, the ASE photon energy (2.34 eV corresponding to 531 nm) is labeled for comparison. For the concentration of 180 mg/mL, the resonant phonon energy is still smaller than the ASE phonon energy, leading to a diffraction of ASE. In this case, the TE mode arcs in the diffraction pattern are crossed. Therefore, the concentration needs to be further reduced to increase the resonant photon energy. When the concentration is reduced to 150 mg/mL, the resonant photon energy is further shifted upward, which is almost perfectly matched with the ASE photon energy, leading to successful laser emission. In this case, the TE mode arcs just touch with each other, forming a single bright stripe in the middle.[1,29] Up to this point, the cavity is already successfully fine-tuned, and 150 mg/mL has been identified as the optimized concentration. Further reduction of the film concentration to 120 mg/mL results in a resonant photon energy much larger than the ASE photon energy. In this case, the TE mode arcs are separated from each other, and only ASE diffraction instead of laser emission is observed. As can be seen from these data, all the ARPS plots are consistent with their corresponding photos of the emission patterns, confirming the validity of the two characterization approaches.

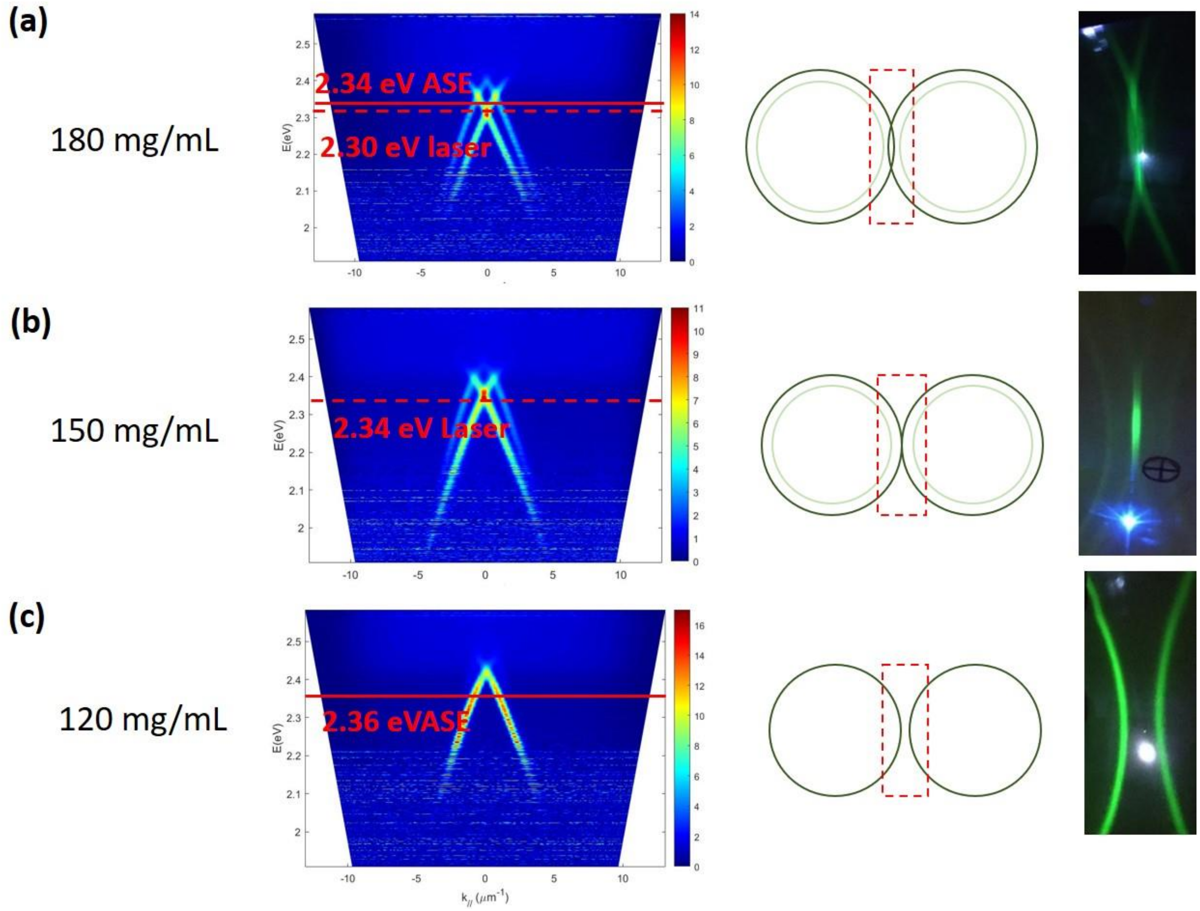

Figure 4.12. ARPS plots and diffraction patterns of nanopatterned perovskites fabricated with different concentrations.

To better understand the importance of cavity fine-tuning for perovskite DFB lasers, the laser performance with different solution concentrations is summarized in **Figure 4.13**. From **Figure 4.13a**, we can clearly observe the change of the resonant wavelength with the solution concentration, and 150 mg/mL gives a resonant wavelength located at the gain maximum. From **Figure 4.13b**, both the threshold and the FWHM reach to the lowest values when the resonant wavelength is located at the gain maximum of the perovskites, while a 10% deviation from the optimal concentration can lead to two times higher lasing threshold. The laser performance of the optimized concentration (150 mg/mL) is shown in Figure **4.13c&d**. From the data, the threshold of the optimized perovskite DFB laser is 20 μJ cm^{-2} with a FWHM of 0.86 nm. Therefore, cavity fine-tuning for an optimal overlap of the gain spectrum with the resonant wavelength is critical to achieve an optimized performance in perovskite DFB lasers.

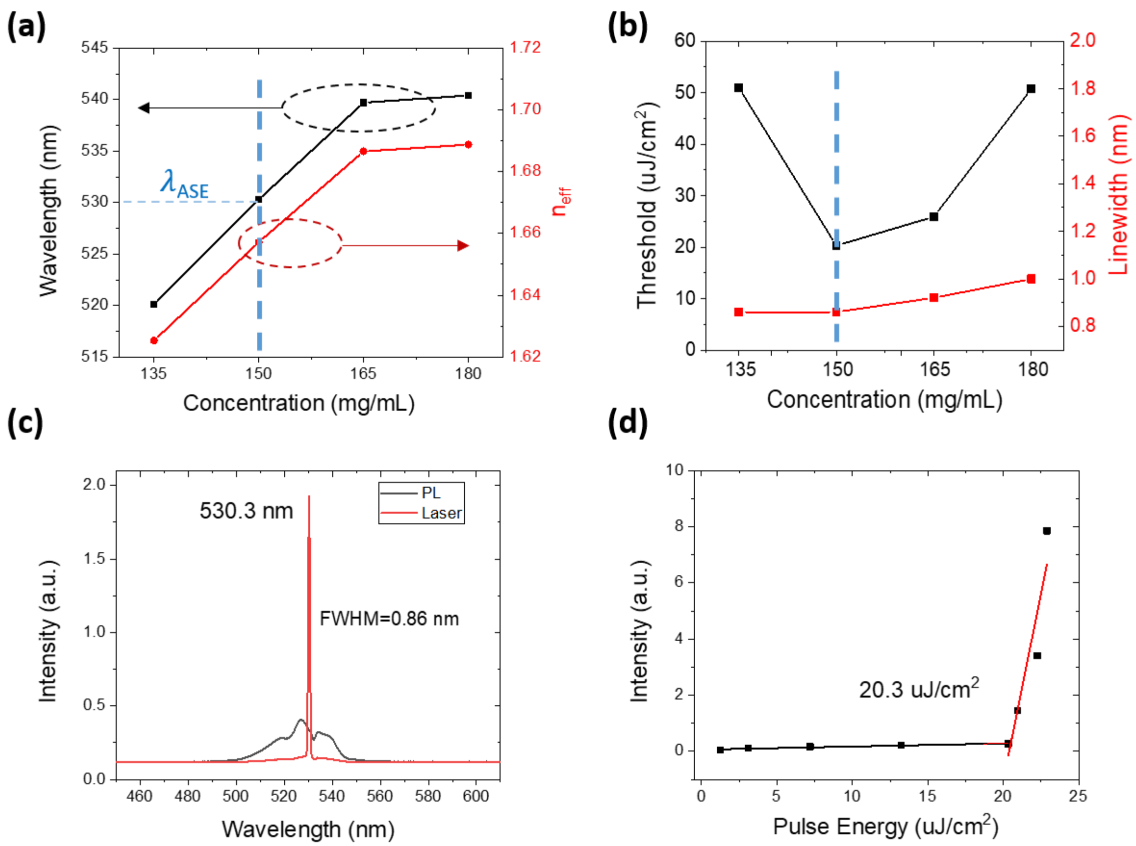

Figure 4.13 (a) correlation between resonant wavelength, effective index, and the solution concentration. (b) Summary of the threshold and linewidth of perovskite DFB lasers fabricated with different concentrations. (c) Emission spectra of the 150 mg/mL sample below and above the laser threshold. (d) Threshold curve of the 150 mg/mL sample.

4.6 Conclusion

In this work, a facile and systematic methodology has been demonstrated with metal-halide perovskites for fine-tuning the cavity of solution-processed surface-emitting DFB lasers. To simplify the cavity-fabrication, a polymer polyvinylpyrrolidone (PVP) is added in the perovskite precursor solutions to assist direct nanoimprint. Through in-situ absorption measurements, PVP has been found to maintain the amount of solution after spin coating, enabling the formation of a stable and soft precursor film that is ready for straightforward nanoimprint to form well-shaped gratings. Through transient absorption spectroscopy, PVP has been found to reduce the defect density in the perovskite film, promoting the ASE performance. To accelerate the cavity fine-tuning, a systematic analysis of the optical modes in the DFB structures is introduced. Through the ARPS measurements, the resonant wavelength can be determined, which can accelerate the cavity fine-tuning process. In addition, the spatial pattern of the ASE diffraction can also be used for guiding the cavity fine-tuning direction. Lastly, based on the methodology, an optimized laser performance with 20 μJ cm^{-2} threshold and 0.86 nm FWHM has been achieved with largely reduced efforts.

4.7 Methods

Preparation of Perovskite Precursor Solutions

Lead bromide ($PbBr_2$) (99.999% trace metals basis), Polyvinylpyrrolidone (PVP), and (dimethyl sulfoxide) (DMSO) (anhydrous ≥ 99.9%) are purchased from Sigma Aldrich, while methylammonium bromide (MABr) is purchased from Dyesol. The perovskite precursor solutions are prepared by dissolving $PbBr_2$, MABr and PVP into DMSO, where the molar ratio of MABr to $PbBr_2$ is 1.5: 1.0, and the mass ratio of PVP to $PbBr_2$ is varied with 0%, 5%, 10% and 20% for studying the effects of PVP on the film formation dynamics. The concentration of the solutions is varied to manipulate the perovskite film thickness for fine-tuning the DFB cavities. The concentration is indicated by the mass concentration of $PbBr_2$ in DMSO, ranging from 120 mg/mL to 180 mg/mL with a step of 15 mg/mL. After mixing the solutes with the solvent, the precursors are stirred at 70 ℃ for 1 hour for a complete dissolution before use.

Fabrication of Perovskite Films

The nanopatterned perovskite films are fabricated by a direct nanoimprint method (**Figure 4.1a**). First, a precursor film is formed by spin coating the precursor solution on a cleaned glass substate (cleaned by acetone and isopropanol sequentially in an ultrasonic bath). The spin coating speed is 4000 rpm, and the spin coating time is tuned from 15 s to 20 s to achieve the best status of the precursor film for the subsequent nanoimprint. Second, a nanopatterned polydimethylsiloxane (PDMS) mold is placed on the precursor film, and the sample is subjected to thermal annealing at 70 ℃ for 10 min to complete the perovskite crystal growth. The nanopattern of the PDMS mold is replicated from a silicon master mold fabricated by interference lithography, which is an 1D grating with a period of 320 nm. Third, after the thermal annealing, the PDMS mold is peeled off, leaving the nanopatterned perovskite film ready for characterizations. To maintain the same material properties while excluding the effects of grating on optical characterizations, the planar perovskite films that are used for photophysical studies (transient absorption, transient PL and ASE measurements) are fabricated with the same procedures described above except that the PDMS mold is planar, which is replicated from a planar glass substrate.

Scanning Electron Microscope

Scanning electron Microscope (SEM) is conducted by a Field Emission Scanning Electron Microscope (FEI Verios 460L).

In-Situ Absorption Spectroscopy

The in situ UV-Vis transmittance measurements are conducted using a home-built setup similar to the previous studies.[30] Filmetrics F20-UVX spectrometer with a deuterium-tungsten light source (Filmetrics, Inc.) are used. Measurements are performed inside a nitrogen filled glovebox with H_2O and O_2 levels below 0.1 ppm and all the measurements are done on bare glass substrates. Transmittance spectra are collected at a repetition rate of 10 Hz and an integration time of 100 ms. Transmittance is converted to absorbance using the relation $A = 2-\log_{10}(T)$, where T represents the transmittance.

Ultrafast transient absorption (UFTA) spectroscopy

Transient absorption (TA) measurements are performed using an amplified Ti:sapphire laser system. Portion of the output from a 1 kHz Ti:sapphire Coherent Libra regenerative amplifier (4 mJ, 100 fs (fwhm) at 800 nm) is split into the pump and probe beams. The pump beam is directed into an optical parametric amplifier (Coherent OPerA Solo) to generate the 400 nm pump pulse while the probe beam is delayed in a 6.6 ns optical delay stage. The probe beam is focused into a CaF_2 crystal to generate the white light continuum spanning 400–700 nm. The two beams are focused and overlapped into a spot on the sample. The transient spectra and kinetics are obtained using a commercially available transient absorption spectrometer (Helios, Ultrafast Systems). All the perovskite samples subjected to the characterizations are encapsulated with a cover glass and an UV-curable epoxy.

Time-Correlated Single Photon Counting Spectroscopy

Time-resolved PL decays are measured using a time-correlated single photon counting spectrometer from Edinburgh Instruments (LifeSpec II). Chameleon Ultra II Ti:Sapphire oscillator (Coherent) is used as the light source, generating 140 fs pulses with a repetition rate of 80 MHz. The laser is tuned to 800 nm and directed into a Coherent 9200 Pulse Picker to give a 4 MHz repetition rate for the experiments. Finally, the 400 nm excitation pulse used in these experiments is obtained by frequency doubling (SHG HarmoniXX, A.P.E.) output from Chameleon Ultra.

ASE and Lasing Characterizations

ASE and lasing characterizations are both conducted by exciting the perovskite samples with a 150 fs pulsed laser (400 nm, 1 kHz) and recording the spectra of the light emission in the normal direction through a CCD spectrometer (from Mightex) at different excitation fluences. The pulsed laser is obtained through the second harmonic generation of a 150 fs pulsed laser (800 nm, 1 kHz) from Quantronix Ingetra-C laser system. The laser beam size on the sample is around 2 mm in diameter. All the perovskite samples for the characterizations are encapsulated. To obtain the diffraction patterns, a piece of white paper is put in the front of the excited perovskite samples, with projection patterns recorded by photos.

ARPS Characterization

ARPS characterization is conducted by measuring the PL spectra of the perovskite samples at different viewing angles (**Figure 4.9a**). Specifically, the nanopatterned perovskite sample is fixed on a rotary stage, with the grating orientation along the vertical direction. A continuous wave laser beam (408 nm) that is generated from a laser diode fixed on the rotary stage is used to excite the perovskite sample from the glass side. The terminal of an optical fiber connected to a spectrometer is fixed at the front side of the sample to record the PL spectra, with its height being the same as the excitation spot on the sample. In addition, the excitation spot is within the rotation axis, so that its relative distance with the optical fiber terminal is kept constant during the rotation. When the sample is normal to the line connecting the excitation spot and the optical fiber terminal, the angle is defined as zero; when the sample is parallel with this line, the angle is defined as $\pm$ 90 °. By recording the PL spectra at different angles with a step of 1 °, the ARPS data with angle from -90 ° to 90 ° and wavelength from 400 nm to 700 nm are obtained, from which the $h\nu$-$k_{//}$ plots are generated.

REFRENCES

[1] I. D. W. D. W. W. Samuel, G. A. A. Turnbull, Organic Semiconductor Lasers, *Chem. Rev.* **2007**, 107, 1272–1295.

[2] K. Roh, C. Dang, J. Lee, S. Chen, J. S. Steckel, S. Coe-Sullivan, A. Nurmikko, Surface-Emitting Red, Green, and Blue Colloidal Quantum Dot Distributed Feedback Lasers, *Opt. Express* **2014**, 22, 18800.

[3] M. M. Stylianakis, T. Maksudov, A. Panagiotopoulos, G. Kakavelakis, K. Petridis, Inorganic and Hybrid Perovskite Based Laser Devices: A Review, *Materials (Basel).* **2019**, 16, 859.

[4] M. Saliba, S. M. Wood, J. B. Patel, P. K. Nayak, J. Huang, J. A. Alexander-Webber, B. Wenger, S. D. Stranks, M. T. Hörantner, J. T. Wang, R. J. Nicholas, L. M. Herz, M. B. Johnston, S. M. Morris, H. J. Snaith, M. K. Riede, Structured Organic-Inorganic Perovskite toward a Distributed Feedback Laser, *Adv. Mater.* **2016**, 28, 923–929.

[5] L. Protesescu, S. Yakunin, M. I. Bodnarchuk, F. Krieg, R. Caputo, C. H. Hendon, R. X. Yang, A. Walsh, M. V. Kovalenko, Nanocrystals of Cesium Lead Halide Perovskites (CsPbX3, X = Cl, Br, and I): Novel Optoelectronic Materials Showing Bright Emission with Wide Color Gamut, *Nano Lett.* **2015**, 15, 3692–3696.

[6] E. T. Hoke, D. J. Slotcavage, E. R. Dohner, A. R. Bowring, H. I. Karunadasa, M. D. McGehee, Reversible Photo-Induced Trap Formation in Mixed-Halide Hybrid Perovskites for Photovoltaics, *Chem. Sci.* **2015**, 6, 613–617.

[7] K. X. Steirer, P. Schulz, G. Teeter, V. Stevanovic, M. Yang, K. Zhu, J. J. Berry, Defect Tolerance in Methylammonium Lead Triiodide Perovskite, *ACS Energy Lett.* **2016**, 1, 360–366.

[8] W.-J. Yin, T. Shi, Y. Yan, Unusual Defect Physics in CH 3 NH 3 PbI 3 Perovskite Solar Cell Absorber, *Appl. Phys. Lett.* **2014**, 104, 063903.

[9] D. P. McMeekin, G. Sadoughi, W. Rehman, G. E. Eperon, M. Saliba, M. T. Hörantner, A.

Haghighirad, N. Sakai, L. Korte, B. Rech, M. B. Johnston, L. M. Herz, H. J. Snaith, M. T. Horantner, A. Haghighirad, N. Sakai, L. Korte, B. Rech, M. B. Johnston, L. M. Herz, H. J. Snaith, A Mixed-Cation Lead Mixed-Halide Perovskite Absorber for Tandem Solar Cells, *Science (80-.).* **2016**, 351, 151–155.

[10] S. Pathak, N. Sakai, F. Wisnivesky Rocca Rivarola, S. D. Stranks, J. Liu, G. E. Eperon, C. Ducati, K. Wojciechowski, J. T. Griffiths, A. A. Haghighirad, A. Pellaroque, R. H. Friend, H. J. Snaith, Perovskite Crystals for Tunable White Light Emission, *Chem. Mater.* **2015**, 27, 8066–8075.

[11] G. L. Whitworth, J. R. Harwell, D. N. Miller, G. J. Hedley, W. Zhang, H. J. Snaith, G. A. Turnbull, I. D. W. Samuel, Nanoimprinted Distributed Feedback Lasers of Solution Processed Hybrid Perovskites, *Opt. Express* **2016**, 24, 23677–23684.

[12] P. Brenner, M. Stulz, D. Kapp, T. Abzieher, U. W. Paetzold, A. Quintilla, I. A. Howard, H. Kalt, U. Lemmer, Highly Stable Solution Processed Metal-Halide Perovskite Lasers on Nanoimprinted Distributed Feedback Structures, *Appl. Phys. Lett.* **2016**, 109, 141106.

[13] Y. Jia, R. A. Kerner, A. J. Grede, A. N. Brigeman, B. P. Rand, N. C. Giebink, Diode-Pumped Organo-Lead Halide Perovskite Lasing in a Metal-Clad Distributed Feedback Resonator, *Nano Lett.* **2016**, 16, 4624–4629.

[14] M. R. Leyden, S. Terakawa, T. Matsushima, S. Ruan, K. Goushi, M. Auffray, A. S. D. D. Sandanayaka, C. Qin, F. Bencheikh, C. Adachi, Distributed Feedback Lasers and Light-Emitting Diodes Using 1-Naphthylmethylamnonium Low-Dimensional Perovskite, *ACS Photonics* **2019**, 6, 460–466.

[15] C. Liu, Y. B. Cheng, Z. Ge, Understanding of Perovskite Crystal Growth and Film Formation in Scalable Deposition Processes, *Chem. Soc. Rev.* **2020**, 49, 1653–1687.

[16] Z. Li, J. Moon, A. Gharajeh, R. Haroldson, R. Hawkins, W. Hu, A. Zakhidov, Q. Gu, Room-Temperature Continuous-Wave Operation of Organometal Halide Perovskite Lasers, *ACS Nano* **2018**, 12, 10968–10976.

[17] N. Pourdavoud, T. Haeger, A. Mayer, P. J. Cegielski, A. L. Giesecke, R. Heiderhoff, S.

Olthof, S. Zaefferer, I. Shutsko, A. Henkel, D. Becker-Koch, M. Stein, M. Cehovski, O. Charfi, H. Johannes, D. Rogalla, M. C. Lemme, M. Koch, Y. Vaynzof, K. Meerholz, W. Kowalsky, H. Scheer, P. Görrn, T. Riedl, Room-Temperature Stimulated Emission and Lasing in Recrystallized Cesium Lead Bromide Perovskite Thin Films, *Adv. Mater.* **2019**, 31, 1903717.

[18] B. Jeong, H. Han, H. H. Kim, W. K. Choi, Y. J. Park, C. Park, Polymer-Assisted Nanoimprinting for Environment- and Phase-Stable Perovskite Nanopatterns, *ACS Nano* **2020**, 14, 1645–1655.

[19] B. Jeong, I. Hwang, S. H. Cho, E. H. Kim, S. Cha, J. Lee, H. S. Kang, S. M. Cho, H. Choi, C. Park, Solvent-Assisted Gel Printing for Micropatterning Thin Organic-Inorganic Hybrid Perovskite Films, *ACS Nano* **2016**, 10, 9026–9035.

[20] J. Harwell, J. Burch, A. Fikouras, M. C. Gather, A. Di Falco, I. D. W. Samuel, Patterning Multicolor Hybrid Perovskite Films via Top-Down Lithography, *ACS Nano* **2019**, 13, 3823–3829.

[21] N. Pourdavoud, S. Wang, A. Mayer, T. Hu, Y. Chen, A. Marianovich, W. Kowalsky, R. Heiderhoff, H.-C. Scheer, T. Riedl, Photonic Nanostructures Patterned by Thermal Nanoimprint Directly into Organo-Metal Halide Perovskites, *Adv. Mater.* **2017**, 29, 1605003.

[22] N. J. Jeon, J. H. Noh, Y. C. Kim, W. S. Yang, S. Ryu, S. Il Seok, Solvent Engineering for High-Performance Inorganic–Organic Hybrid Perovskite Solar Cells, *Nat. Mater.* **2014**, 13, 897–903.

[23] M. Yavari, M. Mazloum-Ardakani, S. Gholipour, M. M. Tavakoli, N. Taghavinia, A. Hagfeldt, W. Tress, Reducing Surface Recombination by a Poly(4-Vinylpyridine) Interlayer in Perovskite Solar Cells with High Open-Circuit Voltage and Efficiency, *ACS Omega* **2018**, 3, 5038–5043.

[24] L. Zuo, H. Guo, D. W. DeQuilettes, S. Jariwala, N. De Marco, S. Dong, R. DeBlock, D. S. Ginger, B. Dunn, M. Wang, Y. Yang, Polymer-Modified Halide Perovskite Films for

Efficient and Stable Planar Heterojunction Solar Cells, *Sci. Adv.* **2017**, 3, e1700106.

[25] V. Navarro-Fuster, I. Vragovic, E. M. Calzado, P. G. Boj, J. A. Quintana, J. M. Villalvilla, A. Retolaza, A. Juarros, D. Otaduy, S. Merino, M. A. Díaz-García, Film Thickness and Grating Depth Variation in Organic Second-Order Distributed Feedback Lasers, *J. Appl. Phys.* **2012**, 112, 043104.

[26] X. Fu, C. Peng, M. Samal, N. Barange, Y.-A. Chen, D.-H. Shin, Y. Mehta, A. Rozelle, C.-H. Chang, F. So, Mode Dispersion in Photonic Crystal Organic Light-Emitting Diodes, *ACS Appl. Electron. Mater.* **2020**, 2, 1759–1767.

[27] G. A. Turnbull, P. Andrew, M. J. Jory, W. L. Barnes, I. D. W. Samuel, Relationship between Photonic Band Structure and Emission Characteristics of a Polymer Distributed Feedback Laser, *Phys. Rev. B* **2001**, 64, 125122.

[28] V. Bonal, J. A. Quintana, J. M. Villalvilla, P. G. Boj, M. A. Díaz-García, Controlling the Emission Properties of Solution-Processed Organic Distributed Feedback Lasers through Resonator Design, *Sci. Rep.* **2019**, 9, 11159.

[29] W. Huang, Y. Liu, L. Hu, Q. Mu, Z. Peng, C. Yang, L. Xuan, Second-Order Distributed Feedback Polymer Laser Based on Holographic Polymer Dispersed Liquid Crystal Grating, *Org. Electron.* **2013**, 14, 2299–2305.

[30] M. Abdelsamie, K. Zhao, M. R. Niazi, K. W. Chou, A. Amassian, In Situ UV-Visible Absorption during Spin-Coating of Organic Semiconductors: A New Probe for Organic Electronics and Photovoltaics, *J. Mater. Chem. C* **2014**, 2, 3373–3381.

CHAPTER 5: SUMMARY AND OUTLOOK

5.1 Summary

The focus of this dissertation is on the applications of metal-halide perovskites in various optoelectronic devices, including photovoltaics (PVs), light-emitting diodes (LEDs), and distributed feedback (DFB) lasers. Each application is addressed by a corresponding chapter.

In Chapter 2, the importance of interfacial passivation in perovskite PVs has been revealed. Here, aluminum-doped zinc oxide (AZO) is employed as the electron transporting layer (ETL) due to a good thermal stability of perovskite films deposited on it. However, the device shows a low short circuit current density and a large photocurrent hysteresis, which are attributed to the poor interfacial properties between the ETL and the perovskite layer. To address this issue, a thin interfacial modification layer of phenyl-C61-butyric acid methyl ester (PCBM) is employed, leading to an increased photocurrent and fill factor, as well as a reduced hysteresis. The increase in photocurrent and fill factor can be attributed to improved electron extraction facilitated by PCBM, while the reduction in hysteresis can be attributed to the defect passivation of the interfacial traps by PCBM. We demonstrated that PCBM functions as an effective interfacial defect passivation material in perovskite solar cells having an AZO ETL.

In Chapter 3, the impact of ion migration on the operation of perovskite LEDs is studied by transient measurements. From the measurements, we found that the electroluminescence (EL) intensity, the current density and the device efficiency all show a slow response in a time scale of tens of milliseconds. Through transient current measurements on single carrier devices, the data reveal that the slow current response is due to a slow hole injection response which is attributed to the migration and accumulation of the Br ions at the anode interface facilitating hole injection. On the contrary, electron injection is not affected by ion migration. Such a different effect of ion migration on electron and hole injection leads to a strong charge imbalance, suggesting that to enhance the device efficiency electron injection needs to be significantly enhanced to compensate for the enhanced hole injection facilitated by halide ion migration. In addition, through photoluminescence (PL) measurements under pulse voltage, we identified that the slow efficiency response is mainly attributed to the enhanced charge injection which leads to an increased carrier density favoring bimolecular radiative recombination. Our findings shed light on the understanding of the device physics of perovskite LEDs, thereby paved the way for the future design of device architecture and materials to realize the full potential of perovskites LEDs.

In Chapter 4, a facile and systematic methodology to fine-tune the cavity of perovskite surface-emitting DFB lasers is developed. To simplify the cavity-fabrication, a polymer polyvinylpyrrolidone (PVP) is added in the perovskite precursor solutions to assist direct nanoimprint. Through in-situ absorption measurements, PVP has been found to maintain the amount of solution after spin coating, enabling the formation of a stable and soft precursor film that is ready for straightforward nanoimprint to form well-shaped gratings. Through transient absorption spectroscopy, PVP has been found to reduce the defect density in the perovskite film, promoting the amplified spontaneous emission (ASE) performance. To accelerate the cavity fine-tuning, a systematic analysis of the optical modes in the DFB structures is introduced. Through the angle-resolved PL spectra (ARPS) measurements, the resonant wavelength can be determined, which can accelerate the cavity fine-tuning process. In addition, the spatial pattern of the ASE diffraction can also be used for guiding the cavity fine-tuning direction. Based on the methodology, an optimized laser performance with 20 μJ/cm^2 threshold and 0.86 nm FWHM has been achieved with largely reduced efforts. More importantly, this methodology can also be applied to other solution-processed DFB lasers, such as organic lasers and quantum dot lasers.

5.2 Outlook

Although metal-halide perovskites exhibit good performance in various optoelectronic applications, there is always a central issue, their poor stability, hindering them from practical applications. The poor stability has two origins. One is due to the degradation of perovskite materials under the exposure of moisture or oxygen, while the other is due to the degradation under electric stress or illumination. The former can be tackled by good encapsulation techniques, which should not be the most critical issue. In contrast, enhancing the stability of perovskites under electric stress or illumination is the main challenge. It has been concluded that such an instability is mainly due to ion migration in perovskites. Specifically, on one hand, ion migration leads to the degradation of the perovskite layer itself; on the other hand, it can cross the interfaces in devices resulting in degradation of other functional layers. Therefore, to address this issue comprehensively, material scientists and device physicists should work more closely, not only to suppress ion migration in the perovskite through material engineering, but also to suppress interfacial ion migration by novel designs of device architectures.